Florian Bernd Gußmann

Classical DFT and liquid-liquid phase transitions

Dissertation

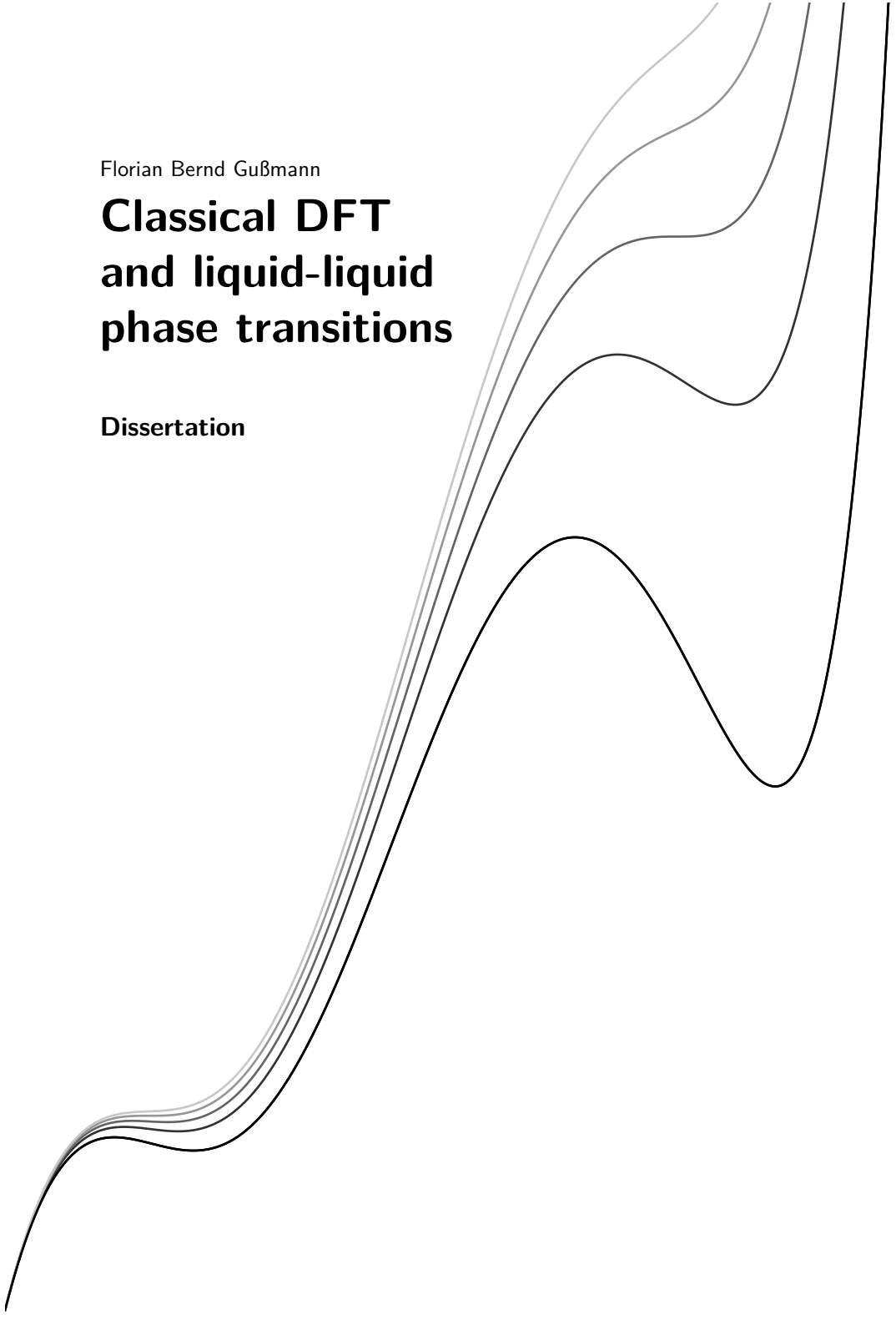

Classical DFT and liquid-liquid phase transitions

Dissertation
der Mathematisch-Naturwissenschaftlichen Fakultät
der Eberhard Karls Universität Tübingen
zur Erlangung des Grades eines
Doktors der Naturwissenschaften
(Dr. rer. nat.)

vorgelegt von
Dipl. Phys. Florian Bernd Gußmann
aus Stuttgart

Tübingen
2020

Gedruckt mit Genehmigung der Mathematisch-Naturwissenschaftlichen Fakultät der Eberhard Karls Universität Tübingen.

Tag der mündlichen Qualifikation:	19. 11. 2020
Stellvertretender Dekan:	Prof. Dr. József Fortágh
1. Berichterstatter:	Prof. Dr. Roland Roth
2. Berichterstatter:	Prof. Dr. Martin Oettel

Contents

Abstract

(*Deutsche Version siehe unten.*) This dissertation examines how classical density functional theory (DFT) [11] can be applied to study liquid-liquid phase transitions in simple fluids under confinement. Here, two model system are investigated. The primary focus is on the construction of a DFT for the Jagla fluid [22] – this constitutes Pt. II of this work – which exhibits a liquid-liquid critical point in the bulk phase diagram as well as a density anomaly, and, thus, is a suitable simple model system for water. In Pt. III the effect of confinement by the infinite slit geometry on the liquid-liquid phase transition of colloids in a ternary colloid-polymer mixture is investigated. For this, the Asakura-Oosawa model [2, 3] is applied.

First, we determine the bulk phase diagram of the Jagla fluid by using perturbation theory. We find that the perturbation approaches of Barker and Henderson (BH) [4] as well as of Week, Chandler, and Andersen (WCA) [41] are not suited to obtain the liquid-liquid binodal of the Jagla fluid due the long range of the Jagla interaction potential. Instead, we succeed to compute the gas-liquid and the liquid-liquid binodal of the Jagla fluid using first-order perturbation theory by separating the Jagla potential twice into reference and perturbation part. Based on this, we continue to construct a perturbation DFT for the Jagla fluid, where we follow the route of Sokolowski and Fischer [37], to be able to describe the inhomogeneous fluid. While our perturbation DFT produces correct density profiles in the infinite slit geometry at high temperatures and not too close to the binodals, it fails at low temperatures where the bulk liquid-liquid critical point of the Jagla fluid is located. Nevertheless, our perturbation DFT

performs significantly better than standard mean-field DFT. In a second approach to describe the inhomogeneous Jagla fluid, we try to use Monte Carlo (MC) simulation data of the Jagla bulk fluid to compute an optimized interaction potential which, if applied in standard mean-field DFT, recovers the quasi-exact MC results of the inhomogeneous fluid. We find the density profiles of the MC-optimized DFT in the infinite slit geometry to have improved compared to the results of the perturbation DFT. Especially at state points not too close to the bulk binodals, the agreement between MC and optimized DFT profiles is excellent, even at state points where perturbation DFT produces unphysical oscillations. In the low temperature region, where the bulk liquid-liquid critical point of the Jagla fluid is located, the optimized DFT profiles are at least in the same range as the MC data. It turns out, however, that our optimized DFT fails to predict phase transitions inside the slit caused by the reduction of the wall separation distance, and, thus, is not suited to compute the phase diagram of the inhomogeneous Jagla fluid.

Interestingly, it is also possible to encounter a liquid-liquid transition in a model for colloid-polymer mixtures within the so-called Asakura-Oosawa model [2, 3], if the polymers are bi- or polydisperse and thus give rise to a second length scale in the effective colloid-colloid interaction [15]. Here, we use the framework of fundamental measure theory (FMT) [30, 32] to describe the bulk mixture as well as the inhomogeneous mixture within DFT. We find that under the confinement of the infinite slit with hard walls, the binodals (gas-liquid and liquid-liquid) are shifted towards higher colloid packing fractions, where the density jump between coexisting phases decreases. The critical points are shifted to higher polymer reservoir packing fractions.

German version: Diese Dissertation untersucht, inwieweit klassische Dichtefunktionaltheorie (DFT) verwendet werden kann [11], um flüssig-flüssige Phasenübergänge in einfachen Fluiden innerhalb einschränkender Geometrien zu untersuchen. Dabei werden zwei Modellsysteme näher betrachtet. Das Hauptaugenmerk liegt auf der Konstruktion einer DFT für das Jagla-Fluid [22] – dies geschieht in Teil II dieser Arbeit –, welches sowohl einen flüssig-flüssigen kritischen Punkt im Bulkphasendiagramm aufweist, als auch eine Dichteanomalie, und daher ein geeignetes einfaches Modellsystem für Wasser ist. In Teil III wird der Effekt von räumlicher Einschränkung durch einen Spalt mit unendlich großen Wänden auf den flüssig-flüssigen Phasenübergang von Kolloiden in einer ternären Kolloid-Polymer-Mischung untersucht.

Zunächst bestimmen wir das Bulkphasendiagramm des Jagla-Fluids mittels Störungstheorie. Dabei stellt sich heraus, dass die Störungstheorien von Barker und Henderson (BH) [4], sowie von Weeks, Chandler und Andersen (WCA) [41] ungeeignet sind, um die flüssig-flüssige Binodale des Jagla-Fluids zu bestimmen. Dies lässt sich auf die lange Reichweite des Jagla-Wechselwirkungspotentials zurückführen. Stattdessen gelingt es uns, die gas-flüssige und die flüssig-flüssige Binodale des Jagla-Fluids mittels Störungsrechung erster Ordnung zu berechnen, wobei wir hierzu das Jagla-Potential zweimal in Referenz- und Störungspotential aufteilen. Hierauf basierend konstruieren wir eine Störungs-DFT für das Jagla-Fluid, um das inhomogene Fluid behandeln zu können. Hierbei folgen wir der Arbeit von Sokolowski and Fischer [37]. Diese Störungs-DFT liefert korrekte Dichteprofile im Spalt mit unendlich ausgedehnten harten Wänden, bei hohen Temperaturen und nicht in direkter Umgebung einer der Binodalen. Jedoch versagt sie für tiefe Temperaturen, wo der flüssig-flüssige kritische Punkt des Jagla-Fluids liegt. Dennoch liefert unsere Störungs-DFT signifikant bessere Ergebnisse als die gewöhnliche

Mean-Field DFT. In einem zweiten Versuch, das inhomogene Jagla-Fluid korrekt zu beschreiben, versuchen wir Daten aus Monte-Carlo(MC)-Simulationen des homogenen Jagla-Fluids zu verwenden, um ein optimiertes Wechselwirkungspotential zu berechnen. Dieses soll, falls in der gewöhnlichen Mean-Field-DFT angewendet, die quasiexakten MC-Ergebnisse des inhomogenen Fluids reproduzieren. Die mittels der optimierten DFT gewonnenen Dichteprofile in der Spaltgeometrie mit unendlich ausgedehnten harten Wänden stellen eine Verbesserung gegenüber den Ergebnissen unserer Störungs-DFT dar. Insbesondere in Zuständen, die nicht allzu nahe an den Binodalen liegen, ist die Übereinstimmung der optimierten DFT-Dichteprofile mit den MC-Dichteprofilen exzellent; dies ist sogar in Zuständen der Fall, für welche die Störungs-DFT-Dichteprofile unphysikalische Oszillationen aufzeigen. In der Niedrigtemperaturregion, wo sich der flüssig-flüssige kritische Punkt des Jagla-Fluids befindet, ähneln die Dichteprofile der optimierten DFT zumindest noch den MC-Dichteprofilen. Trotz diesen zunächst positiven Ergebnissen, stellt es sich heraus, dass die optimierte DFT nicht in der Lage ist, Phasenübergänge im Inneren des Spalts vorherzusagen, die durch die Änderung der Spaltbreite hervorgerufen werden. Damit ist auch die optimierte DFT ungeeignet, um das Phasendiagramm des inhomogenen Jagla-Fluids zu untersuchen.

Interresanter Weise ist es ebenfalls möglich, einen flüssig-flüssigen Phasenübergang in einem Modellsystem einer Kolloid-Polymer-Mischung innerhalb des sogenannten Asakura-Oosawa-Modells [2, 3] zu beobachten; dieser tritt auf, wenn die Polymere bi- oder polydispers sind und somit eine zweite Längenskala in der effektiven Kolloid-Kolloid-Wechselwirkung entstehen lassen [15]. Hierbei verwenden wir die Fundamental-Measure-Theory (FMT) [30, 32], um die Bulkmischung sowie die inhomogene Mischung mittels DFT zu beschreiben. Unter der räumlichen

Einschränkung durch den Spalt verschieben sich die gas-flüssige und flüssig-flüssige Binodale zu höheren Kolloidpackungsdichten, wobei sich der Dichtesprung zwischen koexistierenden Phasen verringert. Des Weiteren wandern beide kritischen Punkte zu höheren Polymerreservoirpackungsdichten.

1. Introduction

One possible explanation of the various anomalies of water is the assumption of a liquid-liquid transition between two phases of supercooled water [29, 9]. The physical existence of a liquid-liquid critical point, however, is not verified yet, as it corresponds to metastable states which are experimentally inaccessible due to crystallization [6, 9].

In contrast, the existence of a liquid-liquid critical point and a density anomaly can be achieved quite easily in rather simple model systems where the spherically symmetric interaction potential is composed of an attractive part and two characteristic short-ranged repulsive components [14]. As for these model systems also cases are reported in which a liquid-liquid transition exists while no density anomaly is observed [13], the model for the actual physical system of interest needs to be chosen carefully. In his work from 2001 [22] Jagla introduces a three dimensional isotropic ramp potential, composed of a hard core, a linear repulsion at short distances, and a long ranged linear attractive part, which exhibits a liquid-liquid transition and a density anomaly. Xu et al. [42] furthermore showed in their molecular dynamic (MD) simulation study that the Jagla model displays a liquid-liquid coexistence line without the need to supercool.

While the work mentioned so far focus on bulk phase behavior, the major aim of this dissertation (see Pt. II) is to exploit the rather simple shape of the Jagla model to develop a perturbation theory for the inhomogeneous fluid based on classical

density functional theory (DFT) [11]. Being able to describe the inhomogeneous Jagla fluid would provide us the possibility to alter the phase diagram based on the nature of the confinement. This in turn might be a first small step towards the finding of an experimental setting which stabilizes the liquid-liquid critical point of water, thus enabling experimental proof. In addition, a description of the inhomogeneous Jagla fluid would enable us to study its local structure close to walls and phenomena like wetting and dewetting and capillarity. The advantage of a perturbation DFT over simulations is that, once established, the confining geometry and its properties can be altered rather easily, and, furthermore, the time cost of the calculations is notably smaller (minutes instead of hours), making DFT a highly efficient framework for testing various confinements. The challenge with a perturbation DFT, of course, is finding an approximation of the intrinsic excess free energy functional which yields reasonable results.

In this work we use the same form of the Jagla potential as in Refs. [24, 42], but scaled by a factor of 2/7 in the direction of the ordinate which essentially comes down to a scaling of temperature. The functional form is given by:

$$v_{\mathrm{J}}(r) = \begin{cases} \infty & , r < \sigma \\ \frac{-2\,\epsilon}{7}\frac{r-r_0}{r_{\mathrm{m}}-r_0} & , \sigma \leq r \leq r_{\mathrm{m}} \\ \frac{2\,\epsilon}{7}\frac{r-r_2}{r_2-r_{\mathrm{m}}} & , r_{\mathrm{m}} < r \leq r_2 \\ 0 & , r > r_2 \end{cases},$$

where r denotes the particle-particle distance, and $r_0 = 1.56\,\sigma$, $r_{\mathrm{m}} = 1.72\,\sigma$, and $r_2 = 3.0\,\sigma$ are the positions of the first zero crossing and the minimum, and the range of the potential, respectively. The quantity σ denotes the hard-sphere diameter and ϵ is our unit of energy. Figure 1.1 shows a plot of the Jagla potential,

and compares it with the modified Lennard-Jones potential

$$v_{\mathrm{LJ}}(r) = \frac{8\epsilon}{7}\left[\left(\frac{\sigma}{r}\right)^{12} - \left(\frac{\sigma}{r}\right)^{6}\right] \tag{1.1}$$

which is the standard Lennard-Jones potential scaled by 2/7 so that the depths of the potential wells are equal. Note, the far greater range of the Jagla potential's repulsive and attractive parts.

Interestingly, it is also possible to encounter a liquid-liquid transition in a model for colloid-polymer mixtures within the so-called Asakura-Oosawa model [2, 3], if the polymers are bi- or polydisperse and thus give rise to a second length scale in the effective colloid-colloid interaction [15]. Our aim is to study the behavior of the liquid-liquid transition under confinement.

This dissertation is structured as follows. In Pt. I we briefly introduce the concepts and quantities required in the following chapters. Part II covers our effort to construct a DFT which is capable of describing the inhomogeneous Jagla fluid. Here, we begin to establish a bulk perturbation description in Chpt. 6, upon which a perturbation DFT can be built. The construction of the latter is described in Chpt. 7. A second approach to gain a DFT for the Jagla fluid is discussed in Chpt. 8, where we use Monte Carlo (MC) simulation data to compute an optimized interaction potential for standard mean-field DFT. In Pt. III the effect of confinement of the infinite slit geometry with hard walls on the gas-liquid and the liquid-liquid binodal of a ternary colloid-polymer mixture is investigated. We conclude and present additional remarks in Pt. IV.

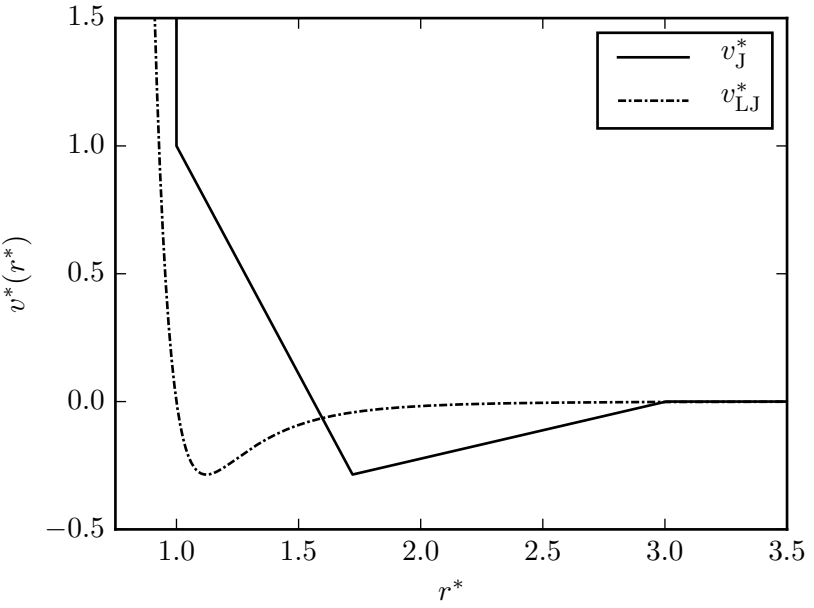

Figure 1.1.: The reduced Jagla potential $v_{\mathrm{J}}^* = v_{\mathrm{J}}/\epsilon$ as applied in this work (solid line), and reduced (12-6)-Lennard-Jones potential $v_{\mathrm{LJ}}^* = v_{\mathrm{LJ}}/\epsilon$ scaled such that the depths of the potential wells are equal (dash-dotted line), namely $2\epsilon/7$. The quantity $r^* = r/\sigma$ is the reduced center-to-center particle distance.

Part I.

Basic concepts

Introduction to Pt. I: The aim of Pt. I of this thesis is to briefly introduce the reader to the concepts and quantities applied in the following parts. Here, no claim to completeness of the corresponding topics is made, as those have been discussed in detail elsewhere before.

Chapters 2 and 3 are meant to introduce all quantities needed for the derivation of the bulk perturbation theory in Sec. 6.1, especially the concept of the radial distribution function which is of central importance in this work. Here, we follow closely Ref. [17]. A thorough introduction to the idea of statistical ensembles can e.g. be found in Refs. [26, 17].

Chapter 4 concisely explains the concept of classical density functional theory, the central theory applied in this work, and of fundamental measure theory which is a density functional theory for hard-sphere fluids. For a more detailed discussion of the topics the reader is referred to Refs. [11, 17, 20, 16] for classical density functional theory and to Refs. [32, 30, 31, 18, 17, 16] for fundamental measure theory.

In Chpt. 5 the methods to calculate the radial distribution function of an isotropic homogeneous fluid by means of classical density functional theory and Monte-Carlo simulations are explained, as these were a central element of the calculations done for this thesis. A comprehensive discussion of Monte-Carlo simulations methods for simple fluids is given in Refs. [8, 17].

2. Canonical ensemble

2.1. Basics

Let us consider an ensemble of isolated, macroscopic systems at fixed temperature T, which consist of N identical, spherically symmetric particles of mass m, described via the $3N$ spatial coordinates $\mathbf{r}^N \equiv \mathbf{r}_1, \ldots, \mathbf{r}_N$ and the $3N$ momenta $\mathbf{p}^N \equiv \mathbf{p}_1, \ldots, \mathbf{p}_N$, which are enclosed in a volume V. The corresponding ensemble equilibrium probability density is then given by [17, 26, 20]

$$P_N(\mathbf{r}^N, \mathbf{p}^N) = \frac{1}{h^{3N} N!} \frac{\exp(-\beta \mathcal{H})}{Q_N}, \tag{2.1}$$

where

$$Q_N = \frac{1}{h^{3N}\, N!} \iint \exp(-\beta \mathcal{H}) \mathrm{d}\mathbf{r}^N \mathrm{d}\mathbf{p}^N \tag{2.2}$$

is the partition function of the canonical ensemble, h is Planck's constant, $\beta = (k_\mathrm{B} T)^{-1}$, with Boltzmann's constant k_B, and $\mathcal{H} = \mathcal{H}(\mathbf{r}^N, \mathbf{p}^N)$ is the hamiltonian of the system which we assume to be of the form:

$$\mathcal{H}(\mathbf{r}^N, \mathbf{p}^N) = K_N(\mathbf{p}^N) + V_N(\mathbf{r}^N). \tag{2.3}$$

Here,

$$K_N = \sum_{i=1}^{N} \frac{|\mathbf{p}_i|^2}{2m}$$

is the total kinetic energy of the system and V_N is the interatomic potential energy. With a hamiltonian given, we can calculate the equilibrium canonical ensemble average $\langle B(\mathbf{r}^N, \mathbf{p}^N)\rangle$ of a function $B(\mathbf{r}^N, \mathbf{p}^N)$ via [17]

$$\begin{aligned}\langle B(\mathbf{r}^N, \mathbf{p}^N)\rangle &= \iint B(\mathbf{r}^N, \mathbf{p}^N) P_N(\mathbf{r}^N, \mathbf{p}^N) \mathrm{d}\mathbf{r}^N \mathrm{d}\mathbf{p}^N \\ &= \frac{1}{h^{3N} N!} \frac{1}{Q_N} \iint B(\mathbf{r}^N, \mathbf{p}^N) \exp(-\beta \mathcal{H}) \mathrm{d}\mathbf{r}^N \mathrm{d}\mathbf{p}^N,\end{aligned} \tag{2.4}$$

where the expression in Eq. (2.1) was used for the second equality. If the hamiltonian is of the form as in Eq. (2.3), the integration over the momenta in Eq. (2.2) can be carried out analytically and yields a factor of $(2\pi m k_\mathrm{B} T)^{1/2}$ for each of the $3N$ degrees of freedom [17]. Hence, the partition function Q_N can be rewritten to be

$$Q_N = \frac{1}{N!} \frac{Z_N}{\Lambda^{3N}},$$

where

$$\Lambda = \sqrt{\frac{h^2 \beta}{2\pi m}} \tag{2.5}$$

is the thermal wavelength and

$$Z_N = \int \exp(-\beta V_N) \mathrm{d}\mathbf{r}^N \tag{2.6}$$

is the so called configuration integral [17]. Likewise, if additionally the function B is only a function of the spatial coordinates $\mathbf{r}^N$, $B = B(\mathbf{r}^N)$, the expression for the ensemble average in Eq. (2.4) simplifies to be

$$\langle B(\mathbf{r}^N)\rangle = \frac{1}{Z_N} \int B(\mathbf{r}^N) \exp\big(-\beta V_N(\mathbf{r}^N)\big) \mathrm{d}\mathbf{r}^N. \tag{2.7}$$

If, for a moment, we assume non-interacting, or ideal, particles, i.e. $V_N = 0$, the configuration integral reduces to

$$Z_N = \int \cdots \int \mathrm{d}\mathbf{r}_1 \ldots \mathrm{d}\mathbf{r}_N = V^N, \tag{2.8}$$

and, hence, the partition function of a an ideal gas in bulk is given by [17]

$$Q_N^{\mathrm{id}} = \frac{1}{N!} \frac{V^N}{\Lambda^{3N}}. \tag{2.9}$$

With this, we can rewrite the partition function of our system of interacting particles to be

$$Q_N = Q_N^{\mathrm{id}} \frac{Z_N}{V^N}. \tag{2.10}$$

The thermodynamic potential of the canonical ensemble is the Helmholtz free energy [17, 26]

$$F = U - T\,S, \tag{2.11}$$

with the internal energy $U = TS - pV + \mu N$, the entropy S, the pressure p, and the chemical potential μ, which can be calculated from the partition function Q_N via

$$F = -k_{\mathrm{B}} T \ln Q_N.$$

Given the expression in Eq. (2.10), and by applying Stirling's approximation, $\ln N! \approx N \ln N - N$ for large N, the Helmholtz free energy can be written as the sum of ideal and excess parts:

$$\begin{aligned} F &\overset{(2.10)}{=} -k_{\mathrm{B}} T \ln Q_N^{\mathrm{id}} - k_{\mathrm{B}} T \ln \frac{Z_N}{V^N} \\ &\overset{(2.9)}{=} N k_{\mathrm{B}} T (\ln \Lambda^3 \rho - 1) - k_{\mathrm{B}} T \ln \frac{Z_N}{V^N} \\ &\equiv F^{\mathrm{id}} + F^{\mathrm{ex}}, \end{aligned} \tag{2.12}$$

where $\rho = N/V$ is the bulk density[1] of the system. The excess part contains all information of the particle-particle interaction and in case of a non-vanishing external potential, i.e. in case of an inhomogeneous fluid, also the contribution of the external potential to the Helmholtz free energy.

2.2. Distribution functions in the canonical ensemble

Often, the information on the positions and momenta of all N particles in the system, provided by the probability density in Eq. (2.1), is unnecessarily detailed, and it is sufficient to only consider a subset of n particles and their positions, and to integrate out the positions of the other $N-n$ particles as well as the momenta of all particles [17]. Hence, it is convenient to introduce the canonical equilibrium n-particle density of a system without external potential [17]:

$$\begin{aligned}\rho_N^{(n)}(\mathbf{r}^n) &= \frac{N!}{(N-n)!}\frac{1}{Q_N}\iint \exp(-\beta\mathcal{H})\mathrm{d}\mathbf{r}^{(N-n)}\mathrm{d}\mathbf{p}^N \\ &= \frac{N!}{(N-n)!}\frac{1}{Z_N}\int \exp(-\beta V_N)\mathrm{d}\mathbf{r}^{(N-n)}, \end{aligned} \tag{2.13}$$

where in the second equality the integration over the momenta is carried out. The quantity $\rho_N^{(n)}(\mathbf{r}^n)\mathrm{d}\mathbf{r}^n$ is the probability to find n arbitrary particles of the system inside the volume element $\mathrm{d}\mathbf{r}^n$ at the position $\mathbf{r}^n = (\mathbf{r}_1, \ldots, \mathbf{r}_n)$, irrespective of the positions of the other $N-n$ particles and the momenta of all particles. From

[1] We denote the bulk density of an homogeneous system by ρ and, for resons of clarity, the bulk density in case of an inhomogeneous system by ρ_b.

Eq. (2.13) we can see that

$$\int \rho_N^{(n)}(\mathbf{r}^n)\mathrm{d}\mathbf{r}^n \overset{(2.6)}{=} \frac{N!}{(N-n)!},$$

and, hence,

$$\int \rho_N^{(1)}(\mathbf{r})\mathrm{d}\mathbf{r} = N. \tag{2.14}$$

For a homogeneous fluid, the single-particle density $\rho_N^{(1)}(\mathbf{r})$ must be independent of the position $\mathbf{r}$ from which follows[2] that for a homogeneous fluid the single-particle density is equal to the bulk number density ρ:

$$\rho_N^{(1)}(\mathbf{r}) = \frac{N}{V} = \rho. \tag{2.15}$$

If the fluid is not only homogeneous, but also ideal, the pair density is given by[3]

$$\rho_N^{(2)} = \rho^2\left(1 - \frac{1}{N}\right). \tag{2.17}$$

[2] If the single-particle density is independent of the position $\mathbf{r}$, Eq. (2.14) can be rewritten to be

$$N = \rho_N^{(1)} \int \mathrm{d}\mathbf{r}.$$

Since $\int \mathrm{d}\mathbf{r} = V$, we obtain $\rho_N^{(1)} = N/V$ for the homogeneous fluid.

[3] From Eq. (2.13) we know that

$$\rho_N^{(2)}(\mathbf{r}_1, \mathbf{r}_2) = \frac{N!}{(N-2)!}\frac{1}{Z_N}\int \exp(-\beta V_N)\mathrm{d}\mathbf{r}^{(N-2)}. \tag{2.16}$$

In the case of an ideal gas $V_N = 0$ and $Z_N = V^N$ holds [see Eq. (2.8)], and (2.16) simplifies to be

$$\rho_N^{(2)} = \frac{N!}{(N-2)!}\frac{1}{V^N}V^{N-2} = \frac{N}{V}\frac{N-1}{V} = \rho^2\left(1 - \frac{1}{N}\right).$$

Based on the canonical n-particle densities, the canonical n-particle distribution functions can be defined [17]:

$$g_N^{(n)}(\mathbf{r}^n) = \frac{\rho_N^{(n)}(\mathbf{r}_1, \ldots, \mathbf{r}_n)}{\prod_{i=1}^n \rho_N^{(1)}(\mathbf{r}_i)}. \tag{2.18}$$

For a homogeneous system (2.18) becomes

$$\rho^n g_N^{(n)}(\mathbf{r}^n) \overset{(2.15)}{=} \rho_N^{(n)}(\mathbf{r}^n). \tag{2.19}$$

The particle distribution functions are a measure for how much the structure of the fluid is different to complete randomness, and provide, together with the particle densities, a complete description of a fluid's structure. The low-order distribution functions, especially the pair density $\rho_N^{(2)}(\mathbf{r}_1, \mathbf{r}_2)$, are often sufficient to obtain the thermodynamic properties of a system such as the equation of state. For an isotropic particle-particle interaction potential, the pair distribution function $g_N^{(2)}(\mathbf{r}_1, \mathbf{r}_2)$ becomes a function of merely the particle-particle distance $r_{12} = |\mathbf{r}_2 - \mathbf{r}_1|$, and it is then often simply called the radial distribution function $g(r)$. If the particle-particle distance r is much greater than the range of the interaction potential, the information on the latter gets lost, and the two particles "see" each other as ideal. Therefore, for large r, $g(r)$ approaches the ideal gas limit which, via Eqs. (2.17) and (2.19), we identify as $(1 - 1/N)$. For large N, in good approximation, this is equal to 1. The quantity $\rho g(r)$ can be interpreted as the single-particle density around a reference particle in the fluid, and, hence, the average number of particles inside the spherical shell around the reference particle, containing all distances from r to $r + \mathrm{d}r$, is $4\pi r^2 \rho g(r) \mathrm{d}r$ [17]. Figure 2.1 shows the radial distribution function of a one-component hard-sphere fluid, obtained through a density functional theory calculation,

at a reduced density $\rho^* = \rho \approx 0.67$, or at a packing fraction $\eta = \frac{\pi}{6}\rho\sigma^3 = 0.35$. The form of the radial distribution function

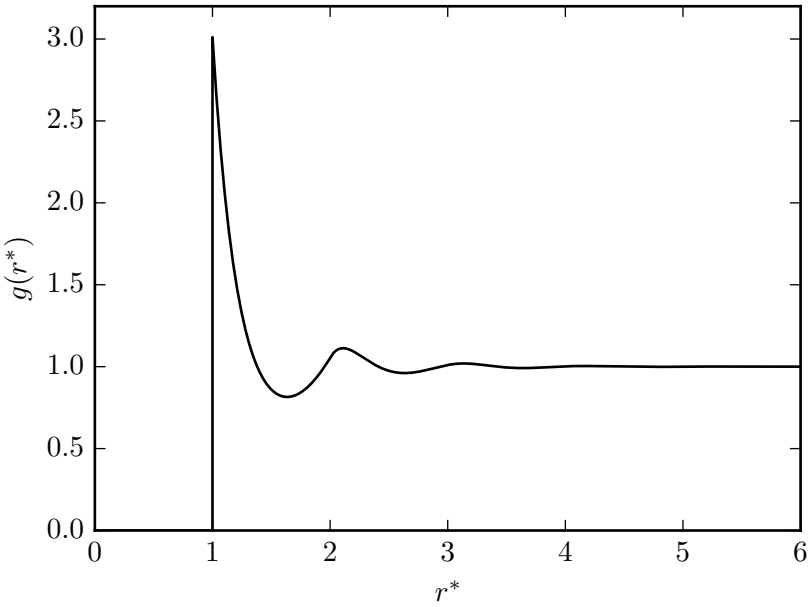

Figure 2.1.: The radial distribution function $g(r^*)$ of a one component hard-sphere fluid at $\eta = 0.35$ as a function of the reduced center-to-center particle distance $r^* = r/\sigma$.

delivers a basic idea of what is understood as the structure of a fluid at the level of pair correlations. For $0 \leq r \leq \sigma$, the radial distribution function is zero, which is due to the fact that hard-sphere particles can not overlap, and for large r the ideal gas limit is attained. The peaks in the plot represent "shells" of neighboring particles around the reference particle [17].

3. Grand canonical ensemble

3.1. Basics

If the system of consideration is open, in the sense that the exchange of particles with a particle reservoir is possible, its thermodynamic state is defined via the chemical potential μ, the volume V, and the temperature T, and the corresponding statistical ensemble is called the grand canonical ensemble. The grand canonical probability density is given by [17, 26]

$$P(\mathbf{r}^N, \mathbf{p}^N; N) = \frac{\exp\big(-\beta(\mathcal{H} - N\mu)\big)}{\Xi}$$

which now is not only a function of the phase space variables $\mathbf{r}^N$ and $\mathbf{p}^N$, but also of the number of particles N in the system. Here,

$$\begin{aligned}\Xi &= \sum_{N=0}^{\infty} \frac{\exp(N\beta\mu)}{h^{3N}N!} \iint \exp(-\beta\mathcal{H})\mathrm{d}\mathbf{r}^N\mathrm{d}\mathbf{p}^N \\ &= \sum_{N=0}^{\infty} \frac{z^N}{N!} Z_N, \end{aligned} \tag{3.1}$$

and $\mathcal{H}$ is the hamiltonian of the system which we assume to be of the form as in Eq. (2.3). In the second equality of (3.1) the degrees of freedom of the momenta are integrated out, and the quantity

$$z = \frac{\exp(\beta\mu)}{\Lambda^3}$$

is the activity. The grand canonical ensemble average of a function $B(\mathbf{r}^N, \mathbf{p}^N)$ is

$$\langle B \rangle = \sum_{N=0}^{\infty} \frac{1}{h^{3N} N!} \iint B(\mathbf{r}^N, \mathbf{p}^N)\, P(\mathbf{r}^N, \mathbf{p}^N; N) \mathrm{d}\mathbf{r}^N \mathrm{d}\mathbf{p}^N.$$

If the function B is independent of the phase space variables, the average can be written as

$$\begin{aligned} \langle B \rangle &= \sum_{N=0}^{\infty} B \frac{1}{h^{3N} N!} \iint P(\mathbf{r}^N, \mathbf{p}^N; N) \mathrm{d}\mathbf{r}^N \mathrm{d}\mathbf{p}^N \\ &\equiv \sum_{N=0}^{\infty} B\, P(N), \end{aligned} \tag{3.2}$$

where we have defined the quantity

$$P(N) = \frac{1}{h^{3N} N!} \iint P(\mathbf{r}^N, \mathbf{p}^N; N) \mathrm{d}\mathbf{r}^N \mathrm{d}\mathbf{p}^N = \frac{1}{\Xi} \frac{z^N}{N!} Z_N \tag{3.3}$$

which, from (3.2), we can identify as the probability that a system of the ensemble contains N particles. In the second equality of (3.3), again, the integral over the momenta is carried out. With this, we can calculate the mean number of particles in the system [17]:

$$\langle N \rangle = \sum_{N=0}^{\infty} N\, P(N) = \frac{1}{\Xi} \sum_{N=0}^{\infty} N \frac{z^N}{N!} Z_N = \frac{\partial \ln \Xi}{\partial \ln z}.$$

The thermodynamic potential of the grand canonical ensemble is the grand potential [17, 26]

$$\Omega = F - N\mu$$

which can be calculated from the grand partition function Ξ via

$$\Omega = -k_\mathrm{B}T \ln \Xi. \tag{3.4}$$

With the free energy F from Eq. (2.11), the grand potential simplifies to be

$$\Omega = -pV.$$

3.2. Distribution functions in the grand canonical ensemble

The grand canonical equilibrium n-particle density is defined via the canonical equilibrium n-particle density [Eq. (2.13)] to be

$$\begin{aligned}\rho^{(n)}(\mathbf{r}^n) &= \sum_{N=n}^{\infty} P(N)\rho_N^{(n)}(\mathbf{r}^n) \\ &\overset{(3.3)(2.13)}{=} \frac{1}{\Xi}\sum_{N=n}^{\infty}\frac{z^N}{(N-n)!}\int \exp(-\beta V_N)\mathrm{d}\mathbf{r}^{(N-n)}.\end{aligned} \tag{3.5}$$

Integration of (3.5) with respect to the spacial variables $\mathbf{r}_1, \ldots, \mathbf{r}_n$ gives (see App. A.1)

$$\int \rho^{(n)}(\mathbf{r}^n)\mathrm{d}\mathbf{r}^n = \left\langle \frac{N!}{(N-n)!} \right\rangle,$$

from which follows that

$$\int \rho^{(1)}(\mathbf{r})\mathrm{d}\mathbf{r} = \langle N \rangle. \tag{3.6}$$

If the fluid is homogeneous, the single-particle density $\rho^{(1)}(\mathbf{r})$ must be independent of the position $\mathbf{r}$, and, hence, we find from (3.6), with the analogue calculation as in Sec. 2.2:

$$\rho^{(1)}(\mathbf{r}) = \langle N \rangle / V \equiv \rho.$$

Note that for reasons of simplicity, from now on we refer to the one-particle density as $\rho(\mathbf{r})$. For a homogeneous and ideal fluid the n-particle densities are (see App. A.2)

$$\rho^{(n)} = \rho^n.$$

The definition of the grand canonical n-particle distribution function is similar to the definition in the canonical ensemble, namely:

$$g^{(n)}(\mathbf{r}^n) = \frac{\rho^{(n)}(\mathbf{r}_1, \ldots, \mathbf{r}_n)}{\prod_{i=1}^{n} \rho^{(1)}(\mathbf{r}_i)}, \tag{3.7}$$

and in the homogeneous case:

$$\rho^{(n)}(\mathbf{r}^n) = \rho^n g^{(n)}(\mathbf{r}^n).$$

If, in the homogeneous case, for all pairs of the n particles the separation becomes sufficiently large, $g^{(n)}$ approaches the ideal gas limit (c.f. Sec. 2.2): $g^{(n)}(\mathbf{r}^n) \to 1$ for all n. Recall, that this is not the case in the canonical description. If the system is homogeneous and isotropic, the 2-particle distribution function, again, is simply denoted by $g(r)$. In the thermodynamic limit canonical and grand canonical descriptions become equivalent and, thus, we denote the radial distribution function from now on as $g(r)$, irrespective of which ensemble was used for the derivation.

Based on the radial distribution function $g(r)$, the so-called cavity distribution function $y(r)$ can be defined:

$$y(r) = \exp\Big[\beta v(r)\Big] g(r), \tag{3.8}$$

where $v(r)$ is the corresponding particle-particle interaction potential. If we imagine a so-called mixed system in which for one fixed pair of particles the interaction is suppressed while all

other interactions remain the same, we can interpret the function $y(r)$ as the distribution function of this pair of non-interacting particles. In a hard-sphere system these two particles correspond to two spheres which can overlap each other but can not overlap the other particles. This leads to the interpretation of the two particles as spherical cavities in the fluid; hence, the name cavity distribution function. Furthermore, $y(r)$ is a continuous function of the center-to-center particle distance r even for hard spheres [17]. This is remarkable, since for hard spheres the particle-particle interaction potential and the radial distribution function are discontinuous at $r = \sigma$. Figure 3.1 shows the plots of the cavity distribution function y and the radial distribution function g of a one component hard-sphere fluid at $\eta = 0.1$, the data for which was derived through a MC simulation in the canonical ensemble and by means of a DFT calculation, respectively. One can clearly see the cavity distribution function to be continuous on the entire range of r, and that outside the hard core, where the hard-sphere interaction potential vanishes, the two functions are equal.

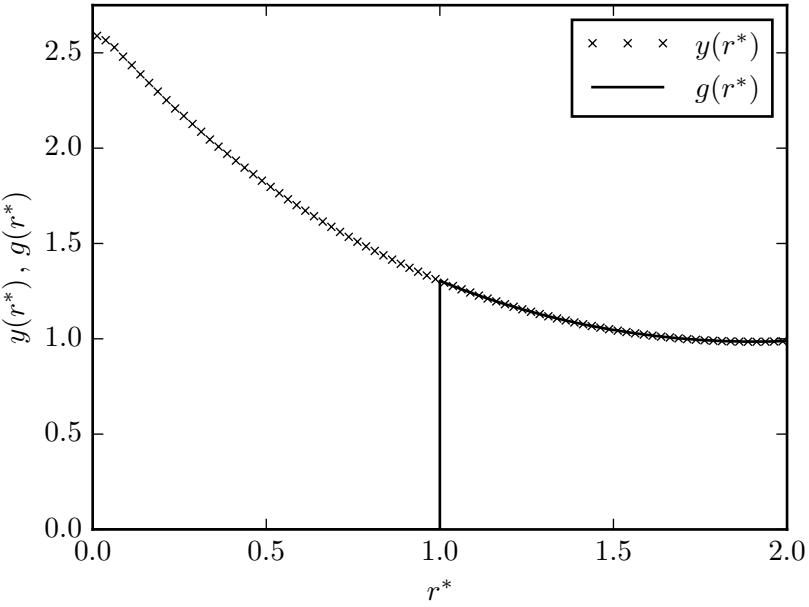

Figure 3.1.: The cavity distribution function $y(r^*)$ (crosses) and the radial distribution function $g(r^*)$ (solid line) of a one-component hard-sphere fluid at $\eta = 0.1$ as functions of the reduced center-to-center particle distance $r^* = r/\sigma$. The data for $y(r^*)$ was calculated by means of a MC simulation in the canonical ensemble, whereas the data for $g(r^*)$ was derived through a DFT calculation.

4. Density functional theory

4.1. Basic concept

Classical density functional theory (DFT) is a theory defined in the grand canonical ensemble. The core of DFT are the two facts that (i) for a statistical system a functional $\Omega[\rho(\mathbf{r})]$ of the spatial number density $\rho(\mathbf{r})$ exists which (ii) is minimal at the equilibrium density, for which it takes the value of the grand potential Ω of the system. I.e. if a functional $\Omega[\rho(\mathbf{r})]$ is given for a particular system, the equilibrium density and the grand potential of the system can be computed by minimizing the functional. To do so, the equation

$$\frac{\delta\Omega[\rho(\mathbf{r})]}{\delta\rho(\mathbf{r})} = 0 \tag{4.1}$$

must be solved for the density profile $\rho(\mathbf{r})$, where $\delta\Omega[\rho(\mathbf{r})]/\delta\rho(\mathbf{r}')$ denotes the functional derivative of the functional $\Omega[\rho(\mathbf{r})]$ with respect to the density profile. In practice, Eq. (4.1) is solved numerically by applying e.g. a Piccard iteration. The expression of the functional of the grand potential reads as follows [11]:

$$\Omega[\rho(\mathbf{r})] = \mathcal{F}[\rho(\mathbf{r})] + \int \mathrm{d}\mathbf{r}\, \rho(\mathbf{r}) \big[V_{\mathrm{ext}}(\mathbf{r}) - \mu\big], \tag{4.2}$$

where $\mathcal{F}[\rho(\mathbf{r})]$ is the unique functional of the intrinsic free energy, $V_{\mathrm{ext}}(\mathbf{r})$ is the external potential, and μ is the particle reservoir's chemical potential. The functional $\mathcal{F}[\rho(\mathbf{r})]$ can be written as

$$\mathcal{F}[\rho(\mathbf{r})] = \mathcal{F}^{\mathrm{id}}[\rho(\mathbf{r})] + \mathcal{F}^{\mathrm{ex}}[\rho(\mathbf{r})], \tag{4.3}$$

i.e. as the sum of the exact intrinsic free energy functional of the ideal gas,

$$\mathcal{F}^{\mathrm{id}}[\rho(\mathbf{r})] = k_{\mathrm{B}}T \int \mathrm{d}\mathbf{r}\, \rho(\mathbf{r}) \Big[\ln\left[\Lambda^3 \rho(\mathbf{r})\right] - 1 \Big], \tag{4.4}$$

and the excess (over the ideal gas) intrinsic free energy functional $\mathcal{F}^{\mathrm{ex}}[\rho(\mathbf{r})]$. The latter contains all information about the particle-particle interaction and in general its exact expression is unknown. Finding approximate expressions for $\mathcal{F}^{\mathrm{ex}}$ is the core challenge of DFT and will be the topic in Secs. 4.2 and 7.1.1. With the expression of the functional of the grand potential given by Eqs. (4.2), (4.3), and (4.4), Eq. (4.1) becomes[1]

$$\ln\left(\frac{\rho(\mathbf{r})}{\rho_{\mathrm{b}}}\right) + \frac{\delta\beta\mathcal{F}^{\mathrm{ex}}[\rho(\mathbf{r})]}{\delta\rho(\mathbf{r}')} + \beta V_{\mathrm{ext}}(\mathbf{r}) - \beta\mu^{\mathrm{ex}} = 0, \tag{4.5}$$

and is called the Euler-Lagrange equation of DFT. The quantity ρ_{b} is the bulk density of the system.

[1] With the expressions in Eqs. (4.2) and (4.3) the functional derivative of $\Omega[\rho(\mathbf{r})]$ is

$$\frac{\delta\Omega[\rho(\mathbf{r})]}{\delta\rho(\mathbf{r}')} = \frac{\delta\mathcal{F}^{\mathrm{id}}[\rho(\mathbf{r})]}{\delta\rho(\mathbf{r}')} + \frac{\delta\mathcal{F}^{\mathrm{ex}}[\rho(\mathbf{r})]}{\delta\rho(\mathbf{r}')} + \frac{\delta}{\delta\rho(\mathbf{r}')} \int \mathrm{d}\mathbf{r}\, \rho(\mathbf{r}) \big[V_{\mathrm{ext}}(\mathbf{r}) - \mu \big].$$

With Eq. (4.4), we find $\frac{\delta\mathcal{F}^{\mathrm{id}}[\rho(\mathbf{r})]}{\delta\rho(\mathbf{r}')} = k_{\mathrm{B}}T \ln\left[\Lambda^3\rho(\mathbf{r})\right]$, and the functional derivative of the integral in the last term yields $(V_{\mathrm{ext}}(\mathbf{r}) - \mu)$. Furthermore, we make use of the identiy $\mu = \mu^{\mathrm{id}} + \mu^{\mathrm{ex}}$, where $\mu^{\mathrm{id}} = k_{\mathrm{B}}T \ln\left[\Lambda^3\rho_{\mathrm{b}}\right]$. With this, we obtain

$$\begin{aligned}\frac{\delta\Omega[\rho(\mathbf{r})]}{\delta\rho(\mathbf{r}')} &= k_{\mathrm{B}}T \ln\left[\Lambda^3\rho(\mathbf{r})\right] + \frac{\delta\mathcal{F}^{\mathrm{ex}}[\rho(\mathbf{r})]}{\delta\rho(\mathbf{r}')} + V_{\mathrm{ext}}(\mathbf{r}) - k_{\mathrm{B}}T \ln\left[\Lambda^3\rho_{\mathrm{b}}\right] - \mu^{\mathrm{ex}} \\ &= k_{\mathrm{B}}T \ln\left[\rho(\mathbf{r})/\rho_{\mathrm{b}}\right] + \frac{\delta\mathcal{F}^{\mathrm{ex}}[\rho(\mathbf{r})]}{\delta\rho(\mathbf{r}')} + V_{\mathrm{ext}}(\mathbf{r}) - \mu^{\mathrm{ex}}.\end{aligned}$$

4.1.1. Generalization for mixtures

Thus far, our treatment of DFT was limited to fluids with one particle species; the generalization for mixtures is straight forward, though. For a fluid comprised of ν particle species (ν-component fluid) with corresponding one-particle densities $\rho_j(\mathbf{r})$, where $j = 1, 2, \ldots, \nu$, the functional of the grand potential reads as follows:

$$\Omega[\{\rho_i\}] = k_\mathrm{B}T \sum_{j=1}^{\nu} \int \mathrm{d}\mathbf{r}\, \rho_j(\mathbf{r}) \Big[\ln\left[\Lambda_j^3 \rho_j(\mathbf{r})\right] - 1 \Big] + \mathcal{F}^{\mathrm{ex}}[\{\rho_j\}] + \sum_{j=1}^{\nu} \int \mathrm{d}\mathbf{r}\, \rho_j(\mathbf{r}) [V_{\mathrm{ext},j}(\mathbf{r}) - \mu_j].$$

In this case, Eq. (4.1) generalizes to be a system of ν coupled equations,

$$\frac{\delta\Omega}{\delta\rho_j(\mathbf{r})} = 0, \qquad j = 1, 2, \ldots, \nu,$$

which has to be solved to minimize $\Omega[\{\rho_i\}]$.

4.2. Fundamental measure theory

Fundamental measure theory (FMT) is an accurate framework to gain an (approximate) expression for the intrinsic excess free energy $\mathcal{F}^{\mathrm{ex}}$ for hard-sphere mixtures, and was originally derived by Rosenfeld [30]. Since hard-sphere systems are often applied as reference systems in the perturbation theory of fluids with soft tail, or in colloidal systems, FMT plays a central role in DFT.

For a ν-component hard-sphere mixture, where the density profile of the species with number i is $\rho_i(\mathbf{r})$, Rosenfeld's ansatz for $\mathcal{F}^{\mathrm{ex}}$ is

$$\beta\mathcal{F}^{\mathrm{ex}}[\{\rho_i\}] = \int \mathrm{d}\mathbf{r}\, \Phi\Big(\{n_\alpha(\mathbf{r})\}\Big), \tag{4.6}$$

where the weighted densities $n_\alpha(\mathbf{r})$ are given by

$$n_\alpha(\mathbf{r}) = \sum_{i=1}^{\nu} n_\alpha^{(i)}(\mathbf{r}) = \sum_{i=1}^{\nu} \int \mathrm{d}\mathbf{r}'\, \rho_i(\mathbf{r}')\omega_\alpha^{(i)}(\mathbf{r}-\mathbf{r}'), \tag{4.7}$$

with the weight functions of species i:

$$\begin{aligned}
\omega_3^{(i)}(\mathbf{r}) &= \Theta(R_i - r), \\
\omega_2^{(i)}(\mathbf{r}) &= \delta(R_i - r), \\
\omega_1^{(i)}(\mathbf{r}) &= \frac{1}{4\pi R_i}\omega_2^{(i)}(\mathbf{r}), \\
\omega_0^{(i)}(\mathbf{r}) &= \frac{1}{4\pi R_i^2}\omega_2^{(i)}(\mathbf{r}),
\end{aligned}
\qquad
\begin{aligned}
\boldsymbol{\omega}_{\mathrm{v}2}^{(i)}(\mathbf{r}) &= \frac{\mathbf{r}}{r}\delta(R_i - r), \\
\boldsymbol{\omega}_{\mathrm{v}1}^{(i)}(\mathbf{r}) &= \frac{1}{4\pi R_i}\boldsymbol{\omega}_{\mathrm{v}2}^{(i)}(\mathbf{r}).
\end{aligned}$$

The function $\Theta(r)$ is the Heaviside step function, $\delta(r)$ the Dirac-delta distribution and $R_i = \sigma_i/2$ the radius of the hard spheres of species i with diameter σ_i. In the bulk limit, the scalar weighted densities reduce to the constant scaled particle theory (SPT) variables,

$$\begin{aligned}
\lim_{\rho_i(\mathbf{r})\to\rho_{\mathrm{b}}^{(i)}} n_3(\mathbf{r}) &= \sum_i \frac{4\pi R_i^3}{3}\rho_{\mathrm{b}}^{(i)}, \\
\lim_{\rho_i(\mathbf{r})\to\rho_{\mathrm{b}}^{(i)}} n_2(\mathbf{r}) &= \sum_i 4\pi R_i^2 \rho_{\mathrm{b}}^{(i)}, \\
\lim_{\rho_i(\mathbf{r})\to\rho_{\mathrm{b}}^{(i)}} n_1(\mathbf{r}) &= \sum_i R_i \rho_{\mathrm{b}}^{(i)}, \\
\lim_{\rho_i(\mathbf{r})\to\rho_{\mathrm{b}}^{(i)}} n_0(\mathbf{r}) &= \sum_i \rho_{\mathrm{b}}^{(i)},
\end{aligned} \tag{4.8}$$

where $\rho_{\mathrm{b}}^{(i)}$ is the bulk density of species i. The vector weighted densites vanish in the bulk limit, i.e.,

$$\lim_{\rho_i(\mathbf{r})\to\rho_{\mathrm{b}}^{(i)}} \mathbf{n}_{\mathrm{v}1,\mathrm{v}2}(\mathbf{r}) = 0.$$

The excess free energy density Φ in Rosenfeld's functional is

$$\Phi^{\mathrm{Ro}}\Big(\{n_\alpha(\mathbf{r})\}\Big) = -n_0\,\ln(1-n_3)+\frac{n_1n_2-\mathbf{n}_1\cdot\mathbf{n}_2}{1-n_3}+\frac{n_2^3-3n_2\mathbf{n}_2\cdot\mathbf{n}_2}{24\pi(1-n_3)^2}.$$

The equation of state resulting from the Rosenfeld functional is the compressibility expression from the solution of the Percus-Yevick integral equations, namely

$$\beta p = \frac{n_0}{1-n_3}+\frac{n_1n_2}{(1-n_3)^2}+\frac{n_2^3}{12\pi(1-n_3)^3}, \tag{4.9}$$

which in bulk and for a one-component system reduces to

$$\frac{\beta p}{\rho} = \frac{1+\eta+\eta^2}{(1-\eta)^3}.$$

Equation 4.9 is in good agreement with simulation results of hard-sphere fluids at low densities, however, deviates from the exact result by about 7 % at densities close to the freezing transition. Furthermore the Rosenfeld functional fails to describe hard-sphere crystals.

To overcome the shortcoming of the Rosenfeld functional to accurately describe the hard-sphere liquid at high densities, Roth et al. [31] constructed the White Bear functional which is of the same form as Eq. (4.6) but the excess free energy density Φ now is

$$\begin{aligned}\Phi^{\mathrm{WB}}\Big(\{n_\alpha(\mathbf{r})\}\Big) = &-n_0\ln(1-n_3)+\frac{n_1n_2-\mathbf{n}_1\cdot\mathbf{n}_2}{1-n_3}\\ &+(n_2^3-3n_2\mathbf{n}_2\cdot\mathbf{n}_2)\frac{n_3+(1-n_3)^2\ln(1-n_3)}{36\pi n_3^2(1-n_3)^2}.\end{aligned}$$

The White Bear functional provides improved results for thermodynamic quantities by virtue of the underlying Mansoori-

Carnahan- Starling-Leland (MCSL) equation of state, however does not satisfy the SPT differential equation ($\partial\Phi/\partial n_3 = \beta p$ in bulk) used in the derivation of the Rosenfeld functional [30].

To overcome the inconsistency regarding the SPT differential equation, the White Bear version of FMT mark II was constructed by Hansen-Goos et al. [18]. The mark II excess free energy density reads

$$\begin{aligned}\Phi^{\mathrm{WBII}}\Big(\{n_\alpha(\mathbf{r})\}\Big) = &-n_0\ln(1-n_3)\\ &+(n_1n_2-\mathbf{n}_1\cdot\mathbf{n}_2)\frac{1+\frac{1}{3}\phi_2(n_3)}{1-n_3}\\ &+(n_2^3-3n_2\mathbf{n}_2\cdot\mathbf{n}_2)\frac{1-\frac{1}{3}\phi_3(n_3)}{24\pi(1-n_3)^2},\end{aligned}$$

where

$$\phi_2(n_3) = \frac{1}{n_3}(2n_3 - n_3^2 + 2(1-n_3)\ln(1-n_3)),$$

and

$$\phi_3(n_3) = \frac{1}{n_3^2}(2n_3 - 3n_3^2 + 2n_3^3 + 2(1-n_3)^2\ln(1-n_3)).$$

Here, for a one-component fluid the SPT differential equation reduces to the Carnahan-Starling (CS) equation of state:

$$\frac{\partial\Phi^{\mathrm{WBII}}}{\partial n_3} = \beta p_{\mathrm{CS}} = \rho\frac{1+\eta+\eta^2-\eta^3}{(1-\eta)^3}.$$

5. Computation of the radial distribution function

The radial distribution functions $g(r)$, introduced in Secs. 2.2 and 3.2, of various homogeneous isotropic fluids are pivotal in this work. In Chpts. 6 and 7 the hard-sphere radial distribution function and the radial distribution function of the Jagla ramp fluid, the latter being a fluid in which the pairwise particle-particle interaction potential is given by the repulsive part of the Jagla potential, are the central quantities to establish perturbation theories which go beyond the standard mean-field approximation. In Chpt. 8 the radial distribution function of the Jagla fluid is employed to transfer information from the exact Monte-Carlo (MC) simulation results to DFT.

In this section the two numerical schemes applied to compute $g(r)$ in this work, namely via DFT calculations and within MC simulations, are commented on.

5.1. Density functional theory calculation

The basis of the computation of the radial distribution function $g(r)$ of a homogeneous isotropic fluid through DFT is the interpretation [17] of the quantity $\rho g(r)$ as the single particle density around a reference particle of the fluid which is assumed to be fixed at the origin. The other particles of the system thus move

in the force field constituted by the interaction between them and the reference particle.

This scenario is also called the test particle geometry, and can be implemented in a DFT calculation, if the external potential in the functional of the grand potential $\Omega[\rho(\mathbf{r})]$ in Eq. (4.2) is chosen to be the particle-particle interaction potential of a particle located at the origin. Since the interaction potential is assumed to be isotropic, the resulting density profile $\rho(r)$ around the particle at the origin will be radially symmetric. If a radially symmetric density profile $\rho(r)$ is assumed in the expressions for the functional of the grand potential and its derivative, the problem reduces from three dimensions to one dimension which considerably simplifies its implementation. Once $\rho(r)$ is obtained, the radial distribution function can be calculated by dividing the density profile by the previously chosen bulk density:

$$g(r) = \frac{1}{\rho}\rho(r).$$

As always with DFT, the accuracy of the result depends on the quality of the applied (approximate) functional $\mathcal{F}^{\mathrm{ex}}[\rho(\mathbf{r})]$ of the excess intrinsic free energy.

5.2. Monte-Carlo simulation calculation

Given a working MC simulation program which samples the isotropic bulk fluid of interest in the chosen statistical ensemble (canonical or grand canonical) correctly, the corresponding radial distribution function can be computed as follows. Here, again, the interpretation of $\rho g(r)$ as the single-particle density $\rho(r)$ around a reference particle in the fluid is utilized (see Sec. 2.2). Note, however, that now, unlike for the DFT calculation, the reference

particle is not fixed in space. The first step is to determine the density profile $\rho(r)$ from which $g(r)$ can easily be calculated through a division by the bulk density ρ.

5.2.1. Canonical ensemble

The idea to obtain a discretized version of the radially symmetric density profile $\rho(r)$ around the reference particle is to determine the mean number of particles inside the spherical shells[1] around the reference particle which subsequently is divided by the volume of the corresponding shell. Be Δr the thickness of the shells, then shell number m, where $m = 0, 1, 2, 3, \ldots$, contains all distances r in the interval $[r_m, r_m + \Delta r)$, where $r_m = m\,\Delta r$. The volume of shell number m then is

$$V_m = \frac{4}{3}\pi\Big[(r_m + \Delta r)^3 - r_m^3\Big] = \frac{4}{3}\pi(\Delta r)^3\Big[(m+1)^3 - m^3\Big].$$

Now, after every, lets say, 100 MC steps (this worked fine in the codes applied for this work in which every particle is attempted to be moved once in every MC step) an evaluation cycle is done in which the number of particles in the shells is counted.

The simplest implementation of an evaluation cycle is to evaluate the distances between the reference particle and all other $(N-1)$ particles (we assume a system with N particles in total). I.e. there is $(N-1)$ evaluations per evaluation cycle, namely one evaluation for each pair. If, e.g. the distance r_i between the reference particle and particle number i ($i = 1, 2, \ldots, N-1$) lies in the interval $[r_m, r_m + \Delta r)$ with number m, the count for shell m goes up by one. Be N_e the total number of evaluation cycles, and be n_m the total count of particles in shell number m after all N_e evaluations (note that we do *not* reset the count

[1] In statistics, what we refer to as shell here is usually called a bin.

after one evaluation cycle). Then the average number of particles in shell m is $\bar{n}_m = n_m/N_e$. This evaluation cycle is simple but also inefficient, as it takes relatively long to converge to the exact result.

A more sophisticated evaluation cycle makes use of the fact that the choice of the reference particle is arbitrary, and, in one evaluation, we now do not only evaluate the $(N-1)$ distances between one reference particle and the other particles, but evaluate the distances of all possible $N(N-1)/2$ pairs of particles. This makes the calculation of the radial distribution function much more efficient as the count n_m increases much faster (by a factor of $N/2$ as we will now show). Now, there obviously is $N(N-1)/2$ evaluations per evaluation cycle which is a factor of $N/2$ more evaluations than before when only $(N-1)$ evaluations were carried out. This we have to take into account in the calculation of the mean number $\bar{n}_m$ of particles in shell m by means of a division by $N/2$:

$$\bar{n}_m = \frac{n_m}{N_e \frac{N}{2}}.$$

With this, the mean density in shell m is

$$\rho_m = \frac{\bar{n}_m}{V_m} = \frac{n_m}{\frac{4}{3}\pi(\Delta r)^3\Big[(m+1)^3 - m^3\Big]N_e\frac{N}{2}},$$

and the discrete value of the radial distribution function in shell m consequently reads as

$$g_m = \frac{\rho_m}{\rho} = \frac{n_m}{\rho\frac{2}{3}\pi(\Delta r)^3\Big[(m+1)^3 - m^3\Big]N_e N}.$$

5.2.2. Grand canonical ensemble

In a grand canonical MC simulation the number of particles varies which must be taken into account in the calculation of $\bar{n}_m$. To calculate $\bar{n}_m$ in the canonical simulation, n_m is divided by $N_e N/2 = \sum_{j=1}^{N_e} N/2$, where j counts the evaluation cycles. For a variable number of particles in the simulation, N must be replaced by N_j which is the number of particles in the system when the j-th evaluation cycle is carried out. Consequently we find

$$\bar{n}_m = \frac{n_m}{\sum_{j=1}^{N_e} \frac{N_j}{2}},$$

and, thus,

$$g_m = \frac{n_m}{\rho \frac{2}{3}\pi(\Delta r)^3 \left[(m+1)^3 - m^3\right] \sum_{j=1}^{N_e} N_j}.$$

Part II.

Towards a DFT for the Jagla fluid

6. Bulk phase diagram[1]

6.1. Perturbation theory in bulk

6.1.1. Derivation

Our starting point for a perturbation description of the Jagla fluid's bulk properties, and especially its bulk phase behavior, is the so called λ-expansion, explicitly described in Ref. [17] which we follow closely here. For the derivation of the λ-expansion, we first consider a canonical ensemble (see Chpt. 2), where the number of particles N in the system and the system's volume V and temperature T are held constant. Later, to derive the second order term of the λ-expansion, we will switch to a grand canonical description (see Chpt. 3). Note, however, that canonical and grand canonical descriptions become equivalent in the thermodynamic limit. To start with, we assume a pairwise additive particle-particle interaction potential of the form

$$v_\lambda(r_{12}) = v_0(r_{12}) + \lambda w(r_{12}). \tag{6.1}$$

Here, $v_0(r_{12})$ is the interaction potential of a reference system, the properties of which are assumed to be known, $r_{12} = |\mathbf{r}_2 - \mathbf{r}_1|$, and $w(r_{12})$ is considered to be a perturbation added to $v_0(r_{12})$.

[1] At the date of printing, content of this chapter is accepted as a Regular Article in Physical Review E with the title "Towards a density functional theory for the Jagla fluid" by Florian Gußmann, S. Dietrich and Roland Roth.

The parameter $\lambda \in [\lambda_1, \lambda_2] = [0, 1]$ is a coupling parameter which, if increased from 0 to 1, gradually turns on the perturbation, such that

$$v_{(\lambda=1)}(r_{12}) = v_0(r_{12}) + w(r_{12}) = v_{\mathrm{J}}(r_{12}).$$

With this, the interatomic potential energy of a system of N particles intercacting via the potential in Eq. (6.1) is

$$V_N(\mathbf{r}^N; \lambda) = \sum_{i=1}^{N} \sum_{j>i}^{N} v_\lambda(r_{ij}). \tag{6.2}$$

If $V_N(\mathbf{r}^N; \lambda)$ is plugged in the expression for F^{ex} [Eq. (2.12)] via the configuration integral Z_N [Eq. (2.6)], the derivative of $F^{\mathrm{ex}}(\lambda)$ with respect to the coupling parameter λ is[2]

$$\begin{aligned} \beta \frac{\partial F^{\mathrm{ex}}(\lambda)}{\partial \lambda} &= \frac{1}{Z_N(\lambda)} \int \exp\big[-\beta V_N(\lambda)\big] \beta V_N'(\lambda) \mathrm{d}\mathbf{r}^N \\ &\overset{(2.7)}{=} \beta \big\langle V_N'(\lambda) \big\rangle_\lambda . \end{aligned} \tag{6.3}$$

[2]

$$\begin{aligned} \beta \frac{\partial F^{\mathrm{ex}}(\lambda)}{\partial \lambda} &\overset{(2.12)}{=} -\frac{\partial}{\partial \lambda} \ln \frac{Z_N(\lambda)}{V^N} \\ &= -\frac{V^N}{Z_N(\lambda)} \frac{\partial}{\partial \lambda} \frac{Z_N(\lambda)}{V^N} \\ &\overset{(2.6)}{=} -\frac{1}{Z_N(\lambda)} \int \mathrm{d}\mathbf{r}^N \frac{\partial}{\partial \lambda} \exp\big(-\beta V_N(\lambda)\big) \\ &= \frac{1}{Z_N(\lambda)} \int \mathrm{d}\mathbf{r}^N \exp\big(-\beta V_N(\lambda)\big) \beta \underbrace{\frac{\partial}{\partial \lambda} V_N(\lambda)}_{\equiv V_N'(\lambda)} \\ &\overset{(2.7)}{=} \beta \big\langle V_N'(\lambda) \big\rangle \end{aligned}$$

where $V_N'(\lambda) \equiv \partial V_N(\lambda)/\partial\lambda$ and $\langle \dots \rangle_\lambda$ denotes the ensemble average in the system with particle-particle interaction potential $v_\lambda(r_{12})$. Integration[3] of the derivative of $F^{\mathrm{ex}}(\lambda)$ [Eq. (6.3)] is the first step to gain an expansion of the excess free energy:

$$\beta F^{\mathrm{ex}}(\lambda_1) = \beta F_0^{\mathrm{ex}} + \beta \int_{\lambda_0}^{\lambda_1} \langle V_N'(\lambda) \rangle_\lambda \, \mathrm{d}\lambda, \tag{6.4}$$

where $F_0^{\mathrm{ex}} \equiv F^{\mathrm{ex}}(\lambda_0)$ is the excess free energy of the reference system. The second step is to expand the ensemble average $\langle V_N'(\lambda) \rangle_\lambda$ in a series around its value for $\lambda = \lambda_0$:

$$\begin{aligned} \langle V_N'(\lambda) \rangle_\lambda = \langle V_N'(\lambda) \rangle_\lambda \Big|_{\lambda=\lambda_0} + (\lambda - \lambda_0) \left. \frac{\partial \langle V_N'(\lambda) \rangle_\lambda}{\partial \lambda} \right|_{\lambda=\lambda_0} \\ + \mathcal{O}(\lambda - \lambda_0)^2. \end{aligned} \tag{6.5}$$

[3] Here, we have got a partial differential equation,

$$\frac{\partial F^{\mathrm{ex}}(\lambda)}{\partial \lambda} \overset{(6.3)}{=} \langle V_N'(\lambda) \rangle_\lambda,$$

which can be solved by solving the corresponding characteristic system:

$$\begin{aligned} \frac{\mathrm{d}\lambda}{1} &= \frac{\mathrm{d}F^{\mathrm{ex}}}{\langle V_N'(\lambda) \rangle_\lambda} \\ \Leftrightarrow \mathrm{d}F^{\mathrm{ex}} &= \langle V_N'(\lambda) \rangle_\lambda \mathrm{d}\lambda \\ \Leftrightarrow \int_{F^{\mathrm{ex}}(\lambda=\lambda_1)}^{F^{\mathrm{ex}}(\lambda=\lambda_0)} \mathrm{d}F^{\mathrm{ex}} &= \int_{\lambda_0}^{\lambda_1} \langle V_N'(\lambda) \rangle_\lambda \mathrm{d}\lambda \\ \Leftrightarrow F^{\mathrm{ex}}(\lambda_1) &= \underbrace{F^{\mathrm{ex}}(\lambda_0)}_{\equiv F_0^{\mathrm{ex}}} + \int_{\lambda_0}^{\lambda_1} \langle V_N'(\lambda) \rangle_\lambda \, \mathrm{d}\lambda. \end{aligned}$$

The derivative of the ensemble average $\langle V_N'(\lambda)\rangle_\lambda$ with respect to λ in Eq. (6.5) is (see App. B.1)

$$\frac{\partial\langle V_N'(\lambda)\rangle_\lambda}{\partial\lambda} = \langle V_N''(\lambda)\rangle_\lambda - \beta\Big(\langle[V_N'(\lambda)]^2\rangle_\lambda - \langle V_N'(\lambda)\rangle_\lambda^2\Big). \quad (6.6)$$

Insertion of Eq. (6.6) and Eq. (6.5) in Eq. (6.4) gives an expansion of the excess free energy in powers of $(\lambda_1 - \lambda_0)$:

$$\begin{aligned}\beta F^{\mathrm{ex}}(\lambda_1) = \beta F_0^{\mathrm{ex}} &+ (\lambda_1-\lambda_0)\beta\,\langle V_N'(\lambda)\rangle_\lambda\Big|_{\lambda=\lambda_0} \\ &+ \frac{1}{2}(\lambda_1-\lambda_0)^2\Bigg(\beta\,\langle V_N''(\lambda)\rangle_\lambda\Big|_{\lambda=\lambda_0} \\ &\quad - \beta^2\Big(\,\langle[V_N'(\lambda)]^2\rangle_\lambda\Big|_{\lambda=\lambda_0} - \langle V_N'(\lambda)\rangle_\lambda^2\Big|_{\lambda=\lambda_0}\Big)\Bigg) \\ &+ \mathcal{O}(\lambda_1-\lambda_0)^3.\end{aligned}$$

If we substitute λ_1 and λ_0 for their numerical values, namely 1 and 0, respectively, the expression for the excess free energy simplifies to be

$$\begin{aligned}\beta F^{\mathrm{ex}}(\lambda{=}1) = \beta F_0^{\mathrm{ex}} &+ \beta\langle V_N'(\lambda{=}0)\rangle_0 \\ &+ \frac{1}{2}\Big(\beta\langle V_N''(\lambda{=}0)\rangle_0 - \beta^2\Big(\langle[V_N'(\lambda{=}0)]^2\rangle_0 \\ &\qquad - \langle V_N'(\lambda{=}0)\rangle_0^2\Big)\Big) + \mathcal{O}(\beta^3), \qquad (6.7)\end{aligned}$$

where $\langle\dots\rangle_0$ denotes the ensemble average in the reference system. We now define the total perturbation energy for $\lambda = 1$ as

$$W_N = \sum_{i=1}^{N}\sum_{j>i}^{N} w(r_{ij}), \quad (6.8)$$

from which follows[4] that $V_N' = W_N$ and $V_N'' = 0$. This lets us further simplify the expression in Eq. (6.7) to be

$$\begin{aligned}\beta F^{\mathrm{ex}} &\approx \beta F_0^{\mathrm{ex}} + \beta\langle W_N\rangle_0 - \frac{1}{2}\beta^2\Big(\langle W_N^2\rangle_0 - \langle W_N\rangle_0^2\Big) + \mathcal{O}(\beta^3) \\ &\equiv \beta F_0^{\mathrm{ex}} + \beta F_1^{\mathrm{ex}} + \beta F_2^{\mathrm{ex}} + \mathcal{O}(\beta^3). \end{aligned} \tag{6.9}$$

Equation (6.9) is called the high temperature expansion; note, however, that in general β is not the only temperature dependent variable in the expression since the ensemble averages are also functions of the temperature. While a temperature expansion of the excess free energy F^{ex} is certainly helpful for practical applications, especially if higher order terms can be neglected, the form of (6.9) is not, as it involves the summation over all particles in the system. Hence, we make use of the fact that we assume a pairwise additive particle-particle interaction potential to rewrite

[4] It is

$$\begin{aligned} V_N(\lambda) &= \sum_{i=1}^{N}\sum_{j>i}^{N} v_\lambda(r_{ij}). \\ &= \sum_{i=1}^{N}\sum_{j>i}^{N}\Big(v_0(r_{ij}) + \lambda w(r_{ij})\Big) \\ &= \sum_{i=1}^{N}\sum_{j>i}^{N} v_0(r_{ij}) + \lambda \underbrace{\sum_{i=1}^{N}\sum_{j>i}^{N} w(r_{ij})}_{=W_N}. \end{aligned}$$

And with this

$$\begin{aligned} V_N'(\lambda) &= \frac{\partial}{\partial\lambda} V_N(\lambda) = W_N, \text{and} \\ V_N''(\lambda) &= \frac{\partial^2}{\partial\lambda^2} V_N(\lambda) = \frac{\partial}{\partial\lambda} W_N = 0. \end{aligned}$$

the first and second order expressions of the high temperature expansion in terms of the radial distribution function $g(r)$. For this we consider the integral term in Eq. (6.4) once more,

$$\begin{aligned}\beta F^{\mathrm{ex}} &= \beta F_0^{\mathrm{ex}} + \beta \int_0^1 \left\langle V_N'(\lambda) \right\rangle_\lambda \mathrm{d}\lambda \\ &\overset{\text{Fn. 4}}{=} \beta F_0^{\mathrm{ex}} + \beta \int_0^1 \left\langle W_N \right\rangle_\lambda \mathrm{d}\lambda, \end{aligned} \tag{6.10}$$

and rewrite the ensemble average of W_N to be (see App. B.2)

$$\left\langle W_N \right\rangle_\lambda = \frac{1}{2} \iint \rho_{N;\lambda}^{(2)}(\mathbf{r}_1, \mathbf{r}_2) w(r_{12}) \mathrm{d}\mathbf{r}_1 \mathrm{d}\mathbf{r}_2, \tag{6.11}$$

where $\rho_{N;\lambda}^{(2)}(\mathbf{r}_1, \mathbf{r}_2)$ is the canonical 2-particle density [Eq. (2.13)] of the system with interaction potential $v_\lambda(r_{12})$. Now, we plug Eq. (6.11) back in Eq. (6.10) and obtain

$$F^{\mathrm{ex}} = \beta F_0^{\mathrm{ex}} + \frac{\beta}{2} \int_0^1 \mathrm{d}\lambda \iint \rho_{N;\lambda}^{(2)}(\mathbf{r}_1, \mathbf{r}_2) w(r_{12}) \mathrm{d}\mathbf{r}_1 \mathrm{d}\mathbf{r}_2. \tag{6.12}$$

Finally, we expand the 2-particle density in powers of λ,

$$\rho_{N;\lambda}^{(2)}(\mathbf{r}_1, \mathbf{r}_2) = \rho_{N;0}^{(2)}(\mathbf{r}_1, \mathbf{r}_2) + \lambda \left. \frac{\partial \rho_{N;\lambda}^{(2)}(\mathbf{r}_1, \mathbf{r}_2)}{\partial \lambda} \right|_{\lambda=0} + \mathcal{O}(\lambda^2),$$

where $\rho_{N;0}^{(2)}(\mathbf{r}_1, \mathbf{r}_2)$ is the 2-particle density of the reference system, and plug the expansion back in Eq. (6.12) which yields

$$\begin{aligned} F^{\mathrm{ex}} = \beta F_0^{\mathrm{ex}} &+ \frac{\beta}{2} \iint \rho_{N;0}^{(2)}(\mathbf{r}_1, \mathbf{r}_2) w(r_{12}) \mathrm{d}\mathbf{r}_1 \mathrm{d}\mathbf{r}_2 \\ &+ \frac{\beta}{4} \iint \left. \frac{\partial \rho_{N;\lambda}^{(2)}(\mathbf{r}_1, \mathbf{r}_2)}{\partial \lambda} \right|_{\lambda=0} w(r_{12}) \mathrm{d}\mathbf{r}_1 \mathrm{d}\mathbf{r}_2 + \mathcal{O}(\lambda^3). \end{aligned} \tag{6.13}$$

By comparison of Eqs. (6.13) and (6.9), we obtain[5] for the first order term

$$\begin{aligned}\frac{\beta F_1^{\mathrm{ex}}}{N} &= \frac{\beta}{2N}\iint \rho^{(2)}_{N;0}(\mathbf{r}_1,\mathbf{r}_2)w(r_{12})\mathrm{d}\mathbf{r}_1\mathrm{d}\mathbf{r}_2 \\ &= \frac{\beta\rho}{2}\int g_0(r)w(r)\mathrm{d}\mathbf{r} \\ &= 2\pi\rho\int_0^\infty g_0(r)\,\beta w(r)\,r^2\mathrm{d}r, \end{aligned} \tag{6.14}$$

where $g_0(r)$ is the (canonical) radial distribution function of the reference system. The second order term in Eq. (6.13) involves the derivative $\partial\rho^{(2)}_{N;\lambda}(\mathbf{r}_1,\mathbf{r}_2)/\partial\lambda$, the exact expression of which is rather lengthy [17], and, hence, little useful in practice. Thus, we make use of the so called 'compressibility' approximation of the second order term, originally derived by Barker and Henderson [5], and continue to follow closely Ref. [17] for the

[5] The second equality in Eq. (6.14) holds, since

$$\begin{aligned}&\frac{\beta}{2N}\iint \rho^{(2)}_{N;0}(\mathbf{r}_1,\mathbf{r}_2)w(r_{12})\mathrm{d}\mathbf{r}_1\mathrm{d}\mathbf{r}_2 \\ &\overset{(2.19)}{=}\frac{\beta}{2N}\iint \rho^2 g^{(2)}_{N;0}(\mathbf{r}_1,\mathbf{r}_2)w(r_{12})\mathrm{d}\mathbf{r}_1\mathrm{d}\mathbf{r}_2 \\ &= \frac{\beta\rho}{2N}\frac{N}{V}\iint g_0(|\mathbf{r}_2-\mathbf{r}_1|)w(r_{12})\mathrm{d}\mathbf{r}_1\mathrm{d}\mathbf{r}_2 \\ &= \frac{\beta\rho}{2V}\underbrace{\int \mathrm{d}\mathbf{r}_1}_{=V}\int g_0(r)w(r)\mathrm{d}\mathbf{r} \\ &= \frac{\beta\rho}{2}\int g_0(r)w(r)\mathrm{d}\mathbf{r},\end{aligned}$$

where we make use of the fact that the system is homogeneous in the first equality, and that it is isotropic in the second equality. Furthermore, we substitute $(\mathbf{r}_2-\mathbf{r}_1)\to\mathbf{r}$ in the third equality.

corresponding derivation. Since the latter involves the particle fluctuations of an open system, it must be carried out in the grand canonical ensemble; note, however, that canonical and grand canonical descriptions become equivalent in the thermodynamic limit. The aim of the 'compressibility' approximation is to approximately rewrite the second order term of Eq. (6.9) based on a semi-macroscopic argument. For this, the range of possible particle-particle distances r in the reference system is divided into equal intervals $[r_m, r_{m+1}]$ of length $\Delta r = r_{m+1} - r_m$, where $m = 0, 1, 2, \ldots$. Furthermore, be $S_m^{(i)}$ the spherical shell around the particle with number [6] i $(i = 1, \ldots, N)$ including all points with a distance from particle i in the interval $[r_m, r_{m+1}]$. Then, the mean number of particles in all shells, i.e. in the volume $\bigcup_{i=1}^{N} S_m^{(i)}$, is[7]

$$\langle N_m \rangle_0 = 2\pi N \rho \int_{r_m}^{r_{m+1}} g_0(r) r^2 \mathrm{d}r, \tag{6.15}$$

where $g_0(r)$ now is the grand canonical radial distribution function of the reference system. If the interval Δr is sufficiently small,

[6] Since we pursue a grand canonical description N may vary, but is always countable.

[7] The mean number or particles in one shell is:

$$\int_{r_m}^{r_{m+1}} \rho_0(r)\, 4\pi r^2 \mathrm{d}r,$$

where $\rho_0(r) = \rho g_0(r)$ is the radial mean density around one particle in the reference system, and ρ is the bulk density. Since we consider the mean number of particles in all shells, we multiply by N and add a factor of $1/2$ to count each particle-particle interaction only once. Because, if particle number i is in the shell of particle number j, also particle number j is in the shell of particle number i, but the interaction ij must only be counted once; hence the factor of $1/2$. Taken together, we get the expression in Eq. (6.15).

the perturbation potential $w(r)$ will, in good approximation, have the same value w_m at all points inside the shell. With this, the high temperature expansion [Eq. (6.9)] can be rewritten[8] in terms of the mean numbers $\langle N_m \rangle_0$, $(m = 0, 1, 2, \dots)$:

$$\begin{aligned} \beta F^{\text{ex}} = \beta F_0^{\text{ex}} &+ \beta \sum_m \langle N_m \rangle_0 w_m \\ &- \frac{1}{2}\beta^2 \sum_m \sum_n \big(\langle N_m N_n \rangle_0 - \langle N_m \rangle_0 \langle N_n \rangle_0 \big) w_m w_n \\ &+ \mathcal{O}(\beta^3). \end{aligned} \tag{6.16}$$

Barker and Henderson [5] now argue that if the shells were large macroscopic volumes, the number of molecules in different shells would be uncorrelated, i.e.

$$\langle N_m N_n \rangle_0 = \langle N_m \rangle_0 \langle N_n \rangle_0 \qquad m \neq n.$$

[8] The mean $\langle W_N \rangle_0$ in Eq. (6.9) can now be rewritten to be

$$\langle W_N \rangle_0 = \Big\langle \sum_m N_m w_m \Big\rangle_0 = \sum_m \langle N_m \rangle_0 w_m,$$

where the second equality holds, as the mean $\langle \dots \rangle_0$ is a linear operator, and w_m is constant for fixed m. Likewise, in the second order term we have

$$\begin{aligned} \langle W_N^2 \rangle_0 - \langle W_N \rangle_0^2 &= \Big\langle \sum_m \sum_n N_m w_m N_n w_n \Big\rangle_0 \\ &\quad - \Big\langle \sum_m N_m w_m \Big\rangle_0 \Big\langle \sum_n N_n w_n \Big\rangle_0 \\ &= \sum_m \sum_n \big(\langle N_m N_n \rangle_0 - \langle N_m \rangle_0 \langle N_n \rangle_0 \big) w_m w_n. \end{aligned}$$

With this, in the second order term in Eq. (6.16) all terms with $m \neq n$ would be zero and the expression thus would reduce to:

$$\beta F_2^{\mathrm{ex}} = -\frac{1}{2}\sum_m \left(\langle N_m^2\rangle_0 - \langle N_m\rangle_0^2\right)(\beta w_m)^2, \tag{6.17}$$

where $\langle N_m^2\rangle_0 - \langle N_m\rangle_0^2 \equiv \langle \Delta N_m^2\rangle_0$ is the fluctuation in the number of particles in all shells, i.e. in the volume $\bigcup_{i=1}^{N} S_m^{(i)}$. The fluctuation $\langle \Delta N_m^2\rangle_0$ is related to the compressibility χ_T^0 of the reference system via[9]

$$\langle \Delta N_m^2\rangle_0 = \langle N_m\rangle_0 k_{\mathrm{B}} T \rho \chi_T^0.$$

Inserted in the second order expression (6.17), this yields

$$\beta F_2^{\mathrm{ex}} = -\frac{1}{2}\sum_m \langle N_m\rangle_0 k_{\mathrm{B}} T \rho \chi_T^0 (\beta w_m)^2.$$

If we now plug in Eq. (6.15) for $\langle N_m\rangle_0$ and replace the sum by an integral[10], we obtain

$$\frac{\beta F_2^{\mathrm{ex}}}{N} = -\pi \rho k_{\mathrm{B}} T \int_0^\infty [\beta w(r)]^2 \rho \chi_T^0 \, g_0(r) r^2 \mathrm{d}r.$$

[9] See e.g. Eq. (2.4.23) in Ref. [17].

[10] First, $\langle N_m\rangle_0$ is replaced by the expression in Eq. (6.15):

$$\begin{aligned}\beta F_2^{\mathrm{ex}} &= -\frac{1}{2}\sum_m \langle N_m\rangle_0 k_{\mathrm{B}} T \rho \chi_T^0 (\beta w_m)^2 \\ &\overset{(6.15)}{=} -\pi \rho N k_{\mathrm{B}} T \sum_m \int_{r_m}^{r_{m+1}} g_0(r) r^2 \rho \chi_T^0 (\beta w_m)^2 \mathrm{d}r.\end{aligned}$$

Then, the limit $\Delta r \to 0$ is considered from which follows that $w_m \to w(r)$. Furthermore, $\sum_m \int_{r_m}^{r_{m+1}} = \int_0^\infty$. With this, one obtains

$$\beta F_2^{\mathrm{ex}} = -\pi \rho N k_{\mathrm{B}} T \int_0^\infty [\beta w(r)]^2 \rho \chi_T^0 \, g_0(r) r^2 \mathrm{d}r.$$

Barker and Henderson now use[11] that $\rho\chi_T^0 = (\partial\rho/\partial p)_0$, where p is the pressure in the system, to gain the so called 'macroscopic' compressibility approximation:

$$\frac{\beta F_2^{\text{ex}}}{N} = -\pi\rho k_{\text{B}}T \int_0^\infty [\beta w(r)]^2 \left(\frac{\partial\rho}{\partial p}\right)_0 g_0(r) r^2 \mathrm{d}r.$$

We, however, use the relation between the compressibility and the radial distribution function[12],

$$\rho k_{\text{B}}T\chi_T^0 = 1 + \rho \int [g_0(r) - 1]\mathrm{d}\mathbf{r},$$

to get

$$\begin{aligned}\frac{\beta F_2^{\text{ex}}}{N} = -\pi\rho\Big[1 + 4\pi\rho \int_0^\infty [g_0(r') - 1] r'^2 \mathrm{d}r'\Big] \\ \times \int_0^\infty [\beta w(r)]^2 g_0(r) r^2 \mathrm{d}r. \qquad (6.18)\end{aligned}$$

With Eqs. (6.14) and (6.18), we have gained an approximate[13] expansion up to second order of the excess free energy of the system with the interaction potential in Eq. (6.1) with $\lambda = 1$. Moreover, we could express the second order expression of F^{ex} solely in terms of the radial distribution function $g_0(r)$ of the reference system, the perturbation potential $w(r)$, and the bulk density ρ. Since $w(r)$ is specified by the system of interest and ρ is a parameter we control, only $g_0(r)$ must be calculated to obtain the approximate F^{ex}.

Now, we can continue to determine the bulk line of coexistence (binodal), the so-called spinodal, the line which seperates metastable from unstable states in the phase diagram, and the critical

[11] See e.g. text body below Eq. (2.4.21) in Ref. [17]
[12] See e.g. Eq. (2.6.12) in Ref. [17].
[13] Since the second order term in Eq. (6.18) is approximate.

point of the system of interest. For this, we first calculate the bulk chemical potential μ and the pressure p via the free energy density $f = F/V = (F^{\mathrm{id}} + F^{\mathrm{ex}})/V = f^{\mathrm{id}} + f^{\mathrm{ex}}$:[14]

$$\mu = \frac{\partial f}{\partial \rho} = \frac{\partial f^{\mathrm{id}}}{\partial \rho} + \frac{\partial f^{\mathrm{ex}}}{\partial \rho} = \mu^{\mathrm{id}} + \mu^{\mathrm{ex}} \tag{6.19}$$

$$p = -f + \rho\mu, \tag{6.20}$$

where $f^{\mathrm{id}} = k_{\mathrm{B}}T\rho\big(\ln[\Lambda^3\rho] - 1\big)$. To calculate the binodal, we demand chemical and mechanical equilibrium for two phases, labeled I and II, with different densities or packing fractions $\eta_{\mathrm{I}} = \frac{\pi}{6}\rho_{\mathrm{I}}\sigma^3$ and $\eta_{\mathrm{II}} = \frac{\pi}{6}\rho_{\mathrm{II}}\sigma^3$ at fixed temperature T:

$$\begin{aligned} \mu(\eta_{\mathrm{I}}, T) &= \mu(\eta_{\mathrm{II}}, T) \\ p(\eta_{\mathrm{I}}, T) &= p(\eta_{\mathrm{II}}, T). \end{aligned} \tag{6.21}$$

[14] It is

$$\mu = \frac{\partial F(N,T,V)}{\partial N},$$

and, if we plug in a factor of one in the form of V/V, we obtain

$$\mu = \frac{V}{V}\frac{\partial F(N,T,V)}{\partial N} = V\frac{\partial V^{-1}F(N,T,V)}{\partial N}.$$

Since F is a homogeneous function of degree one in the extensive variables,

$$V^{-1}F(N,T,V) = F(N/V,T,V/V) \equiv f(\rho,T)$$

holds, and thus

$$\mu = V\frac{\partial f(\rho,T)}{\partial N} = V\frac{\partial f(\rho,T)}{\partial \rho}\frac{\partial \rho}{\partial N} = \frac{\partial f(\rho,T)}{\partial \rho},$$

where we have used that $\partial\rho/\partial N = V^{-1}$. Furthermore, in bulk $\Omega = -pV = F - N\mu$, and, hence,

$$p = -\frac{F}{V} + \frac{N}{V}\mu = -f + \rho\mu.$$

The system of equations (6.21) is then solved for the two packing fractions η_{I} and η_{II}. In the T-η-diagram, the binodal is then given by all the sets $\{(\eta_{\mathrm{I}}(T), T), (\eta_{\mathrm{II}}(T), T)\}$ of phase points (η, T), where T is smaller than the critical temperature T_{crit}. The spinodal seperates meta-stable from unstable states in the phase diagram. Unstable states are characterized by a negative slope of the pressure as a function of the packing fraction η, for fixed $T < T_{\mathrm{crit}}$. Thus, for a given temperature $T < T_{\mathrm{crit}}$, the unstable regions lie between the maximum and the minimum of the pressure curve $p(\eta, T)$, and the two points on the spinodal lie at the position of the maximum and the minimum, respectively. By solving

$$\frac{\partial p(\eta, T)}{\partial \eta} = 0 \tag{6.22}$$

for T, the spinodal is obtained as a function $T(\eta)$. At the critical point $(\eta_{\mathrm{crit}}, T_{\mathrm{crit}})$ binodal and spinodal meet, and the pressure curve $p(\eta, T_{\mathrm{crit}})$ has a saddle point at $\eta = \eta_{\mathrm{crit}}$. Hence, the critical point is determined by solving the system of equations

$$\frac{\partial p(\eta, T)}{\partial \eta} = 0, \qquad \frac{\partial^2 p(\eta, T)}{\partial \eta^2} = 0 \tag{6.23}$$

for η and T.

In the following, the full expressions of the free energy density f, the chemical potential μ and the pressure p obtained via the (approximate) second order high temperature expansion of F^{ex} are shown, where we use the following abbreviations[15]:

$$I = \int_0^\infty g_0(r)\, \beta w(r)\, r^2 \mathrm{d}r, \tag{6.24}$$

[15] The integral I is the integral of the first order expression of F^{ex} in Eq. (6.14), and was derived in a canonical description. Hence, it originally contains the canonical radial distribution function. However, in the thermodynamic limit, canonical and grand canonical descriptions become equivalent.

$$J_1 = \int_0^\infty [g_0(r) - 1] r^2 \mathrm{d}r,$$

and

$$J_2 = \int_0^\infty g_0(r) [\beta w(r)]^2 \, r^2 \mathrm{d}r.$$

The expression for the free energy density thus reads

$$\beta f = \beta f^{\mathrm{id}} + \beta f_0^{\mathrm{ex}} + \beta f_1^{\mathrm{ex}} + \beta f_2^{\mathrm{ex}} + \mathcal{O}(\beta^3),$$

where

$$\begin{aligned} \beta f^{\mathrm{id}} &= \rho\big(\ln[\Lambda^3 \rho] - 1\big), \\ \beta f_1^{\mathrm{ex}} &= 2\pi\rho^2 I, \\ \beta f_2^{\mathrm{ex}} &= -\pi\rho^2 \Big[1 + 4\pi\rho J_1\Big] J_2. \end{aligned} \tag{6.25}$$

The chemical potential, hence, is given by

$$\beta\mu = \beta\mu^{\mathrm{id}} + \beta\mu_0^{\mathrm{ex}} + \beta\mu_1^{\mathrm{ex}} + \beta\mu_2^{\mathrm{ex}} + \mathcal{O}(\beta^3),$$

with

$$\begin{aligned} \beta\mu^{\mathrm{id}} &= \ln[\Lambda^3 \rho], \\ \beta\mu_1^{\mathrm{ex}} &= 4\pi\rho I + 2\pi\rho^2 \frac{\partial I}{\partial \rho}, \\ \beta\mu_2^{\mathrm{ex}} &= -2\pi\rho \Big[1 + 4\pi\rho J_1\Big] J_2 - 4\pi^2\rho^2 \left[J_1 + \rho \frac{\partial J_1}{\partial \rho} \right] J_2 \\ &\quad - \pi\rho^2 \Big[1 + 4\pi\rho J_1\Big] \frac{\partial J_2}{\partial \rho}, \end{aligned} \tag{6.26}$$

and the pressure consequently reads as

$$\beta p = \beta p^{\mathrm{id}} + \beta p_0^{\mathrm{ex}} + \beta p_1^{\mathrm{ex}} + \beta p_2^{\mathrm{ex}} + \mathcal{O}(\beta^3),$$

where

$$\begin{aligned}
\beta p^{\mathrm{id}} &= \rho, \\
\beta p_1^{\mathrm{ex}} &= 2\pi\rho^2 I + 2\pi\rho^3 \frac{\partial I}{\partial \rho}, \\
\beta p_2^{\mathrm{ex}} &= -\pi\rho^2\Big[1 + 4\pi\rho J_1\Big] J_2 - 4\pi^2\rho^3 \left[J_1 + \rho \frac{\partial J_1}{\partial \rho} \right] J_2 \\
&\quad - \pi\rho^3\Big[1 + 4\pi\rho J_1\Big] \frac{\partial J_2}{\partial \rho}.
\end{aligned} \tag{6.27}$$

Note that since $g_0(r)$ in general is dependent on the density ρ and the temperature T, also the integrals I, J_1, and J_2 are. In practice, the radial distribution function of the reference system is obtained numerically, and, hence, the calculation of the integrals and their derivatives is done numerically, too.

The form of the expressions βf_0^{ex}, $\beta\mu_0^{\mathrm{ex}}$, and βp_0^{ex}, obviously, depends on what reference system is chosen. In what follows, we apply the hard-sphere fluid as reference system, since its thermodynamic and structural properties are well known [17]. In particular we use the expressions originally derived by Carnahan and Starling [7] to describe the hard-sphere bulk properties. Thus, we have for the free energy density βf_0^{ex} and the chemical potential $\beta\mu_0^{\mathrm{ex}}$ of the hard-sphere reference system

$$\beta f_0^{\mathrm{ex}} = \beta f_{\mathrm{hs}}^{\mathrm{ex}} = \beta f_{\mathrm{cs}}^{\mathrm{ex}} = \rho \frac{4\eta - 3\eta^2}{(1-\eta)^2} \tag{6.28}$$

and

$$\beta\mu_0^{\mathrm{ex}} = \beta\mu_{\mathrm{hs}}^{\mathrm{ex}} = \beta\mu_{\mathrm{cs}}^{\mathrm{ex}} = \frac{8\eta - 9\eta^2 + 3\eta^3}{(1-\eta)^3}.$$

The Carnahan-Starling expression for the pressure is given by

$$\begin{aligned}\beta p_{\mathrm{cs}} &= \rho \frac{1+\eta+\eta^2-\eta^3}{(1-\eta)^3} \\ &= \beta p^{\mathrm{id}} + \beta p_{\mathrm{cs}}^{\mathrm{ex}} = \beta p^{\mathrm{id}} + \beta p_{\mathrm{hs}}^{\mathrm{ex}} = \beta p^{\mathrm{id}} + \beta p_0^{\mathrm{ex}}.\end{aligned}$$

6.1.2. The mean-field approximation

The first order and the approximate second order term of the λ-expansion of the excess free energy F^{ex} in Eqs. (6.14) and (6.18), respectively, require the knowledge of the radial distribution function $g_0(r)$ of the reference system. Obtaining the latter can be tedious, as it can be a function not only of the particle-particle distance r but also of the particles' bulk density ρ or packing fraction η (as is the case for hard spheres), and even of the temperature. In practice, this means that for every system density or even for every state point (η, T) under consideration, the radial distribution function of the reference system must be calculated. The idea of the so called mean-field approximation is to circumvent this effort by considering a first order λ-expansion for which the first order term [Eq. (6.14)] is simplified. The ansatz is to neglect the local structure of the reference fluid by setting $g_0(r) = 1$. With this, the first order term basically reduces to an integral over the perturbation potential $w(r)$:

$$\begin{aligned}\frac{\beta F_1^{\mathrm{ex}}}{N} = \frac{\beta F_{\mathrm{mf}}^{\mathrm{ex}}}{N} &= \frac{\beta\rho}{2} \int w(r) \mathrm{d}\mathbf{r} \\ &= 2\pi\rho \int_0^\infty \beta w(r)\, r^2 \mathrm{d}r. \end{aligned} \tag{6.29}$$

The approach might seem rough at first glance, but its simplicity is appealing, making it a commonly used approximation. Nevertheless, the simplicity comes at a price and the mean-field ansatz

describes the bulk phase equilibrium rather poorly in comparison to simulation results. Hence, often empirical corrections to the perturbation potential are required to optimize the outcome. This, for example, is the case for the square-well potential which in the mean-field approach is separated into hard-sphere potential and attractive well. The latter is then extended into the hard core to optimize the bulk phase behavior [1]. In the mean-field approximation the integral I in Eq. (6.24) becomes independent of the density ρ, and, hence, the derivatives of I in the first order expressions of excess chemical potential and pressure in Eqs. (6.26) and (6.27) vanish, which simplifies the calculations required to study the phase behavior. The mean-field contributions to the excess chemical potential and the pressure thus read:

$$\beta\mu_{\mathrm{mf}}^{\mathrm{ex}} = 4\pi\rho \int_0^\infty \beta w(r) r^2 \mathrm{d}r \tag{6.30}$$

and

$$\beta p_{\mathrm{mf}}^{\mathrm{ex}} = 2\pi\rho^2 \int_0^\infty \beta w(r) r^2 \mathrm{d}r \tag{6.31}$$

To study the Jagla fluid, the mean-field approximation is too rough as it does not capture the liquid-liquid phase transition. The binodal of the Jagla fluid's gas-liquid transition, calculated by means of the mean-field approximation, is shown in Fig. 6.12. Here, hard spheres are the reference system and the soft tail of the Jagla potential is the perturbation.

6.2. BH and WCA perturbation theory

6.2.1. Theory

The λ-expansion, described in Sec. 6.1, is useful only, if a well-understood reference system can be found for the system of

interest. For the reasons noted above, an apparent choice for a reference system is the hard-sphere fluid, which is exploited by the perturbation theories of Barker and Henderson (BH) [4] and Weeks, Chandler, and Andersen (WCA) [41]. In both approaches the interaction potential is separated in a repulsive reference part $v_0(r)$ and an attractive perturbation part $w(r)$; the former is then mapped onto a hard-sphere potential with an effective hard-sphere diameter d, providing an effective reference system comprised of hard spheres. The only difference between the two approaches is the way, in which the interaction potential is split.

In their original work, [4] BH separate the potential at the zero crossing into a positive reference part and a negative perturbation. This is illustrated in Fig. 6.1 for the Jagla potential. The reference potential $v_0(r)$ is then mapped onto the effective hard-sphere diameter d via [4, 17]

$$d = \int_0^\infty (1 - \exp[-\beta v_0(r)])\mathrm{d}r. \tag{6.32}$$

The WCA method has the advantage over the BH method that for some systems, where a second order term of the λ-expansion would be needed by the BH theory to obtain accurate results, a first order WCA λ-term is sufficient [17]. In the WCA approach the potential is split at its minimum in a purely repulsive (reference) and a purely attractive (perturbation) part. This has the benefit that the potential's rapidly varying bit between the zero crossing and the minimum is not treated in the perturbation of the λ-theory, resulting in a perturbation potential that is more slowly varying in space. This in turn makes the perturbation series converge more rapidly [17]. To avoid discontinuities, the repulsive part of the potential is shifted upwards by the amount of the depth of the potential well, and the perturbation part is extended as a constant function into the hard core. This is depicted in Fig. 6.2.

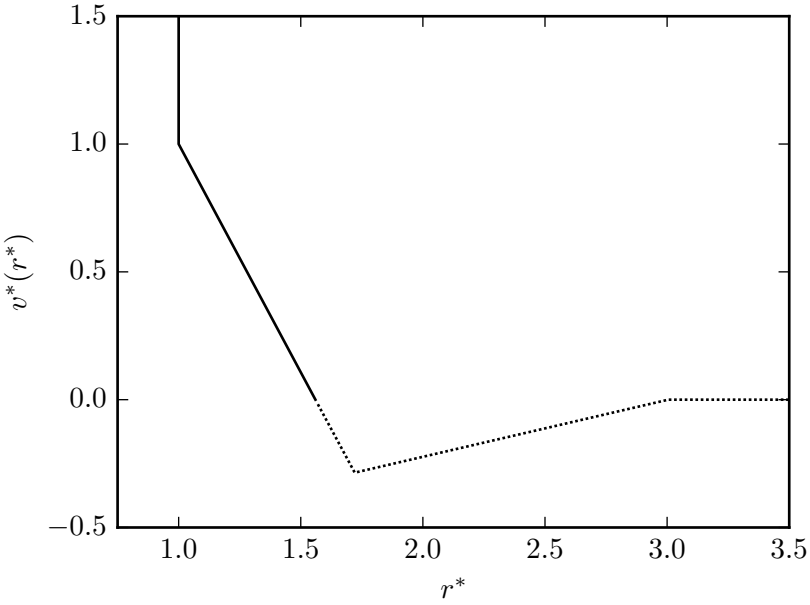

Figure 6.1.: The reduced Jagla potential $v_{\mathrm{J}}^* = v_{\mathrm{J}}/\epsilon$ split according to the BH method as a function of the reduced center-to-center particle distance $r^* = r/\sigma$. The solid line shows the reduced interaction potential of the reference system, $v_0^* = v_0/\epsilon$, whereas the dotted line depicts the reduced perturbation potential $w^* = w/\epsilon$. Note that except for the hard-sphere contribution, the potentials are zero in the regions where no lines are shown.

As in the BH theory, the reference potential is then mapped onto the corresponding hard-sphere diameter d via Eq. (6.32).

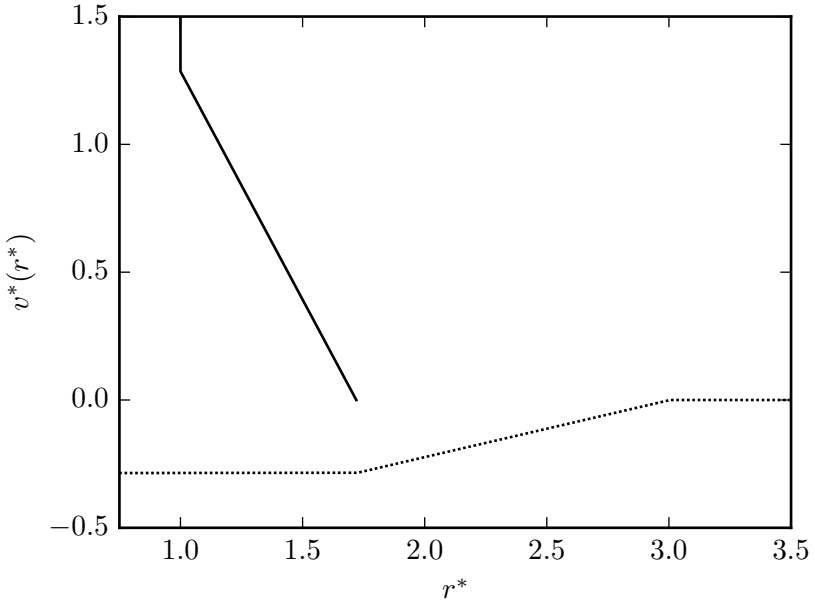

Figure 6.2.: The reduced Jagla potential $v_{\mathrm{J}}^* = v_{\mathrm{J}}/\epsilon$ split according to the WCA method as a function of the reduced center-to-center particle distance $r^* = r/\sigma$. The solid line shows the reduced interaction potential of the reference system, $v_0^* = v_0/\epsilon$, whereas the dotted line depicts the reduced perturbation potential $w^* = w/\epsilon$. Note that except for the hard-sphere contribution, the potentials are zero in the regions where no lines are shown.

6.2.2. Results

In our attempt to describe the Jagla fluid's bulk phase behavior by means of the WCA and BH pertrubation theories, we try out both approaches. Some characteristic pressure curves obtained at various temperatures using the WCA and BH theory up until the first order, are shown in Figs. 6.3 and 6.4, respectively. Here, $g_0(r)$ in Eq. (6.14) is given by the radial distribution function $g_{\mathrm{hs}}(r;\eta)$ of hard spheres which we obtain by means of a DFT calculation, where the White Bear II version of FMT (see Sec. 4.2) is applied. Except for $T^* = 50$, the temperatures are chosen such, that a comparison with the MC simulation data by Lomba et al. [24], who show a liquid-liquid critical point in the respective temperature region in their phase diagram of the Jagla fluid, is possible. Note that Lomba and colleagues apply a reduced Jagla potential $v_{\mathrm{J}}^* = v_{\mathrm{J}}/\epsilon$ which is stretched by a factor of 7/2 in direction of the ordinate, compared to the one we use here. This requires to multiply the reduced temperatures $T^* = k_{\mathrm{B}}T/\epsilon$ of their results by the inverse of the factor, i.e., by 2/7, in order to gain comparability with our results. In both figures the pressure line at $T^* = 50$ is in excellent agreement with the hard-sphere equation of state, shown by the circles in the plots, which demonstrates that the high-temperature limit of our calculations is correct. The pressure curves for the three low temperatures show van der Waals loops, which vanish with increasing temperature, indicating a gas-liquid critical point. We find the corresponding first order binodals, depicted in Fig. 6.5, to be in good agreement with the MC data by Lomba and co-workers, considering the usual deviation occurring between perturbation theory and, quasi-exact, MC results. However, neither the WCA, nor the BH approach show van der Waals loops for a liquid-liquid critical point in our pressure data for greater packing fractions. Instead, the

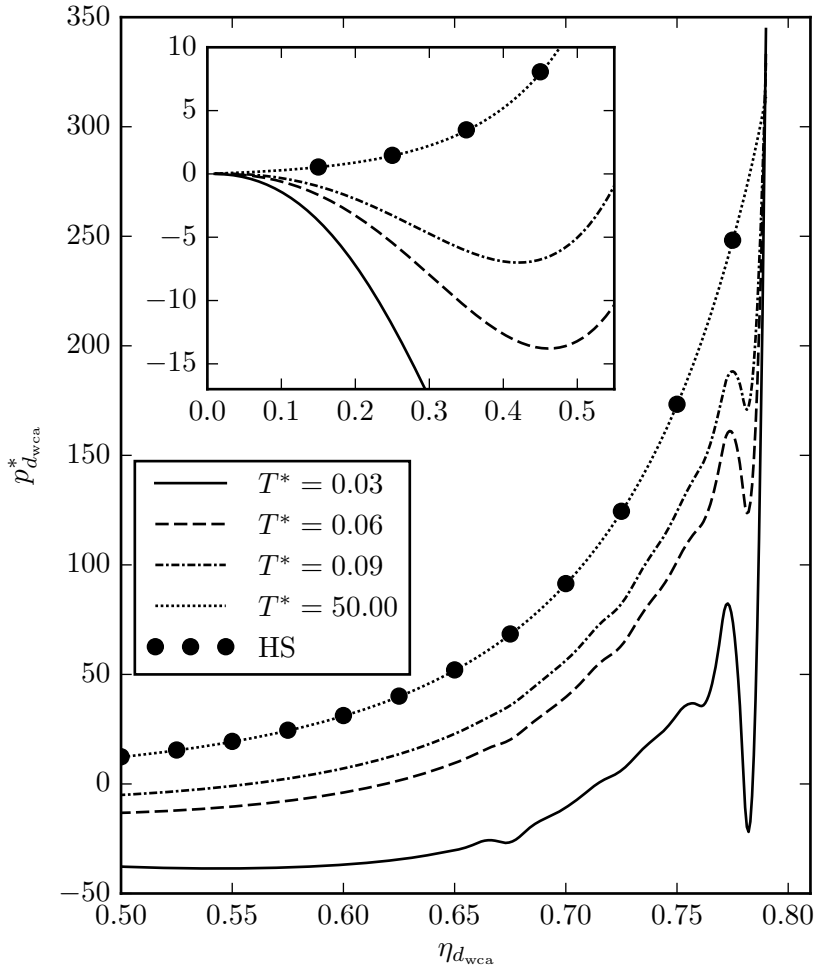

Figure 6.3.: The reduced pressure $p^*_{d_{\mathrm{wca}}} = \beta p d^3_{\mathrm{wca}}$ of the Jagla fluid as a function of the effective packing fraction $\eta_{d_{\mathrm{wca}}} = \pi\rho d^3_{\mathrm{wca}}/6$, for various reduced temperatures $T^* = k_{\mathrm{B}}T/\epsilon$, when described by means of the first order WCA perturbation theory (lines). The hard-sphere equation of state is plotted as filled circles. For reasons of clarity, the main plot focuses on high values of $\eta_{d_{\mathrm{wca}}}$, while the inset shows data for $\eta_{d_{\mathrm{wca}}} < 0.5$.

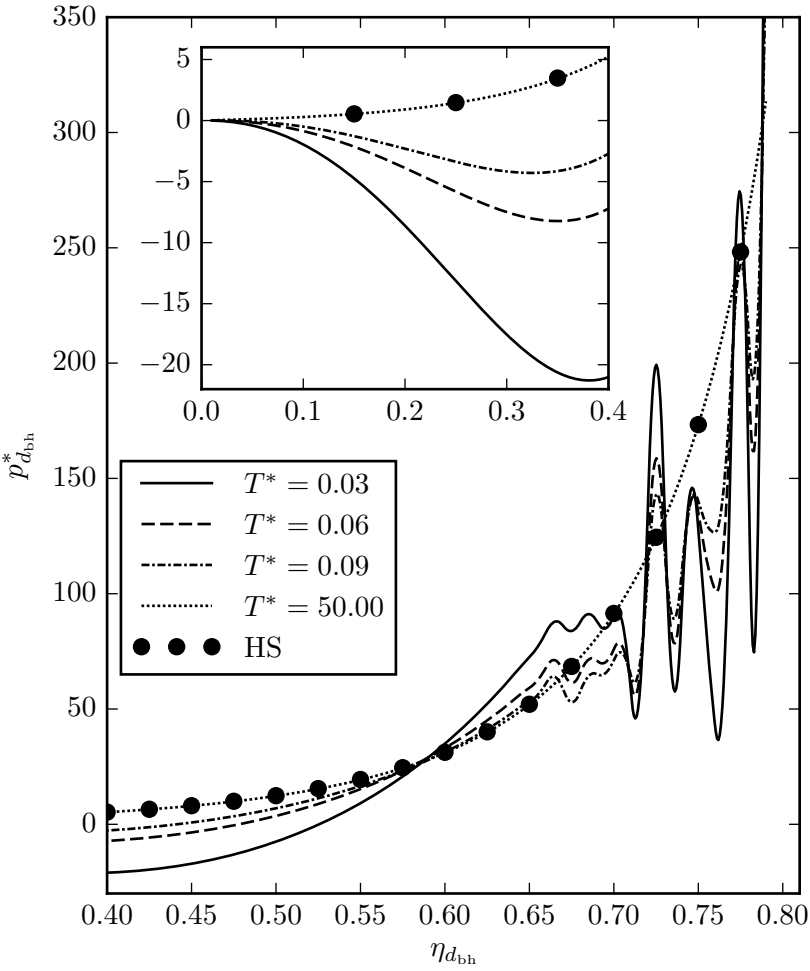

Figure 6.4.: The reduced pressure $p^*_{d_{\mathrm{bh}}} = \beta p d^3_{\mathrm{bh}}$ of the Jagla fluid as a function of the effective packing fraction $\eta_{d_{\mathrm{bh}}} = \pi\rho d^3_{\mathrm{bh}}/6$, for various reduced temperatures $T^* = k_{\mathrm{B}}T/\epsilon$, when described by means of the first order BH perturbation theory (lines). The hard-sphere equation of state is plotted as filled circles. For reasons of clarity, the main plot focuses on high values of $\eta_{d_{\mathrm{bh}}}$, while the inset shows data for $\eta_{d_{\mathrm{bh}}} < 0.4$.

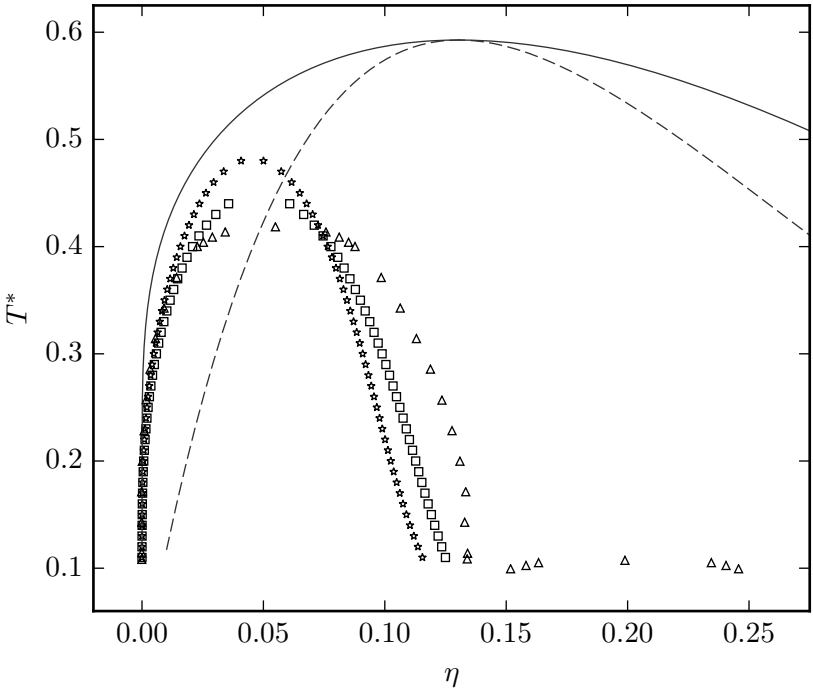

Figure 6.5.: The bulk binodals of the Jagla fluid in the T^*-η phase diagram obtained by means of the first order WCA (stars) and BH (squares) perturbation theories, standard mean-field theory (solid line) and MC simulations [24] (triangles). The dashed line shows the mean-field bulk spinodal of the Jagla fluid.

pressure curves begin to oscillate wildly, where the oscillations are stronger in the BH results. These oscillations have their origin in the calculation of the first order perturbation term βF_1^{ex} of the excess free energy [Eq. (6.14)] in which the hard-sphere radial distribution function $g_{\text{hs}}(r, \eta)$ enters. For the calculation of the latter the non-freezing White Bear II [18] functional is used, which enables us to calculate the pressure at such high packing fractions in the first place. But not only is a hard-sphere radial distribution function at packing fractions beyond the hard-sphere freezing transition ($\eta_{\text{f}} \approx 0.492$) highly questionable, also the DFT results in this density range exhibit inaccuracies which cause oscillations in the derivative $\partial g_{\text{hs}}(r; \eta)/\partial\eta$ of the hard-sphere radial distribution function, which enters the expression for the pressure $p(\eta)$ [Eq. (6.27)], and, hence, cause the oscillation observed in the plot.

This raises the question why $\eta_{d_{\text{bh}}}$ and $\eta_{d_{\text{wca}}}$ become so large after all. In Sec. 6.2.1 the mapping of the reference potential $v_0(r)$ onto the effective hard-sphere diameter d is described, thus creating an effective hard-sphere reference system. The latter has the effective packing fraction η_d which is related to the packing fraction η via

$$\eta_d = \frac{\pi}{6}\rho d^3 = \frac{\pi}{6}\rho\sigma^3\frac{d^3}{\sigma^3} = \eta\left(\frac{d}{\sigma}\right)^3. \tag{6.33}$$

All calculations are then carried out in the effective system and are later transformed back to the "real" density scale using (6.33). This scaling is the crux of the matter in case of the Jagla potential. Since the corresponding reference potentials $v_0(r)$ in the BH and WCA perturbation theories are rather long ranged, compared to the hard-sphere diameter σ (see Figs. 6.1 and 6.2), the cube $(d/\sigma)^3$ of the diameter ratio is well greater than one for low temperatures. This is illustrated in Fig. 6.6. The liquid-liquid critical point in the

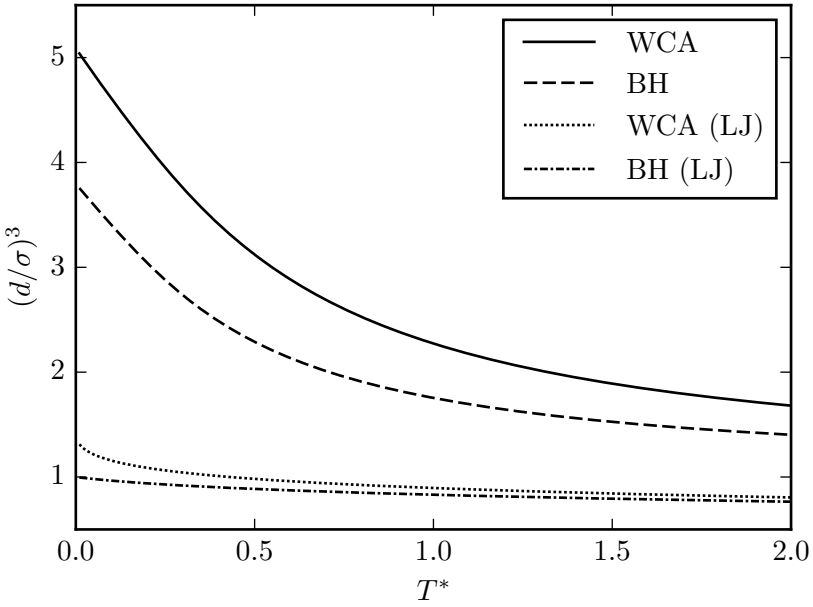

Figure 6.6.: The cube $(d/\sigma)^3$ of the hard-sphere diameter ratio as a function of the reduced temperature $T^* = k_\mathrm{B}T/\epsilon$ for the Jagla potential in the WCA description (solid line) and in the BH description (dashed line), as well as for the scaled Lennard-Jones potential (see Fig. 1.1) in the WCA description (dotted line) and in the BH description (dash-dotted line).

work by Lomba et al. [24], if scaled to match the Jagla potential used in our work, is located at $(\eta, T^*) \approx (0.2, 0.1)$. At $T^* = 0.1$, the cube of the diameter ratio in the WCA case is $(d_{\mathrm{wca}}/\sigma)^3 \approx 4.6$, implying that in the effective system the liquid-liquid critical point would be located at $\eta_{d_{\mathrm{wca}}} = 0.92$. Not only is this packing fraction located in the density region where our pressure curves oscillate, but it is way beyond the freezing packing fraction of hard spheres, $\eta_{\mathrm{f}} \approx 0.492$, and even beyond close-packing which occurs at $\eta_{\mathrm{cp}} = \frac{\pi}{3\sqrt{2}} \approx 0.7405$. To properly calculate the liquid-liquid binodal, the pressure at even lower temperatures and greater packing fractions must be known, rendering the WCA perturbation theory useless for describing the Jagla fluid. In the BH case the scaling is not quite as dramatic, $(d_{\mathrm{bh}}/\sigma)^3 \approx 3.4$ at $T^* = 0.1$, resulting in a effective packing fraction $\eta_{d_{\mathrm{bh}}} = 0.68$ for the liquid-liquid critical point. However, our BH pressure curves show more dramatic oscillations than the WCA curves for $\eta_{d_{\mathrm{bh}}} \gtrsim 0.65$, making it again impossible to observe liquid-liquid van der Waals loops.

Within the scope of this work we also calculate the second order perturbation terms for the BH and WCA perturbation theories. However, we do not show the corresponding results in a plot, as no new information is gained. Due to the occurrence of more complicated integrals in the second order terms (see Eq. (6.18)), we observe more dramatic oscillations than in the first order case and no liquid-liquid van der Waals loops. This is to be expected, since the scaling factor between the "real" and the effective system is independent of the order of the perturbation; also the improper DFT input data for high packing fractions is the same.

If we consider Figs. 1.1 and 6.6 once more, it becomes clear that in terms of the scaling between the "real" and the effective system, the BH and WCA theories also work well in the high density region for short ranged particle-particle interaction potentials,

such as the Lennard-Jones potential. Here, in the WCA case the cube $(d/\sigma)^3$ of the diameter ratio is smaller than 1.5, and in the BH case even smaller than 1.0 for all temperatures above zero.

6.3. Pure hard sphere reference system

6.3.1. Theory

As shown in Sec. 6.2.2, the mapping of the reference system $v_0(r)$ onto an effective hard-sphere diameter according to the method of BH [4] (see Sec. 6.2.1) renders the BH and WCA perturbation theories [4, 41] unemployable to describe the Jagla fluid's liquid-liquid critical point, due to the dramatic density scaling between the effective and the "real" system. Hence, it seems reasonable to apply the perturbation theory discussed in Sec. 6.1 without the introduction of an effective hard-sphere system. One of the simplest implementations of such a system, certainly, is to choose hard spheres with diameter σ to be the reference system, and to consider the Jagla potential for $r > \sigma$ as perturbation. This splitting into reference and perturbation potential is depicted in Fig. 6.7.

6.3.2. Results

For the first order perturbation ansatz of this basic splitting into reference and perturbation potential, we obtain the pressure curves depicted in Fig. 6.8. As expected, we observe gas-liquid van der Waals loops in the η-region below $\eta \approx 0.35$, which vanish at higher temperatures, indicating a gas-liquid critical point. Furthermore, the pressure curves show a second van der Waals loop for packing fractions above 0.35 which also vanishes at greater temperatures. This is remarkable, given how simple the applied

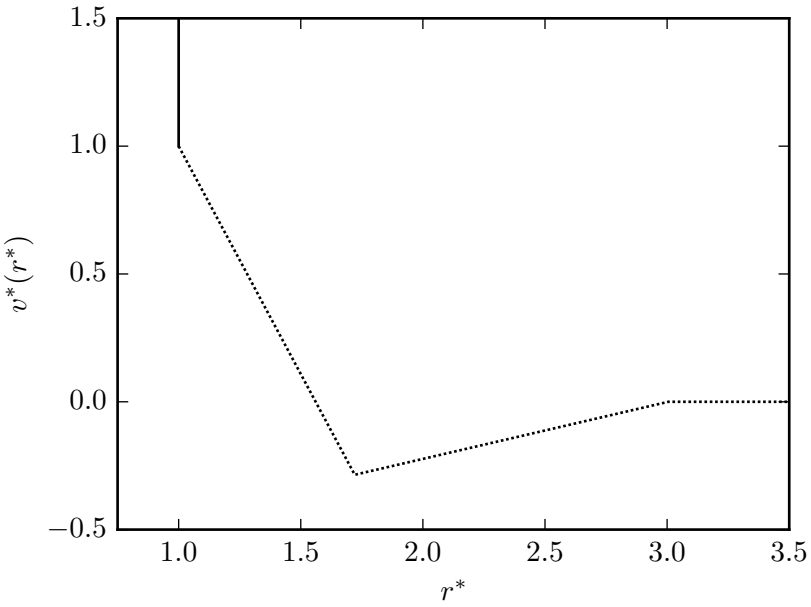

Figure 6.7.: The reduced Jagla potential $v_{\mathrm{J}}^* = v_{\mathrm{J}}/\epsilon$ split into reference and perturbation potential at $r{=}\sigma$ as a function of the reduced center-to-center particle distance $r^* = r/\sigma$. The solid line shows the reduced interaction potential of hard spheres with diameter σ which constitute the reference system with reduced interaction potential $v_0^* = v_0/\epsilon = v_{\mathrm{hs}}/\epsilon$. The dotted line depicts the reduced perturbation potential $w^* = w/\epsilon$ which, in this case, is the full Jagla potential outside the hard core. Note that the perturbation potential is zero in the regions where no lines are shown.

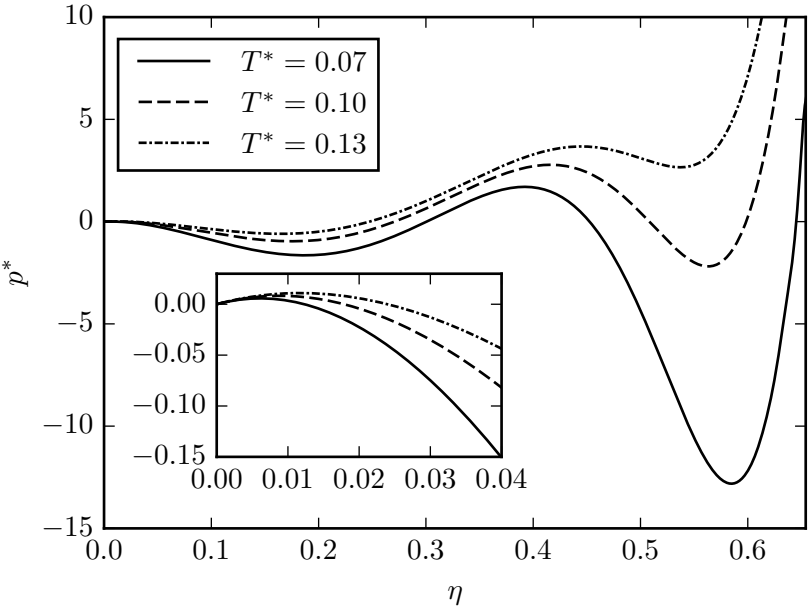

Figure 6.8.: The reduced pressure $p^* = \beta p \sigma^3$ of the Jagla fluid as a function of the packing fraction $\eta = \pi \rho \sigma^3/6$ for various reduced temperatures $T^* = k_\mathrm{B} T/\epsilon$ when described by means of the first order perturbation theory with the potential splitting depicted in Fig. 6.7. The inset shows the pressure data for small η in greater detail.

ansatz is, and a clear indication of a second critical point. However, half of each second van der Waals loop lies above the freezing packing fraction $\eta_\mathrm{f} \approx 0.492$ of hard spheres and we are only able to obtain this result, since we apply the non-freezing White Bear II version of FMT to calculate the hard-sphere radial distribution function $g_\mathrm{hs}(r)$. Recall, that the latter enters the first order term of the excess free energy [Eq. (6.14)]. For completeness we note that, again, we observe unphysical oscillations in the pressure curves for $\eta \gtrsim 0.65$ (not depicted in the plot) due to the reasons discussed in Sec. 6.2.2. In the corresponding phase diagram in Fig. 6.9, we indeed observe a second binodal the high-density branch of which lies, as expected from the pressure curves, in the region above the hard-sphere freezing transition. This renders the applied potential separation a poor model for a liquid-liquid phase transition. Furthermore, we find no agreement with the second MC binodal [24] and only poor agreement with the first binodal. Since this simple splitting of the Jagla potential into reference and perturbation potential already yields a second binodal in a first order treatment, and since the first order perturbation term is easier to implement than the second order one, especially with regard to the inhomogeneous system, we do not investigate a second order treatment here. Instead, we continue to apply a more elaborate reference system.

6.4. Two reference systems

6.4.1. Theory

Motivated by the fact that our simple first order perturbation treatment of the Jagla fluid in Sec. 6.3 yields a second binodal, we now try to find a way to split the Jagla potential into reference and perturbation potential such that, in a first order treatment,

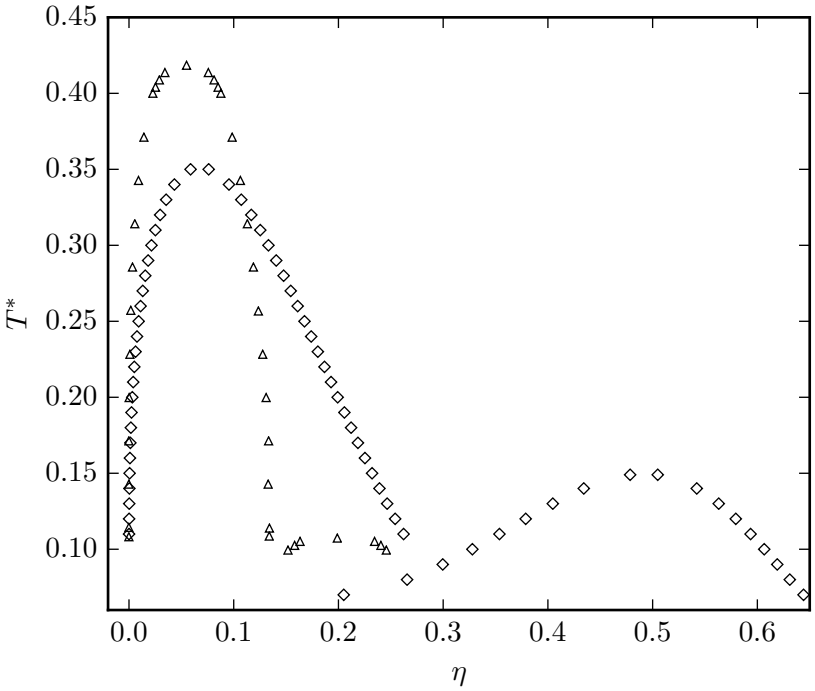

Figure 6.9.: The bulk binodals of the Jagla fluid in the T^*-η phase diagram. The diamonds show the results of a first order perturbation ansatz with the potential splitting depicted in Fig. 6.7. The triangles show the results of MC simulations [24].

the second binodal lies fully in the liquid-density region of the hard-sphere fluid. For this, we, again, separate the Jagla potential according to the method of BH, depicted in Fig. 6.1, into a purely repulsive reference system $v_0(r)$ and an attractive perturbation $w(r)$ comprised of the potential's well. This results in a first order λ-expansion [Eq. (6.9)] of the form

$$\beta F^{\mathrm{ex}} = \beta F_0^{\mathrm{ex}} + \beta F_1^{\mathrm{ex}} + \mathcal{O}(\beta^2). \tag{6.34}$$

Now, of course, we face the problem that, unlike assumed before, the excess free energy term F_0^{ex} of the repulsive reference system is unknown. To overcome this issue, we apply another potential separation, and divide the potential $v_0(r)$ of the repulsive reference system into a hard-sphere potential $v_{\mathrm{hs}}(r)$ (representing the reference system of the repulsive reference system) and a repulsive ramp $v_{\mathrm{rep}}(r)$ (the perturbation of the hard-sphere reference system), which lets us expand F_0^{ex} in a further first-order λ-expansion to be

$$\beta F_0^{\mathrm{ex}} = \beta F_{\mathrm{hs}}^{\mathrm{ex}} + \beta F_{1,\mathrm{rep}}^{\mathrm{ex}} + \mathcal{O}(\beta^2). \tag{6.35}$$

This twofold split of the Jagla potential is depicted in Fig. 6.10. Also, note that the hard spheres of the hard-sphere reference system have a diameter σ and no effective diameter d. Now, we plug Eq. (6.35) in Eq. (6.34), and obtain a first order expression of the Jagla fluid's excess free energy:

$$\beta F^{\mathrm{ex}} = \beta F_{\mathrm{hs}}^{\mathrm{ex}} + \beta F_{1,\mathrm{rep}}^{\mathrm{ex}} + \beta F_1^{\mathrm{ex}} + \mathcal{O}(\beta^2). \tag{6.36}$$

The hard-sphere term is known [see Eq. (6.28)], and the two first order terms are according to Eq. (6.14):

$$\frac{\beta F_{1,\mathrm{rep}}^{\mathrm{ex}}}{N} = \frac{\beta\rho}{2} \int g_{\mathrm{hs}}(r) v_{\mathrm{rep}}(r) \mathrm{d}\mathbf{r} \tag{6.37}$$

$$\frac{\beta F_1^{\mathrm{ex}}}{N} = \frac{\beta\rho}{2} \int g_0(r) w(r) \mathrm{d}\mathbf{r}, \tag{6.38}$$

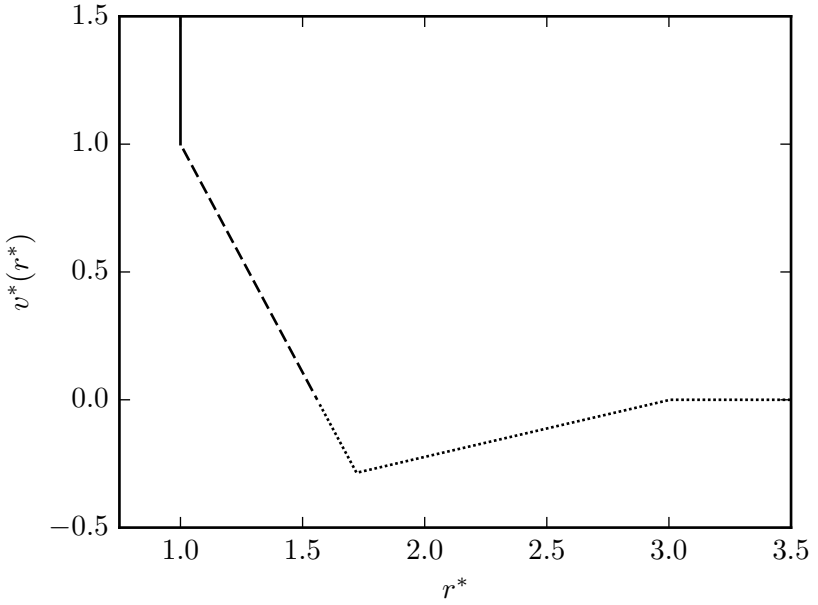

Figure 6.10.: The twice split reduced Jagla potential $v_{\mathrm{J}}^* = v_{\mathrm{J}}/\epsilon$ as a function of the reduced center-to-center particle distance $r^* = r/\sigma$. The first separation divides the potential according to BH into a purely positive reference part $v_0^* = v_0/\epsilon$ (solid and dashed lines) and a negative perturbation well $w^* = w/\epsilon$ (dotted line). The reference potential v_0^* is again divided into a hard-sphere potential $v_{\mathrm{hs}}^* = v_{\mathrm{hs}}/\epsilon$ (solid line) and a repulsive ramp $v_{\mathrm{rep}}^* = v_{\mathrm{rep}}/\epsilon$ (dashed line). Note that except for the hard-sphere contribution, the potentials are zero in the regions where no lines are shown.

where $g_{\mathrm{hs}}(r)$ is the hard-sphere radial distribution function, and $g_0(r)$ is the radial distribution function of the original repulsive reference system with interaction potential $v_0(r)$.

6.4.2. Results

To obtain an explicit expression for the excess free energy F^{ex} of the Jagla fluid via Eqs. (6.36), (6.37), and (6.38), we compute the hard-sphere radial distribution functions $g_{\mathrm{hs}}(r;\eta)$ and the radial distribution functions $g_0(r;\eta,T^*)$ of the repulsive reference system. In particular, we deploy DFT calculations and use the White Bear II version of FMT (see Sec. 4.2) to calculate $g_{\mathrm{hs}}(r;\eta)$, whereas $g_0(r;\eta,T^*)$ is computed by use of (MC) simulations[16].

Three characteristic pressure curves, derived by means of the first order F^{ex} in Eq. (6.36), are shown in Fig. 6.11. As expected, the curves show gas-liquid van der Waals loops in the η-region between 0.0 and 0.125, which vanish for increasing temperatures, indicating a gas-liquid critical point. Additionally, for greater packing fractions, i. e. $0.125 < \eta < 0.3$, each pressure line shows a second van der Waals loop which is fully in the liquid regime of hard spheres and which becomes weaker for higher temperatures. These indicate the existence of a liquid-liquid critical point. The corresponding phase diagram is shown in Fig. 6.12. We find the gas-liquid binodal in the η-region between 0 and 0.125 to be in good agreement with the respective MC data by Lomba et al. [24], considering the usual deviation occurring between perturbation theory results and, quasi-exact, MC data. Additionally, we observe a liquid-liquid binodal for packing fractions between 0.125 and 0.325, peaking in a liquid-liquid critical point, the critical

[16] We, also, tried to compute $g_0(r;\eta,T^*)$ trough mean-field DFT calculations, however, the results exhibit unphysical oscillations at low temperatures, and, hence, can not be deployed here.

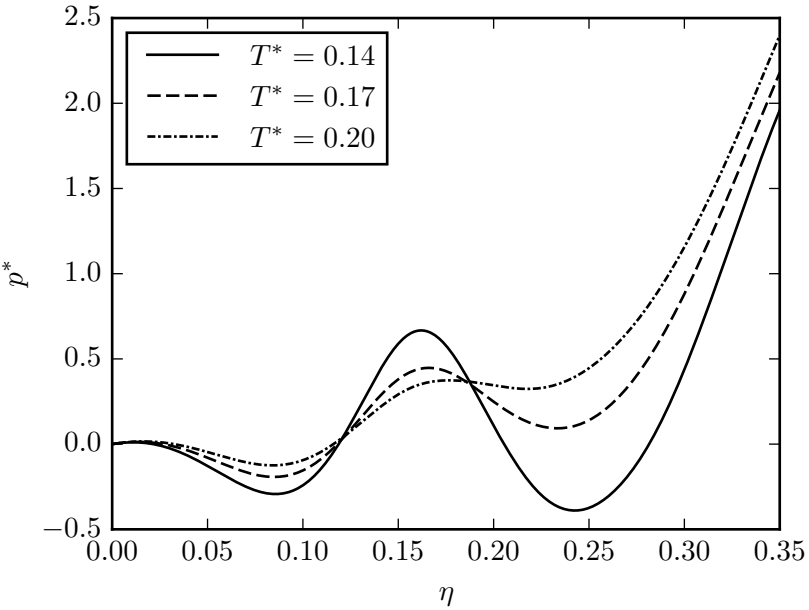

Figure 6.11.: The reduced pressure $p^* = \beta p \sigma^3$ of the Jagla fluid as a function of the packing fraction $\eta = \pi \rho \sigma^3/6$ for various temperatures $T^* = k_\mathrm{B} T/\epsilon$ when calculated by means of the first order twice split potential approach described in Sec. 6.4.1.

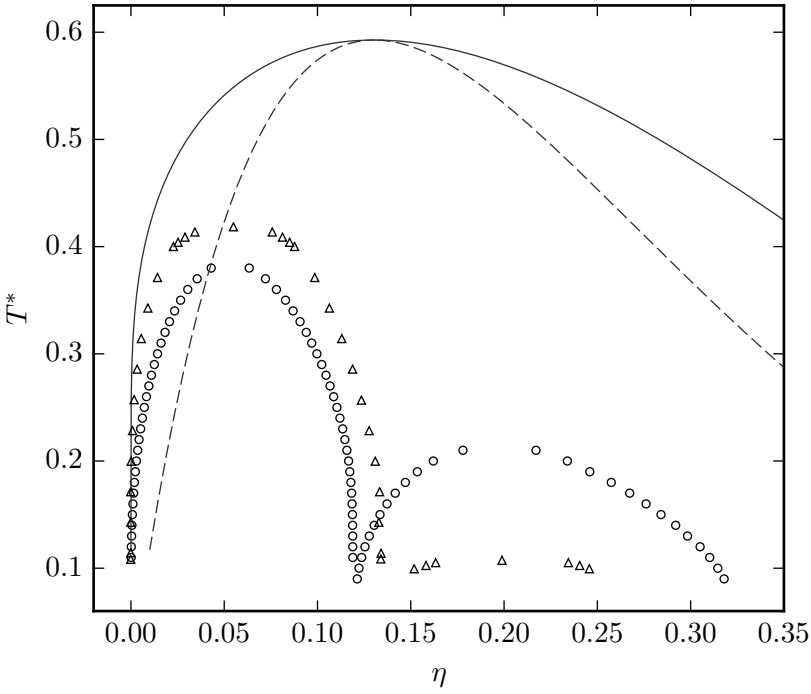

Figure 6.12.: The bulk binodals of the Jagla fluid in the T^*-η phase diagram obtained by means of the first order twice split potential approach (circles), described in Sec. 6.4.1, standard mean-field theory (solid line) and MC simulations [24] (triangles). The dashed line shows the mean-field bulk spinodal of the Jagla fluid.

packing fraction of which is in good agreement with the MC result by Lomba and colleagues.

In Fig. 6.12 we also show the binodal and spinodal line of the Jagla fluid when described by means of the standard mean-field approximation (Sec. 6.1.2). The improvement of the first order twice split potential approach over the mean-field ansatz is remarkable. The latter already fails to predict the gas-liquid binodal correctly and does not capture the liquid-liquid line of coexistence. From this comparison it becomes clear that a proper perturbation ansatz is required to study the Jagla fluid's liquid-liquid critical point.

7. Perturbation DFT[1]

7.1. Theory

7.1.1. Derivation of a perturbation DFT

Having derived a bulk perturbation theory for the Jagla fluid capable of describing a liquid-liquid phase separation in the previous sections, the next step is to extend the theory to inhomogeneous systems. This would not only enable us to study e.g. the local structure of the fluid close to walls or other physical boundaries, the first step to investigate phenomena such as wetting and dewetting and capillarity, but also would offer possibilities to alter the Jagla fluid's phase diagram to our needs. Hence, we continue to consider an inhomogeneous Jagla fluid, which we describe using classical density functional theory (DFT) [11] (see Chpt. 4). As already mentioned above, in general, the exact expression of the excess intrinsic free energy functional $\mathcal{F}^{\text{ex}}[\rho(\mathbf{r})]$ is unknown. Hence, and to ensure that the excess functional has the correct bulk limit, namely F^{ex} in Eq. (6.36), we derive an approximate expression for $\mathcal{F}^{\text{ex}}[\rho(\mathbf{r})]$ as follows. Initially, we derive an exact expression for $\mathcal{F}^{\text{ex}}$ which is the sum of the intrinsic excess free energy $\mathcal{F}_0^{\text{ex}}$ of a reference system and a perturbation term $\mathcal{F}_w^{\text{ex}}$,

[1] At the date of printing, content of this chapter is accepted as a Regular Article in Physical Review E with the title "Towards a density functional theory for the Jagla fluid" by Florian Gußmann, S. Dietrich and Roland Roth.

where we follow closely Ref. [17]. Based on this, we apply the approximation originally proposed by Sokolowski and Fischer [37] to obtain an expression of $\mathcal{F}_w^{\mathrm{ex}}$ which is practically applicable.

Again, we assume a pairwise particle-particle interaction potential $v(\mathbf{r}_1, \mathbf{r}_2)$, and, consequently, the interatomic potential energy V_N is

$$V_N(\mathbf{r}^N) = \sum_{i=1}^{N} \sum_{j>i}^{N} v(\mathbf{r}_i, \mathbf{r}_j).$$

With this, the grand partition function Ξ can be written as[2]

$$\Xi = \sum_{N=0}^{\infty} \frac{1}{N!} \int \cdots \int \prod_{i,j>i}^{N} \exp[-\beta v(\mathbf{r}_i, \mathbf{r}_j)] \prod_{k=1}^{N} z^*(\mathbf{r}_k) \mathrm{d}\mathbf{r}_1 \ldots \mathrm{d}\mathbf{r}_N, \tag{7.1}$$

[2] The grand partition function of an inhomogeneous fluid is given by [17]

$$\Xi = \sum_{N=0}^{\infty} \frac{1}{N!} \int \exp(-\beta V_N) \left(\prod_{k=1}^{N} z \exp[-\beta \phi(\mathbf{r}_k)] \right) \mathrm{d}\mathbf{r}^N,$$

and can be easily derived from Eq. (3.1), if the potential energy $\sum_{k=1}^{N} \phi(\mathbf{r}_k)$, caused by the external potential acting upon the particles, is added to the hamiltonian in Eq. (2.3), and if the particle momenta are integrated out. Here, $z = \exp(\beta\mu)/\Lambda^3$ is the activity. If we now define the local activity $z^*(\mathbf{r}) = z \exp[-\beta\phi(\mathbf{r})]$, the expression for Ξ can be rewritten to be

$$\Xi = \sum_{N=0}^{\infty} \frac{1}{N!} \int \exp(-\beta V_N) \prod_{k=1}^{N} z^*(\mathbf{r}_k) \mathrm{d}\mathbf{r}^N.$$

Finally, we use that V_N is a sum of pair potentials to rewrite the term $\exp(-\beta V_N)$:

$$\Xi = \sum_{N=0}^{\infty} \frac{1}{N!} \int \cdots \int \prod_{i,j>i}^{N} \exp[-\beta v(\mathbf{r}_i, \mathbf{r}_j)] \prod_{k=1}^{N} z^*(\mathbf{r}_k) \mathrm{d}\mathbf{r}_1 \ldots \mathrm{d}\mathbf{r}_N.$$

where $z^*(\mathbf{r}) = z\exp[-\beta\phi(\mathbf{r})]$ is the local activity, $z = \exp(\beta\mu)/\Lambda^3$ is the activity, $\prod_{i,j>i}^{N} = \prod_{i=1}^{N}\prod_{j>i}^{N}$, and $\phi(\mathbf{r})$ is the external potential acting on a particle at position $\mathbf{r}$. Now, the functional derivative of the functional of the grand potential $\Omega[\rho(\mathbf{r})]$ with respect to the interaction potential $v(r)$ is (see App. C.1):

$$\frac{\delta\Omega}{\delta v(\mathbf{r}_1,\mathbf{r}_2)} = \frac{1}{\Xi}\sum_{N=2}^{\infty}\frac{N(N-1)}{2N!} \times \int\cdots\int\prod_{i,j>i}^{N}\exp[-\beta v(\mathbf{r}_i,\mathbf{r}_j)]\prod_{k=1}^{N}z^*(\mathbf{r}_k)\mathrm{d}\mathbf{r}_3\ldots\mathrm{d}\mathbf{r}_N. \tag{7.2}$$

If we compare this result with the expression for the n-particle density $\rho^{(n)}$ in Eq. (3.5)[3], we see that

$$\rho^{(2)}(\mathbf{r}_1,\mathbf{r}_2) = 2\frac{\delta\Omega}{\delta v(\mathbf{r}_1,\mathbf{r}_2)}.$$

Since the only term in $\Omega[\rho(\mathbf{r})]$ which is dependent on $v(\mathbf{r}_1,\mathbf{r}_2)$ is $\mathcal{F}^{\mathrm{ex}}[\rho(\mathbf{r})]$, it also holds that

$$\rho^{(2)}(\mathbf{r}_1,\mathbf{r}_2) = 2\frac{\delta\mathcal{F}^{\mathrm{ex}}[\rho(\mathbf{r})]}{\delta v(\mathbf{r}_1,\mathbf{r}_2)}. \tag{7.3}$$

We now further assume the particle-particle interaction potential to be of the form

$$v_\lambda(\mathbf{r}_1,\mathbf{r}_2) = v_0(\mathbf{r}_1,\mathbf{r}_2) + \lambda w(\mathbf{r}_1,\mathbf{r}_2), \tag{7.4}$$

where $\lambda \in [\lambda_1,\lambda_2] = [0,1]$ (cf. Eq. (6.1) and text thereafter). As in Sec. 6.1.1, be $v_0(\mathbf{r}_1,\mathbf{r}_2)$ the interaction potential of a well-known

[3] Due to the addition of the external potential term to the hamiltonian discussed in Fn. 2, in the inhomogeneous case the quantity z^N in Eq. (3.5) must be replaced by $\prod_{k=1}^{N} z^*(\mathbf{r}_k)$ and be written under the integral.

reference system and $w(\mathbf{r}_1, \mathbf{r}_2)$ a perturbation added to v_0. The coupling parameter λ gradually turns on the perturbation when increased from 0 to 1. By integration of Eq. (7.3), with $v(\mathbf{r}_1, \mathbf{r}_2) = v_\lambda(\mathbf{r}_1, \mathbf{r}_2)$, which is explicitly carried out in App. C.2, the intrinsic excess free energy functional $\mathcal{F}^{\mathrm{ex}}[\rho(\mathbf{r})]$ of the system characterized by the particle-particle interaction potential $v_{(\lambda=1)}(\mathbf{r}_1, \mathbf{r}_2)$ can be expressed as [17]

$$\mathcal{F}^{\mathrm{ex}}[\rho(\mathbf{r})] = \mathcal{F}_0^{\mathrm{ex}}[\rho(\mathbf{r})] + \mathcal{F}_w^{\mathrm{ex}}[\rho(\mathbf{r})], \tag{7.5}$$

where

$$\begin{aligned}\mathcal{F}_w^{\mathrm{ex}}[\rho(\mathbf{r})] = \frac{1}{2}\int_0^1 \mathrm{d}\lambda \int \mathrm{d}\mathbf{r}_1 \rho(\mathbf{r}_1) \\ \times \int \mathrm{d}\mathbf{r}_2 \rho(\mathbf{r}_2) g^{(2)}(\mathbf{r}_1, \mathbf{r}_2; \lambda) w(\mathbf{r}_1, \mathbf{r}_2),\end{aligned} \tag{7.6}$$

and $\mathcal{F}_0^{\mathrm{ex}}[\rho(\mathbf{r})]$ is the intrinsic free energy of the reference system, i. e. the system with interaction potential $v_{(\lambda=0)}(\mathbf{r}_1, \mathbf{r}_2)$. Furthermore, $g^{(2)}(\mathbf{r}_1, \mathbf{r}_2; \lambda)$ denotes the 2-particle distribution function of the inhomogeneous system with particle-particle interaction potential $v_\lambda(\mathbf{r}_1, \mathbf{r}_2)$. Since merely little is known about the 2-particle distribution function of an inhomogeneous system, approximations for Eq. (7.6) are required. The so called mean-field approximation to the problem (see also Sec. 7.1.2), commonly used in DFT calculations, is to set $g^{(2)}(\mathbf{r}_1, \mathbf{r}_2; \lambda) = 1$, thereby neglecting the local structure around a particle in the fluid. However, this approach is too simple for our investigation, since setting the 2-particle distribution function equal to unity, would give us an incorrect bulk-limit of $\mathcal{F}_w^{\mathrm{ex}}$, when compared to the bulk expressions derived earlier [Eqs. (6.37) and (6.38)]. Instead, we exploit the fact that when we separate the Jagla potential as in the bulk investigations above into reference part

and perturbation, the reference system is always fully repulsive, and, hence, follow the route of Sokolowski and Fischer [37], also described in Ref. [40], who approximate $\mathcal{F}_w^{\mathrm{ex}}$ via

$$\mathcal{F}_w^{\mathrm{ex}}[\rho(\mathbf{r})] = \frac{1}{2}\int \mathrm{d}\mathbf{r}_1 \rho(\mathbf{r}_1) \int \mathrm{d}\mathbf{r}_2 \rho(\mathbf{r}_2) g_0^{(2)}(\mathbf{r}_1, \mathbf{r}_2) w(\mathbf{r}_1, \mathbf{r}_2), \quad (7.7)$$

where $g_0^{(2)}(\mathbf{r}_1, \mathbf{r}_2)$ is the 2-particle distribution function of the inhomogeneous repulsive reference system. Since $g_0^{(2)}(\mathbf{r}_1, \mathbf{r}_2)$ is a complicated function and no detailed knowledge of its behavior in realistic non-uniform systems is available, Sokolowski and Fischer continue to approximate $g_0^{(2)}(\mathbf{r}_1, \mathbf{r}_2)$ by the corresponding bulk radial distribution function evaluated at some mean density $\bar{\rho}$:

$$g_0^{(2)}(\mathbf{r}_1, \mathbf{r}_2) \approx g_0^{\mathrm{b}}(r_{12}; \bar{\rho}). \quad (7.8)$$

They further note that $\bar{\rho}$ has to be chosen such that the resulting radial distribution function is firstly symmetric with respect to the interchange of particles, and secondly approaches the corresponding bulk radial distribution function as $\bar{\rho}$ tends to the bulk density ρ_{b}.

With the aim to preserve the expression of the bulk excess free energy [Eq. (6.36)], we continue to construct a perturbation functional for the twice split Jagla potential based on Eqs. (7.5) and (7.6) using the approximations in Eqs. (7.7) and (7.8) which is of the following form:

$$\begin{aligned} \mathcal{F}^{\mathrm{ex}}[\rho(\mathbf{r})] &= \mathcal{F}_0^{\mathrm{ex}}[\rho(\mathbf{r})] + \mathcal{F}_w^{\mathrm{ex}}[\rho(\mathbf{r})] \\ &= \mathcal{F}_{\mathrm{hs}}^{\mathrm{ex}}[\rho(\mathbf{r})] + \mathcal{F}_{\mathrm{rep}}^{\mathrm{ex}}[\rho(\mathbf{r})] + \mathcal{F}_w^{\mathrm{ex}}[\rho(\mathbf{r})], \end{aligned} \quad (7.9)$$

where

$$\mathcal{F}_{\mathrm{rep}}^{\mathrm{ex}}[\rho(\mathbf{r})] = \frac{1}{2}\int \mathrm{d}\mathbf{r}_1 \rho(\mathbf{r}_1) \int \mathrm{d}\mathbf{r}_2 \rho(\mathbf{r}_2) g_{\mathrm{hs}}^{\mathrm{b}}(r_{12}; \bar{\rho}) v_{\mathrm{rep}}(r_{12}),$$

and

$$\mathcal{F}_w^{\mathrm{ex}}[\rho(\mathbf{r})] = \frac{1}{2}\int \mathrm{d}\mathbf{r}_1\rho(\mathbf{r}_1)\int \mathrm{d}\mathbf{r}_2\rho(\mathbf{r}_2)g_0^{\mathrm{b}}(r_{12};\bar{\rho})w(r_{12}).$$

Taken together, we obtain

$$\begin{aligned}\mathcal{F}^{\mathrm{ex}}[\rho(\mathbf{r})] &= \mathcal{F}_{\mathrm{hs}}^{\mathrm{ex}}[\rho(\mathbf{r})] + \frac{1}{2}\iint \mathrm{d}\mathbf{r}_1\mathrm{d}\mathbf{r}_2\rho(\mathbf{r}_1)\rho(\mathbf{r}_2) \\ &\qquad \times \left[g_{\mathrm{hs}}^{\mathrm{b}}(r_{12};\bar{\rho})v_{\mathrm{rep}}(r_{12}) + g_0^{\mathrm{b}}(r_{12};\bar{\rho})w(r_{12})\right] \\ &\equiv \mathcal{F}_{\mathrm{hs}}^{\mathrm{ex}}[\rho(\mathbf{r})] + \mathcal{F}_{\mathrm{J}}^{\mathrm{ex}}[\rho(\mathbf{r})]. \end{aligned} \tag{7.10}$$

The hard-sphere bulk radial distribution function $g_{\mathrm{hs}}^{\mathrm{b}}(r_{12};\bar{\rho})$ and the bulk radial distribution function of the original reference system with interaction potential $v_0(r)$, $g_0^{\mathrm{b}}(r_{12};\bar{\rho})$, are the same as in Sec. 6.4.1, only, here, they are evaluated at the mean density $\bar{\rho}$. The potentials $v_0(r)$, $v_{\mathrm{rep}}(r)$ and $w(r)$ are also the same as in Sec. 6.4.1 and are depicted in Fig. 6.10. The quantity $\mathcal{F}_{\mathrm{hs}}^{\mathrm{ex}}[\rho(\mathbf{r})]$ is the hard-sphere intrinsic free energy functional for which we apply the White Bear version [31] of FMT [30, 32] (see Sec. 4.2). Note that $\mathcal{F}_{\mathrm{J}}^{\mathrm{ex}}[\rho(\mathbf{r})]$ in (7.10) has the correct bulk limit, namely $F_{1,\mathrm{rep}}^{\mathrm{ex}} + F_1^{\mathrm{ex}}$ in Eqs. (6.36), (6.37) and (6.38), if the bulk limit of $\bar{\rho}$ is the bulk density ρ_{b}. The proof is done analogously to the one in Sec.7.1.2 for the mean-field term.

The question remains which mean density $\bar{\rho}$ to apply, especially with regard to the calculation of the functional derivative of $\delta\mathcal{F}_{\mathrm{J}}^{\mathrm{ex}}[\rho(\mathbf{r})]/\delta\rho(\mathbf{r})$, needed to minimize the functional of the grand potential. If the mean density is dependent on the density distribution $\rho(\mathbf{r})$, this must be considered in the functional derivative, making its calculation more sophisticated and the result lengthy. Hence, the easiest route to continue from here is to set $\bar{\rho}$ to be the bulk density ρ_{b}. With this, the functional derivative of $\mathcal{F}_{\mathrm{J}}^{\mathrm{ex}}[\rho(\mathbf{r})]$

in Eq. (7.10) is given by

$$\frac{\delta \mathcal{F}_{\mathrm{J}}^{\mathrm{ex}}}{\delta \rho(\mathbf{r}_2)} = \int \rho(\mathbf{r}_1) \Big[g_{\mathrm{hs}}^{\mathrm{b}}(r_{12}; \rho_{\mathrm{b}}) v_{\mathrm{rep}}(r_{12}) + g_0^{\mathrm{b}}(r_{12}; \rho_{\mathrm{b}}) w(r_{12}) \Big] \mathrm{d}\mathbf{r}_1. \tag{7.11}$$

A more sophisticated version for the mean-density is the one introduced by Sokolowski and Fischer [37], namely

$$\bar{\rho}(\mathbf{r}_1, \mathbf{r}_2) = \frac{1}{2} \big[\rho_\nu(\mathbf{r}_1) + \rho_\nu(\mathbf{r}_2) \big].$$

Here,

$$\rho_\nu(\mathbf{r}) = \int \mathrm{d}\mathbf{r}' \rho(\mathbf{r}') \omega_\nu(|\mathbf{r} - \mathbf{r}'|)$$

is a coarse grained, or weighted, density with the weight function

$$\omega_\nu(r) = \frac{3}{4\pi r_\nu^3} \Theta(r_\nu - r),$$

and the Heaviside step function $\Theta(r)$. The coarse grained density $\rho_\nu(\mathbf{r})$ is the average density in a sphere of radius r_ν at position $\mathbf{r}$, making $\bar{\rho}(\mathbf{r}_1, \mathbf{r}_2)$ the mean of the two average densities in the spheres at $\mathbf{r}_1$ and $\mathbf{r}_2$. With $\bar{\rho}$ now also being a functional of $\rho(\mathbf{r})$, care is needed when evaluating the functional derivative

$\delta\mathcal{F}_{\mathrm{J}}^{\mathrm{ex}}/\delta\rho(\mathbf{r})$. The latter is given by

$$\begin{aligned}
\frac{\delta\mathcal{F}_{\mathrm{J}}^{\mathrm{ex}}}{\delta\rho(\mathbf{r}_0)} &= \frac{1}{2}\int \mathrm{d}\mathbf{r}_1 \int \mathrm{d}\mathbf{r}_2 \frac{\delta\big(\rho(\mathbf{r}_1)\rho(\mathbf{r}_2)\big)}{\delta\rho(\mathbf{r}_0)} \\
&\qquad \times \Big[g_{\mathrm{hs}}^{\mathrm{b}}(r_{12};\bar{\rho})v_{\mathrm{rep}}(r_{12}) + g_0^{\mathrm{b}}(r_{12};\bar{\rho})w(r_{12})\Big] \\
&\quad + \frac{1}{2}\int \mathrm{d}\mathbf{r}_1 \int \mathrm{d}\mathbf{r}_2 \rho(\mathbf{r}_1)\rho(\mathbf{r}_2) \\
&\qquad \times \left[\left.\frac{\partial g_{\mathrm{hs}}^{\mathrm{b}}(r_{12};\rho)}{\partial\rho}\right|_{\rho=\bar{\rho}} v_{\mathrm{rep}}(r_{12}) \right. \\
&\qquad\quad \left. + \left.\frac{\partial g_0^{\mathrm{b}}(r_{12};\rho,T^*)}{\partial\rho}\right|_{\rho=\bar{\rho}} w(r_{12}) \right] \frac{\delta\bar{\rho}}{\delta\rho(\mathbf{r}_0)} \\
&= \int \mathrm{d}\mathbf{r}_2 \rho(\mathbf{r}_2)\Big[g_{\mathrm{hs}}^{\mathrm{b}}(r_{02};\bar{\rho})v_{\mathrm{rep}}(r_{02}) + g_0^{\mathrm{b}}(r_{02};\bar{\rho})w(r_{02})\Big] \\
&\quad + \frac{3}{8\pi r_\nu^3}\int \mathrm{d}\mathbf{r}_2 \rho(\mathbf{r}_2)\Theta(r_\nu - r_{02}) \int \mathrm{d}\mathbf{r}_1 \rho(\mathbf{r}_1) \\
&\qquad \times \left[\left.\frac{\partial g_{\mathrm{hs}}^{\mathrm{b}}(r_{12};\rho)}{\partial\rho}\right|_{\rho=\bar{\rho}} v_{\mathrm{rep}}(r_{12}) \right. \\
&\qquad\quad \left. + \left.\frac{\partial g_0^{\mathrm{b}}(r_{12};\rho,T^*)}{\partial\rho}\right|_{\rho=\bar{\rho}} w(r_{12}) \right],
\end{aligned} \tag{7.12}$$

where $r_{02} = |\mathbf{r}_2 - \mathbf{r}_0|$. Evaluating the expression in Eq. (7.12) requires in every step of the iteration to minimize $\Omega[\rho(\mathbf{r})]$ the calculation of $\bar{\rho}(\mathbf{r}_1, \mathbf{r}_2)$ at all points $(\mathbf{r}_1, \mathbf{r}_2)$ at which at least one of the two quantities $\rho_\nu(\mathbf{r}_1)$ and $\rho_\nu(\mathbf{r}_2)$ is unequal to zero. Furthermore, $g_{\mathrm{hs}}^{\mathrm{b}}(r;\rho)$ and $g_0^{\mathrm{b}}(r_{12};\rho,T^*)$ must be known on a (r,ρ)-grid, to calculate the derivatives in the second term of Eq. (7.12). This makes the calculation of the functional derivative of $\mathcal{F}_{\mathrm{J}}^{\mathrm{ex}}[\rho(\mathbf{r})]$ extremely tedious, if not almost impossible regarding computation time, and, hence, we simplify the expression in

Eq. (7.12) further and set the weighted density to be the bulk density: $\bar{\rho}(\mathbf{r}_1, \mathbf{r}_2) = \rho_\mathrm{b}$.

7.1.2. The mean-field approximation in the inhomogeneous case

In case of an inhomogeneous fluid, the idea of the mean-field approximation is the same as in bulk (see Sec. 6.1.2), namely to set $g(\mathbf{r}_1, \mathbf{r}_2; \lambda)$ in Eq. (7.6) to be 1, thereby fully neglecting the structure of the fluid in the vicinity of a particle. With $g(\mathbf{r}_1, \mathbf{r}_2; \lambda) = 1$, the integration with respect to λ in Eq. (7.6) becomes trivial and gives a factor of 1, and the expression for $\mathcal{F}_w^\mathrm{ex}[\rho(\mathbf{r})]$ reduces to

$$\mathcal{F}_\mathrm{mf}^\mathrm{ex}[\rho(\mathbf{r})] = \frac{1}{2} \iint \rho(\mathbf{r}_1)\rho(\mathbf{r}_2) w(\mathbf{r}_1, \mathbf{r}_2) \mathrm{d}\mathbf{r}_1 \mathrm{d}\mathbf{r}_2. \tag{7.13}$$

Under the assumption of identical particles, $w(\mathbf{r}_1, \mathbf{r}_2) = w(\mathbf{r}_2, \mathbf{r}_1)$ holds, and then the functional derivative $\delta\mathcal{F}_\mathrm{mf}^\mathrm{ex}/\delta\rho(\mathbf{r})$ of the mean-field term is

$$\frac{\delta\mathcal{F}_\mathrm{mf}^\mathrm{ex}}{\delta\rho(\mathbf{r}_2)} = \int \rho(\mathbf{r}_1) w(\mathbf{r}_1, \mathbf{r}_2) \mathrm{d}\mathbf{r}_1. \tag{7.14}$$

As is the case for its bulk version, the mean-field approximation is appealing due to its simplicity. To evaluate the functional derivative (7.14), only the perturbation potential $w(\mathbf{r}_1, \mathbf{r}_2)$ is required, and no additional input is necessary for the minimization process of DFT.

If the interaction potential is a function of only the particle-particle distance $|\mathbf{r}_2 - \mathbf{r}_1| = r_{12}$, the bulk limit of Eq. (7.13) is[4]

$$\frac{1}{N}\lim_{\rho(\mathbf{r})\to\rho_\mathrm{b}}\mathcal{F}^\mathrm{ex}_\mathrm{mf}[\rho(\mathbf{r})] = \frac{1}{N}\frac{\rho_\mathrm{b}^2}{2}V\int w(r)\mathrm{d}\mathbf{r} = \frac{\rho_\mathrm{b}}{2}\int w(r)\mathrm{d}\mathbf{r}$$

which is exactly the expression in Eq. (6.29).

7.2. Results

In order to test the quality of the perturbation DFT for the Jagla fluid derived in Sec. 7.1.1, we perform perturbation DFT calculations and MC simulations in a slit geometry. We compare the resulting perturbation DFT density profiles with our MC simulation data as well as with density curves obtained through mean-field DFT (see Sec. 7.1.2). The slit geometry is composed of two infinitely expanded, parallel and planar hard walls with reduced distance $l = L/\sigma$. In the following, we present the results calculated in a slit with reduced length $l = 22$ for various assorted state points (η, T^*). Here, l is chosen such that a bulk limit in the slit center can be observed to check for consistency. Also note that

[4] In bulk $\rho(\mathbf{r}) = \rho_\mathrm{b}$ and, with $w(\mathbf{r}_1, \mathbf{r}_2) = w(|\mathbf{r}_2 - \mathbf{r}_1|)$ we have

$$\lim_{\rho(\mathbf{r})\to\rho_\mathrm{b}}\mathcal{F}^\mathrm{ex}_\mathrm{mf}[\rho(\mathbf{r})] = \frac{\rho_\mathrm{b}^2}{2}\iint w(|\mathbf{r}_2 - \mathbf{r}_1|)\mathrm{d}\mathbf{r}_1\mathrm{d}\mathbf{r}_2.$$

Now, we substitute $(\mathbf{r}_2 - \mathbf{r}_1) \to \mathbf{r}$ in the integration with respect to $\mathbf{r}_2$, i.e. $\mathrm{d}\mathbf{r} = \mathrm{d}\mathbf{r}_2$, and find

$$\lim_{\rho(\mathbf{r})\to\rho_\mathrm{b}}\mathcal{F}^\mathrm{ex}_\mathrm{mf}[\rho(\mathbf{r})] = \frac{\rho_\mathrm{b}^2}{2}\int \mathrm{d}\mathbf{r}_1\int w(r)\mathrm{d}\mathbf{r}.$$

The integration with respect to $\mathbf{r}_1$ gives the volume V, and with this

$$\lim_{\rho(\mathbf{r})\to\rho_\mathrm{b}}\mathcal{F}^\mathrm{ex}_\mathrm{mf}[\rho(\mathbf{r})] = \frac{\rho_\mathrm{b}^2}{2}V\int w(r)\mathrm{d}\mathbf{r}.$$

not the full density profiles (which are symmetric) are presented, but only the densities in the vicinity of the left wall in order to show all relevant details. For the bulk radial distribution functions $g_{\mathrm{hs}}^{\mathrm{b}}(r;\rho_{\mathrm{b}})$ and $g_0^{\mathrm{b}}(r;\rho_{\mathrm{b}},T^*)$, needed to calculate the functional derivative in Eq. (7.12), we apply the same data as for the bulk calculations. Here, $g_{\mathrm{hs}}^{\mathrm{b}}(r;\rho_{\mathrm{b}})$ is obtained via DFT calculations, where the mark II [18] version of the White Bear functional is used (see Sec. 4.2), and $g_0^{\mathrm{b}}(r_{12};\rho_{\mathrm{b}},T^*)$ via MC simulations.

To begin with, we examine the performance of perturbation DFT regarding the choice of the mean density $\bar{\rho}(\mathbf{r}_1,\mathbf{r}_2)$. For this, we compare the density profiles of the DFTs with $\bar{\rho}(\mathbf{r}_1,\mathbf{r}_2) = \frac{1}{2}\big[\rho_\nu(\mathbf{r}_1)+\rho_\nu(\mathbf{r}_2)\big]$ [Eq. (7.12)], where[5] $r_\nu = 0.5\,\sigma$, and $\bar{\rho}(\mathbf{r}_1,\mathbf{r}_2) = \rho_{\mathrm{b}}$ [see Eq. (7.11)] to MC profiles in a system at state point $(\eta,T^*) = (0.1,1.0)$. This is depicted in Fig. 7.1. While the DFT with $\bar{\rho} = \rho_{\mathrm{b}}$ performs better than mean-field DFT, the corresponding density profile lies notably below the MC result. By contrast, the DFT with $\bar{\rho} = \frac{1}{2}\big[\rho_\nu(\mathbf{r}_1) + \rho_\nu(\mathbf{r}_2)\big]$ almost perfectly hits the MC contact value and provides results which are in very good agreement with the simulation data for $0.5 < z^* < 1.25$ and $z^* > 5.0$. Only for $1.25 < z^* < 5.0$, the DFT result is slightly below the MC data but still in good agreement. These results clearly show an improvement of DFT gained by the perturbation ansatz, where the DFT with $\bar{\rho} = \frac{1}{2}\big[\rho_\nu(\mathbf{r}_1) + \rho_\nu(\mathbf{r}_2)\big]$ clearly outperforms the one with $\bar{\rho} = \rho_{\mathrm{b}}$. Since the latter already lacks precision at this relative high temperature, we continue to apply the DFT with $\bar{\rho} = \frac{1}{2}\big[\rho_\nu(\mathbf{r}_1) + \rho_\nu(\mathbf{r}_2)\big]$, exclusively. We have to keep in mind that the critical point of the Jagla fluid's gas-liquid bulk binodal lies a little below $T^* = 0.4$ and the liquid-liquid

[5] We tried various values for the parameter r_ν, none of which seemed to produce results overall superior to the others, and chose the value for which the agreement of the contact value with the MC contact value was the best.

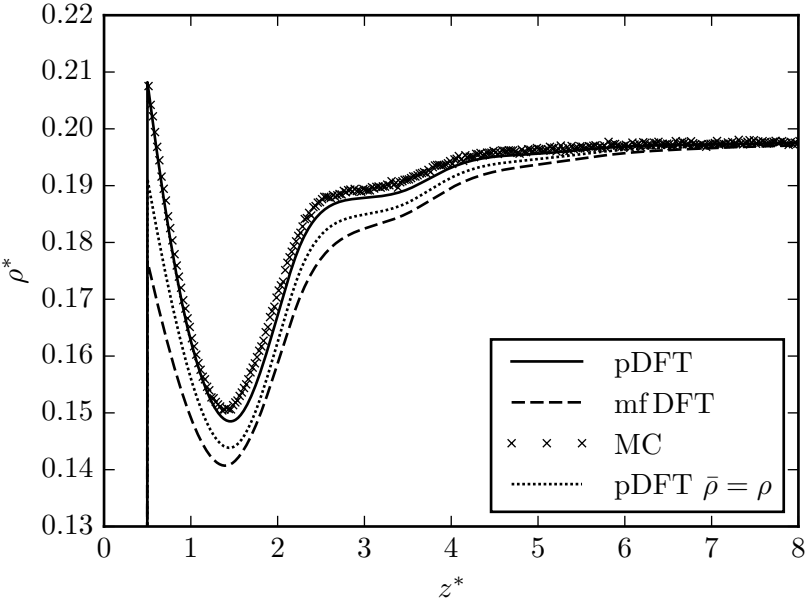

Figure 7.1.: The density distribution $\rho^* = \rho\sigma^3$ of the Jagla fluid in a slit with hard walls and reduced length $l = L/\sigma = 22$ at $(\eta, T^*) = (0.1, 1.0)$ described by means of the perturbation DFT with $\bar{\rho} = \frac{1}{2}\big[\rho_\nu(\mathbf{r}_1) + \rho_\nu(\mathbf{r}_2)\big]$ (solid line), the perturbation DFT with $\bar{\rho} = \rho_\mathrm{b}$ (dotted line), standard mean-field DFT (dashed-line) and MC simulations (crosses). The abscissa provides the reduced distance $z^* = z/\sigma$ from the left wall.

bulk binodal at temperatures around $T^* = 0.1$ (see Fig. 6.12). Thus, we need a DFT which performs reliably at temperatures way below $T^* = 1.0$, and, hence, discard the DFT with $\bar{\rho} = \rho_\mathrm{b}$. Therefore, from now on, by perturbation DFT, we mean the perturbation DFT with $\bar{\rho} = \frac{1}{2}\big[\rho_\nu(\mathbf{r}_1) + \rho_\nu(\mathbf{r}_2)\big]$. From Fig. 7.1, it also becomes clear that at the state point $(\eta, T^*) = (0.1, 1.0)$ mean-field DFT already fails to give the correct density curve and predicts, apart from the bulk limit in the slit center, values which are clearly below the (quasi-exact) MC result.

For an increased density, i.e. $(\eta, T^*) = (0.3, 1.0)$ (see Fig. 7.2), perturbation DFT gives still good results close to the wall but predicts a contact value which is a little below the MC data. Furthermore, perturbation DFT fails to predict the correct positions of the first minimum and maximum of the density profile away from contact, which are shifted somewhat to the right. Also, the depth of the first minimum is underestimated. However, perturbation DFT still produces significantly better results than mean-field DFT which gives a contact value that is almost a factor of $\frac{1}{2}$ off the MC data. Compared to the previous case, the overall performance of mean-field DFT seems to have improved, nevertheless.

For lower temperatures ($T^* = 0.5$) perturbation DFT clearly underestimates the density in the slit close to the wall at small density ($\eta = 0.1$), whereas mean-field DFT fails and predicts a profile close to or in a gas phase (see Fig. 7.3). The failure of mean-field DFT, however, comes at no surprise as for the state point under consideration the mean-field Jagla fluid is unstable (see phase diagram in Fig. 6.12). At greater densities ($\eta = 0.3$), however, the perturbation DFT results are in the range of the MC profile, where the contact value is too low, and, again, the positions of the maxima and minima is predicted incorrectly. Mean-field DFT, at least, gives the correct bulk limit (Fig. 7.4). Thus, it seems

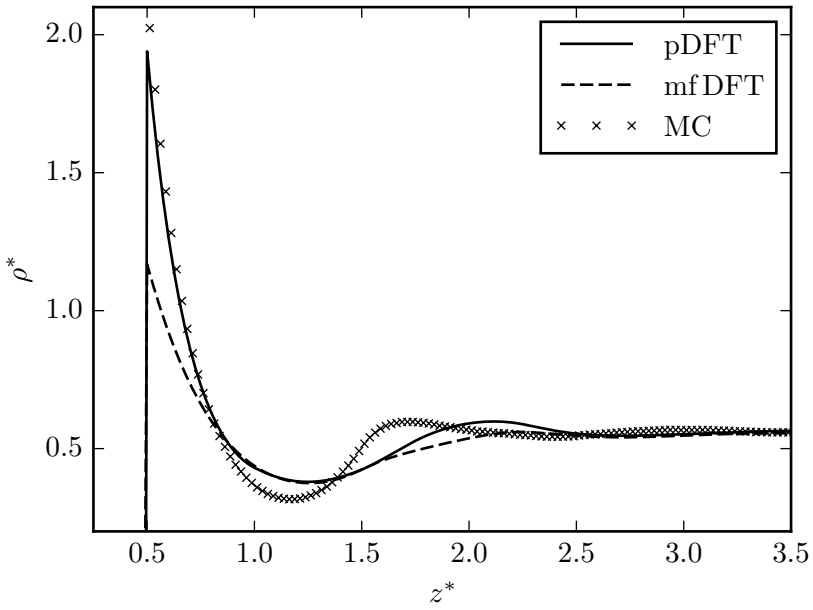

Figure 7.2.: The density distribution $\rho^* = \rho\sigma^3$ of the Jagla fluid in a slit with hard walls and reduced length $l = L/\sigma = 22$ at $(\eta, T^*) = (0.3, 1.0)$ described by means of perturbation DFT (solid line), standard mean-field DFT (dashed-line) and MC simulations (crosses). The abscissa provides the reduced distance $z^* = z/\sigma$ from the left wall.

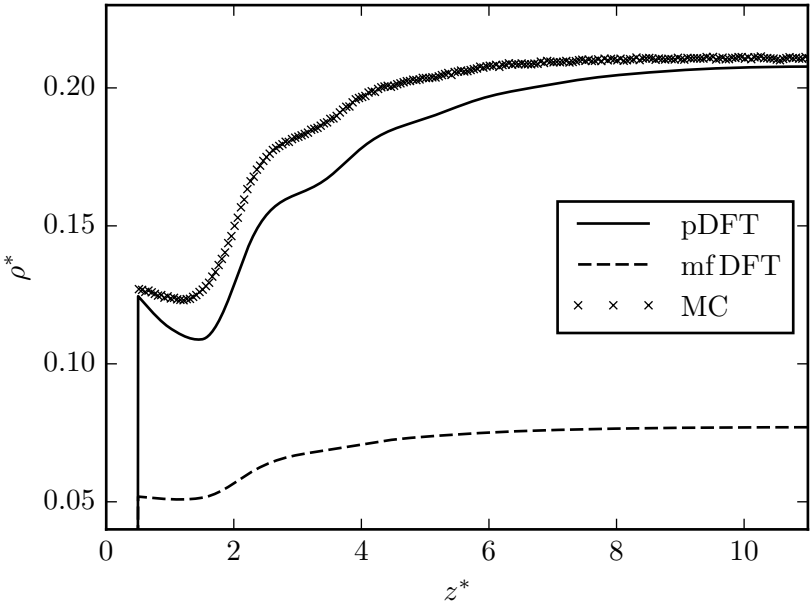

Figure 7.3.: The density distribution $\rho^* = \rho\sigma^3$ of the Jagla fluid in a slit with hard walls and reduced length $l = L/\sigma = 22$ at $(\eta, T^*) = (0.1, 0.5)$ described by means of perturbation DFT (solid line), standard mean-field DFT (dashed-line) and MC simulations (crosses). The abscissa provides the reduced distance $z^* = z/\sigma$ from the left wall.

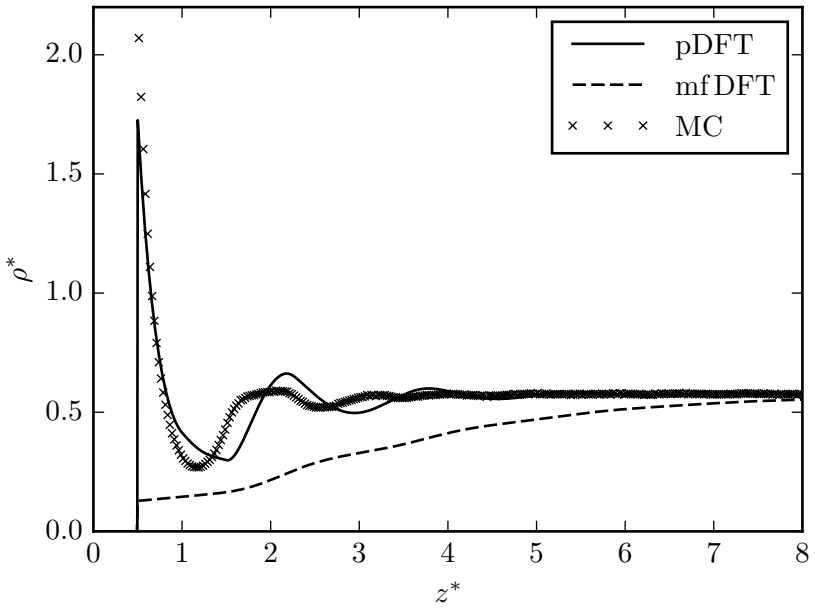

Figure 7.4.: The density distribution $\rho^* = \rho\sigma^3$ of the Jagla fluid in a slit with hard walls and reduced length $l = L/\sigma = 22$ at $(\eta, T^*) = (0.3, 0.5)$ described by means of perturbation DFT (solid line), standard mean-field DFT (dashed-line) and MC simulations (crosses). The abscissa provides the reduced distance $z^* = z/\sigma$ from the left wall.

that at state points in the vicinity of the corresponding binodal line (circles and solid line, respectively, in Fig. 6.12) DFT has especially difficulties producing correct results.

Even closer to the liquid-liquid binodal at $(\eta, T^*) = (0.3, 0.3)$, also perturbation DFT fails to reproduce the structure of the MC density profile and exhibits unphysical oscillations. This is depicted in Fig. 7.5. Furthermore, mean-field DFT, being considered at a state point in the unstable region of its bulk phase diagram, erroneously predicts a gas phase. At even lower temperatures, the unphysical oscillations of perturbation DFT become only worse, and, hence, we, obviously, have reached a point where the results of our perturbation theory are not meaningful anymore. The liquid-liquid critical point derived by our bulk perturbation approach, however, lies clearly below $T^* = 0.3$. This poses a major problem, since our motivation to derive a DFT for the Jagla fluid is to examine its liquid-liquid binodal line under confinement. Evidently, the perturbation DFT derived above is of no use for this purpose.

7.3. Conclusions and outlook

Above results show that, obviously, the information on the Jagla potential and the Jagla fluid's bulk structure, which enters perturbation DFT via $v_{\mathrm{rep}}(r_{12})$, $w(r_{12})$, and $g_0^{\mathrm{b}}(r_{12}; \rho_{\mathrm{b}})$ in Eq. (7.10), is not sufficient for the prediction of the fluid's behavior under confinement at low temperatures and close to the binodal line. The perturbation techniques applied in this work are constructed such that the system of interest, i.e. the particle-particle interaction potential of interest, is split into a well-known reference system and a perturbation which is coupled to the reference potential via the coupling parameter λ [see Eqs. (6.1) and (7.4)]. The parameter

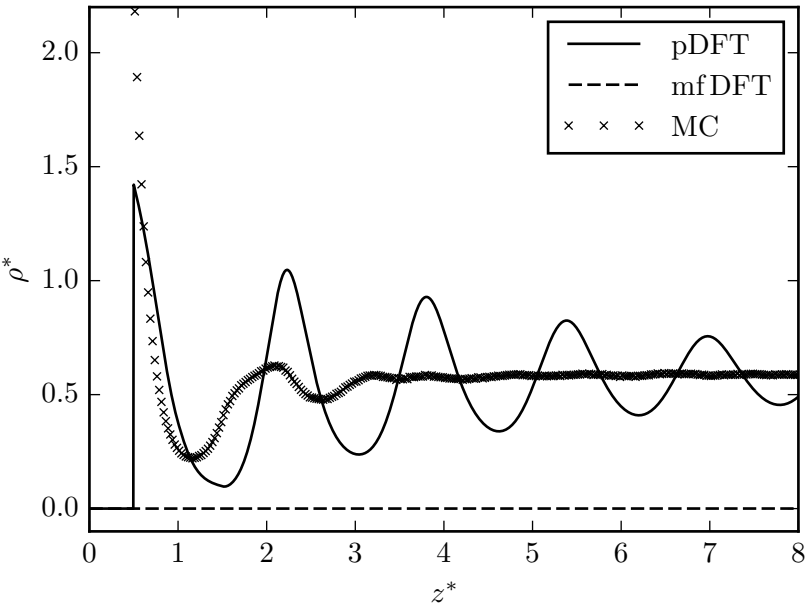

Figure 7.5.: The density distribution $\rho^* = \rho\sigma^3$ of the Jagla fluid in a slit with hard walls and reduced length $l = L/\sigma = 22$ at $(\eta, T^*) = (0.3, 0.3)$ described by means of perturbation DFT (solid line), standard mean-field DFT (dashed-line) and MC simulations (crosses). The abscissa provides the reduced distance $z^* = z/\sigma$ from the left wall.

λ and the perturbation potential thus appear in the expressions of the excess free energy F^{ex} [Eq. (2.12)] and the intrinsic excess free energy functional $\mathcal{F}^{\mathrm{ex}}$ [Eq. (7.6)]. For the bulk expression F^{ex}, subsequently, a series expansion in powers of the parameter λ is made which is normally aborted after the first or second order term as the higher order expressions are too complicated to evaluate. Note that the second order term is usually already approximated [see Sec. 6.1.1 and Eq. (6.18)]. The low-order expansion, of course, only yields reasonable results if the perturbation is small compared to the reference. In the inhomogeneous case, the expression for $\mathcal{F}^{\mathrm{ex}}$ is approximated by substituting the 2-particle distribution function $g^{(2)}(\mathbf{r_1}, \mathbf{r_2}; \lambda)$ of the actual inhomogeneous system with the 2-particle distribution function $g_0^{(2)}(\mathbf{r_1}, \mathbf{r_2})$ of the inhomogeneous (repulsive) reference system. Certainly, this approximation works the better, the smaller the perturbation, i.e. the more similar the two radial distribution functions.

In the case of the Jagla fluid, none of the two key requirements for a successfully working perturbation theory is optimally met. Firstly, the perturbation is not small compared to the reference system due to the long range of the perturbation potential $w(r)$. Hence, aborting the λ- or high temperature expansion after the first or second term (bulk system), as well as substituting $g^{(2)}(\mathbf{r_1}, \mathbf{r_2}; \lambda)$ with $g_0^{(2)}(\mathbf{r_1}, \mathbf{r_2})$ (inhomogeneous case) is not optimal. Secondly, the properties of the reference system [with interaction potential $v_0(r)$] are not well-known, and, hence, we have to apply the perturbation techniques again, to describe the reference system as a combination of a hard-sphere system and a repulsive ramp. While the hard-sphere system is well-described in bulk and in the inhomogeneous case (e.g. via FMT [30, 32]), the long-ranged repulsive ramp of the Jagla potential, again, is not a small perturbation to the hard sphere system creating more

inaccuracies. This is essentially the reason why the BH and WCA perturbation theories fail to describe the Jagla fluid (see discussion in Sec. 6.2.2). Here, the reference potential $v_0(r)$, i.e. the repulsive ramp, is mapped onto an effective hard-sphere system with effective hard-sphere diameter d [see Sec. 6.2 and Eq. (6.32)]. The long range of the Jagla potential's repulsive part becomes obvious, if the ratio of the effective diameter d and the actual hard-sphere diameter σ is compared to the corresponding ratio of the Lennard-Jones fluid [Figs. 6.6 and 1.1].

While, despite their shortcomings discussed in this section, the techniques applied here yield reasonable results for the bulk system, in the inhomogeneous case the Jagla fluid is described correctly only at state points at high temperatures not too close to the binodal. Close to the binodal line and at low temperatures, perturbation DFT, for which further approximations are applied when the 2-particle distribution functions of the inhomogeneous systems are substituted with the corresponding bulk radial distribution functions, fails to describe the Jagla fluid correctly.

The shortcomings of DFT discussed herein might be remedied by feeding it (quasi-exact) MC simulation data as is suggested in the outlook of Ref. [33]. This is the topic of the following chapters.

8. Monte-Carlo-optimized DFT

8.1. The idea

In Chpt. 7 the poor performance of perturbation DFT to describe the inhomogeneous Jagla fluid at low temperatures and in states close to the binodals of the bulk phase diagram was discussed. These shortcomings motivate the idea, initially formulated in Ref. [33], to feed standard mean-field DFT quasi-exact Monte-Carlo simulation data to gain a (mean-field) DFT which produces correct results also at low temperatures. In particular, the aim of this chapter is to use MC data, in fact cavity distribution function $y(r)$ [see Eq. (3.8)] and radial distribution function $g(r)$ (see Secs. 2.2 and 3.2), to derive a, with respect to mean-field DFT, optimized interaction potential for the Jagla fluid in the test particle geometry and subsequently in the infinite slit geometry to gain an accurate mean-field DFT description (density profiles and phase behavior) of the inhomogeneous fluid. This, eventually, would enable us to alter the Jagla fluid's phase diagram due to the confining slit. Here, the challenge clearly is to transfer the results from the test particle geometry to the infinite slit geometry.

This ansatz might sound similar to the uniqueness theorem for fluid pair correlation functions [21] by Henderson, but clearly is a different approach. Under the assumption of only pairwise interactions, the uniqueness theorem states that, for a given temperature and density, two pair potentials which give rise to the same radial distribution function $g(r)$ can at most differ by a

constant [21]. It is not our aim to use the MC radial distribution function to find this, up to a constant, unique interaction potential of the "exact" theory. In fact, we already know the form of the Jagla potential which is why we are able to calculate the corresponding radial distribution function. Instead, we want to derive an interaction potential which is optimized for the use within standard mean-field DFT and thus makes up for the shortcomings of this approximate theory.

8.2. Theory

In the original study [33] on this topic the comparison of classical DFT and MC simulations is limited to hard spheres, and the functional $\mathcal{F}_{\text{ex}}[\rho]$ of the excess intrinsic free energy is given by FMT [30, 32] (see Chpt. 4.2). In the present analysis, we want to extent the concept to spherically symmetric fluids with a hard core repulsion at small distances and an additional soft tail by deploying standard mean-field DFT (see Sec 7.1.2). The mean-field expression of the functional of the intrinsic excess free energy reads [c.f. Eq. (7.13)]:

$$\mathcal{F}^{\text{ex}}[\rho(\mathbf{r})] = \mathcal{F}^{\text{ex}}_{\text{hs}}[\rho(\mathbf{r})] + \frac{1}{2}\iint \mathrm{d}\mathbf{r}_1\mathrm{d}\mathbf{r}_2\rho(\mathbf{r}_1)\rho(\mathbf{r}_2)w(r_{12}), \quad (8.1)$$

where $\mathcal{F}^{\text{ex}}_{\text{hs}}[\rho(\mathbf{r})]$ is the intrinsic free energy functional of the hard-sphere reference system for which we apply the White Bear version [31] (see Chpt. 4.2) of FMT, and $w(r)$ is the perturbation potential. As before, the quantity $r_{12} = |\mathbf{r}_2 - \mathbf{r}_1|$ denotes the center-to-center distance of the particles labeled 1 and 2.

For the discussion which follows, it is important to note that there is an important difference between the particle-particle interaction potential $v(r)$ and the associated perturbation potential

$w(r)$ in the mean-field approach applied in the present study. While the two are equal outside the hard core ($r \geq \sigma$), namely the soft tail of the interaction potential, they can differ inside the hard core ($r < \sigma$), where, obviously, $v(r)$ is the hard-sphere potential, whereas there usually is a freedom of choice for the perturbation potential's behavior. In perturbation theories the behavior of the perturbation potential inside the core is commonly chosen such that the results are optimized. A well-known example is the square-well fluid for which the potential well of the perturbation potential is extended into the hard core to optimize the bulk phase behavior.

As suggested in the outlook of Ref. [33], we want to derive an, with respect to standard mean-field DFT, optimized particle-particle interaction potential $v_{\text{opt}}(r)$ and the associated perturbation potential $w_{\text{opt}}(r)$ via the Euler-Lagrange equation of DFT [see Eq. (4.5)] in the test particle geometry (see Sec. 5.1) by employing (quasi-exact) MC simulation data. The optimized potential(s) shall then reproduce the Monte-Carlo density profile once plugged into the original mean-field DFT framework. In a second step, we try to optimize the interaction potential in such a way that it also can be applied to the infinite slit geometry (see the beginning of Sec. 7.2). While, in the following, we limit our investigation to the Jagla fluid, we emphasize that the techniques employed are also applicable to other spherically symmetric fluids with hard-core-plus-soft-tail interaction potential.

8.2.1. Via the cavity distribution function

In a first attempt, our ansatz for the optimized potential is

$$v_{\text{opt}}(r) = v_{\text{hs}}(r) + w_{\text{J}}(r) + w_1(r),$$

where $v_{\mathrm{hs}}(r)$ is the hard-sphere potential, $w_{\mathrm{J}}(r)$ is the soft tail of the Jagla potential, i.e., $w_{\mathrm{J}}(r < \sigma) = 0$, and $w_1(r)$ is a correction added to w_{J}, which, in general, is not zero for $r < \sigma$. Thus in our case, $w(r)$ in Eq. (8.1) is equal to $w_{\mathrm{J}}(r) + w_1(r)$. The determination of $w_1(r)$ is the goal of this section. To this end, we rewrite[1] the Euler-Lagrange equation of DFT [Eq. (4.5)] in terms of the cavity distribution function $y(r)$ for the test particle geometry to be:

$$\frac{\delta\beta\Omega}{\delta\rho(\mathbf{r})} = \ln\big(y(r)\big) + \frac{\delta\beta\mathcal{F}^{\mathrm{ex}}}{\delta\rho(\mathbf{r})} - \beta\mu^{\mathrm{ex}} = 0. \tag{8.2}$$

[1] First, we use that in the test particle geometry $\rho(\mathbf{r}) = \rho(r) = \rho_{\mathrm{b}} g(r)$ holds. Thus, Eq. (4.5) becomes

$$\ln\big(g(r)\big) + \frac{\delta\beta\mathcal{F}^{\mathrm{ex}}}{\delta\rho(\mathbf{r})} + \beta V_{\mathrm{ext}}(\mathbf{r}) - \beta\mu^{\mathrm{ex}} = 0$$

Now, we use that $\beta V_{\mathrm{ext}}(\mathbf{r}) = \ln\Big(\exp\big(\beta V_{\mathrm{ext}}(\mathbf{r})\big)\Big)$, and that in the test particle geometry $V_{\mathrm{ext}}(\mathbf{r}) = V_{\mathrm{ext}}(r) = v(r)$ with the particle-particle interaction potential $v(r) = v_{\mathrm{opt}}(r)$. With this, we obtain

$$\ln\Big(g(r)\exp\big(\beta v_{\mathrm{opt}}(r)\big)\Big) + \frac{\delta\beta\mathcal{F}^{\mathrm{ex}}}{\delta\rho(\mathbf{r})} - \beta\mu^{\mathrm{ex}} = 0.$$

Finally, we make use of the definition of the cavitiy distribution function, Eq. (3.8), and find the expression in Eq. (8.2):

$$\ln\big(y(r)\big) + \frac{\delta\beta\mathcal{F}^{\mathrm{ex}}}{\delta\rho(\mathbf{r})} - \beta\mu^{\mathrm{ex}} = 0.$$

With Eq. (8.1), $w(r) = w_{\mathrm{J}}(r) + w_1(r)$, and Eq. (7.14), we can rewrite the functional derivative of $\mathcal{F}^{\mathrm{ex}}$ and obtain

$$\begin{aligned}\frac{\delta\beta\Omega}{\delta\rho(\mathbf{r})} &= \ln\big(y(r)\big) + \frac{\delta\beta\mathcal{F}^{\mathrm{ex}}_{\mathrm{hs}}}{\delta\rho(\mathbf{r})} \\ &\quad + \int \mathrm{d}\mathbf{r}_1 \rho(\mathbf{r}_1)\beta w_{\mathrm{J}}(|\mathbf{r}-\mathbf{r}_1|) \\ &\quad + \int \mathrm{d}\mathbf{r}_1 \rho(\mathbf{r}_1)\beta w_1(|\mathbf{r}-\mathbf{r}_1|) \\ &\quad - \beta\mu^{\mathrm{ex}} \\ &= \ln\big(y(r)\big) + \frac{\delta\beta\mathcal{F}^{\mathrm{ex}}_{\mathrm{hs}}}{\delta\rho(\mathbf{r})} \\ &\quad + \big(\rho * \beta w_{\mathrm{J}}\big)(r) + \big(\rho * \beta w_1\big)(r) - \beta\mu^{\mathrm{ex}} = 0, \end{aligned} \tag{8.3}$$

where the integrals are rewritten as convolutions in the second equation. Now, instead of solving Eq. (8.3) for the density profile (which we could not do, because $w_1(r)$ is unknown), we plug in the quasi-exact density profile $\rho^{\mathrm{J}}_{\mathrm{mc}}(r)$ of the test particle geometry of the Jagla fluid which is obtained from a MC simulation and, hence, is denoted by the index 'mc'. The MC simulation calculates the quasi-exact bulk radial distribution function $g^{\mathrm{J}}_{\mathrm{mc}}(r)$ of the Jagla fluid, and we subsequently make use of the fact that $\rho^{\mathrm{J}}_{\mathrm{mc}}(r) = \rho_{\mathrm{b}} g^{\mathrm{J}}_{\mathrm{mc}}(r)$ holds in the test particle geometry. We note that the MC input data is somewhat smoothed to ensure that noise do not cause strong numerical artifacts. Furthermore, we plug into (8.3) the cavity distribution function $y^{\mathrm{J}}_{\mathrm{mc}}(r)$ of the Jagla fluid which we compute by employing the direct MC simulation method described in the work by Llano-Restrepo and Chapman [23]. From (3.8) we see that $y(r) = g(r)$ holds for all distances r for which the interaction potential $v(r)$ vanishes. Since the Jagla potential $v_{\mathrm{J}}(r)$ has a finite range, we use this identity to verify our results for $y^{\mathrm{J}}_{\mathrm{mc}}(r)$. Finally, we plug into Eq. (8.3) the mean-field expression

of the excess chemical potential of the Jagla fluid, $\mu^{\mathrm{ex}}_{\mathrm{mf,J}}$, which is given by Eq. (6.30) and can be easily calculated, where $w(r)$ in (6.30) now is the soft tail $w_{\mathrm{J}}(r)$ of the Jagla fluid. With this we obtain:

$$\begin{aligned}\left.\frac{\delta\beta\Omega}{\delta\rho(\mathbf{r})}\right|_{\rho^{\mathrm{J}}_{\mathrm{mc}}(r)} &= \ln\left(y^{\mathrm{J}}_{\mathrm{mc}}(r)\right) + \left.\frac{\delta\beta\mathcal{F}^{\mathrm{ex}}_{\mathrm{hs}}}{\delta\rho(\mathbf{r})}\right|_{\rho^{\mathrm{J}}_{\mathrm{mc}}(r)} \\ &\quad + \left(\rho^{\mathrm{J}}_{\mathrm{mc}} * \beta w_{\mathrm{J}}\right)(r) + \left(\rho^{\mathrm{J}}_{\mathrm{mc}} * \beta w_1\right)(r) - \beta\mu^{\mathrm{ex}}_{\mathrm{mf,J}} \\ &= 0. \end{aligned} \tag{8.4}$$

The only unknown quantity in Eq. (8.4) is the potential correction $w_1(r)$ and, thus, we rewrite it to be

$$\begin{aligned}\rho^{\mathrm{J}}_{\mathrm{mc}} * \beta w_1 &= -\Bigg[\ln\left(y^{\mathrm{J}}_{\mathrm{mc}}(r)\right) + \left.\frac{\delta\beta\mathcal{F}^{\mathrm{ex}}_{\mathrm{hs}}}{\delta\rho(\mathbf{r})}\right|_{\rho^{\mathrm{J}}_{\mathrm{mc}}(r)} \\ &\qquad + \rho^{\mathrm{J}}_{\mathrm{mc}} * \beta w_{\mathrm{J}} - \beta\mu^{\mathrm{ex}}_{\mathrm{mf,J}}\Bigg] \\ &\equiv u(r), \end{aligned} \tag{8.5}$$

where, for reasons of simplicity, we term the right side $u(r)$. Note, that $u(r)$ is also well defined for $r < \sigma$ and unequal zero, and, hence, the same holds for the solution $w_1(r)$. If we manage to accurately solve Eq. (8.5) for $w_1(r)$, we are able to reproduce the MC density profile $\rho^{\mathrm{J}}_{\mathrm{mc}}(r)$ with mean-field DFT with $w_1(r)$ as perturbation potential. To determine the latter, we make use of the convolution theorem which states that the Fourier transform of a convolution of two functions $f(\mathbf{r})$ and $g(\mathbf{r})$ is equal to the product of the Fourier transforms of the functions: $\mathfrak{F}[f*g] = \mathfrak{F}[f]\,\mathfrak{F}[g]$, where $\mathfrak{F}$ denotes the three-dimensional Fourier transform. If we now apply the Fourier transform on either sides of Eq. (8.5) as well as the convolution theorem , we obtain

$$\mathfrak{F}\left[\rho^{\mathrm{J}}_{\mathrm{mc}}(r)\right](k)\,\mathfrak{F}\left[\beta w_1(r)\right](k) = \mathfrak{F}\left[u(r)\right](k)$$

which can be rewritten to be

$$\beta w_1(r) = \mathfrak{F}^{-1}\left[\frac{\mathfrak{F}\left[u(r)\right]}{\mathfrak{F}\left[\rho^{\mathrm{J}}_{\mathrm{mc}}(r)\right]}\right], \tag{8.6}$$

where $\mathfrak{F}^{-1}$ denotes the inverse Fourier transform, i.e., $\mathfrak{F}^{-1}\,\mathfrak{F} = \mathrm{id}$. This approach, however, is not as straight forward as it might seem at first glance. The (discrete) Fourier transform $\mathfrak{F}(\rho^{\mathrm{J}}_{\mathrm{mc}}(r))(k)$ of the density profile $\rho^{\mathrm{J}}_{\mathrm{mc}}(r)$ oscillates around zero while decaying, hence, causing the fraction in Eq. (8.6) to become extremely large at certain points where $\mathfrak{F}(\rho^{\mathrm{J}}_{\mathrm{mc}}(r))(k)$ is close to zero. This is especially the case for large values of k, and causes inaccuracies in the result $\beta w_1(r)$. We tried to overcome this issue by fitting a high order polynomial to the data points of the fraction of Fourier transforms at which the large values occur. This, however, could not improve the outcome enough to derive a potential correction $w_1(r)$ which is sufficiently accurate to reproduce the MC density profile with mean-field DFT.

8.2.2. Via the radial distribution function

In a second approach, we implement all calculations in real space. For this, we apply an interaction potential $v_{\mathrm{opt}}(r)$ which is of the form $v_{\mathrm{opt}}(r) = v_{\mathrm{hs}}(r) + w_{\mathrm{opt}}(r)$ with the perturbation potential $w_{\mathrm{opt}}(r)$. Furthermore, we substitute $y(r)$ in Eq. (8.2) via $y(r) = \exp\left[\beta v_{\mathrm{opt}}(r)\right] g(r)$ which yields a Euler-Lagrange equation that contains the radial distribution function $g(r)$:

$$\frac{\delta\beta\Omega}{\delta\rho(\mathbf{r})} = \ln\left(g(r)\right) + \frac{\delta\beta\mathcal{F}^{\mathrm{ex}}}{\delta\rho(\mathbf{r})} + \beta v_{\mathrm{opt}}(r) - \beta\mu^{\mathrm{ex}} = 0.$$

As in Sec. 8.2.1, we use Eq. (8.1) to rewrite the functional derivative of $\mathcal{F}^{\mathrm{ex}}$, and we plug in the quasi-exact MC simulation data

in terms of the density profile $\rho^{\mathrm{J}}_{\mathrm{mc}}(r)$ of the test particle geometry and the radial distribution function $g^{\mathrm{J}}_{\mathrm{mc}}(r)$ of the Jagla fluid. Also as above, we plug in the mean-field expression of the excess chemical potential $\mu^{\mathrm{ex}}_{\mathrm{mf,J}}$. With this we obtain:

$$\begin{aligned}\left.\frac{\delta\beta\Omega}{\delta\rho(\mathbf{r})}\right|_{\rho^{\mathrm{J}}_{\mathrm{mc}}(r)} &= \ln\left(g^{\mathrm{J}}_{\mathrm{mc}}(r)\right) + \left.\frac{\delta\beta\mathcal{F}^{\mathrm{ex}}_{\mathrm{hs}}}{\delta\rho(\mathbf{r})}\right|_{\rho^{\mathrm{J}}_{\mathrm{mc}}(r)} \\ &\quad + \left(\rho^{\mathrm{J}}_{\mathrm{mc}} * \beta w_{\mathrm{opt}}\right)(r) + \beta v_{\mathrm{opt}}(r) - \beta\mu^{\mathrm{ex}}_{\mathrm{mf,J}} \\ &= 0. \end{aligned} \tag{8.7}$$

Since both unknown functions $\beta v_{\mathrm{opt}}(r)$ and $\beta w_{\mathrm{opt}}(r)$ occur in Eq. (8.7), it can only be quasi-solved for $\beta v_{\mathrm{opt}}(r)$:

$$\begin{aligned}\beta v_{\mathrm{opt}}(r) = &- \ln\left(g^{\mathrm{J}}_{\mathrm{mc}}(r)\right) - \left.\frac{\delta\beta\mathcal{F}^{\mathrm{ex}}_{\mathrm{hs}}}{\delta\rho(\mathbf{r})}\right|_{\rho^{\mathrm{J}}_{\mathrm{mc}}(r)} \\ &- \left(\rho^{\mathrm{J}}_{\mathrm{mc}} * \beta w_{\mathrm{opt}}\right)(r) + \beta\mu^{\mathrm{ex}}_{\mathrm{mf,J}}; \end{aligned} \tag{8.8}$$

yet, it can be solved numerically by using e.g. a Piccard iteration. This procedure is equivalent to the standard functional minimization in DFT. The only difference is that now the (quasi-exact) MC density profile is the input, and the result is the (optimized) interaction potential, whereas in standard DFT the interaction potential is the input, and the equilibrium density profile the output. Unlike in Eq. (8.5), the right side of Eq. (8.8) is not well defined for $r < \sigma$, as $g^{\mathrm{J}}_{\mathrm{mc}}(r < \sigma) = 0$, and therefore is only valid for $r \geq \sigma$. This gives us a freedom of choice for the behavior of the perturbation potential $\beta w_{\mathrm{opt}}(r)$ inside the hard core. In the

$(i+1)$-th iteration step, Eq. (8.8) takes the shape

$$\begin{aligned}\beta v^{(i+1)}(r) = (1-\alpha)\beta v^{(i)}(r) \\ + \alpha\Bigg[- \ln\left(g^{\mathrm{J}}_{\mathrm{mc}}(r)\right) - \left.\frac{\delta\beta\mathcal{F}^{\mathrm{ex}}_{\mathrm{hs}}}{\delta\rho(\mathbf{r})}\right|_{\rho^{\mathrm{J}}_{\mathrm{mc}}(r)} \\ - \left(\rho^{\mathrm{J}}_{\mathrm{mc}} * \beta w^{(i)}\right)(r) + \beta\mu^{\mathrm{ex}}_{\mathrm{mf}}(w^{(i)}(r))\Bigg], \quad (8.9)\end{aligned}$$

where we have introduced the parameter α which mixes the old solution $\beta v^{(i)}(r)$ with the new solution (the term in brackets), to avoid divergence in the iteration. Only the convolution and the excess chemical potential must be calculated in every iteration step, whereas the functional derivative of $\beta\mathcal{F}^{\mathrm{ex}}_{\mathrm{hs}}$ has to be calculated only once. The initial perturbation potential $w^{(0)}(r)$ we set to be the Jagla potential $v_{\mathrm{J}}(r)$ for $r \geq \sigma$; the choice of the behavior of $w^{(0)}(r)$ for $r < \sigma$ we discuss in Sec. 8.3. Since Eq. (8.9) is only valid outside the hard core, $w^{(i)}(r < \sigma) = w^{(0)}(r < \sigma)$ holds for all values of i. It is important to note that the behavior of the perturbation potentials $w^{(i)}$ for $r < \sigma$ influences the updated potential $v^{(i+1)}(r)$ outside the hard core via the convolution $\left(\rho_{\mathrm{mc}} * \beta w^{(i)}\right)(r)$ and the excess chemical potential $\mu^{\mathrm{ex}}(w^{(i)}(r))$. Nevertheless, if in the original test particle mean-field DFT the optimized perturbation potential is applied which is composed of the chosen behavior inside the core and the associated potential behavior outside the core which was determined with Eq. (8.9), the correct MC density profile is recovered, independent of the actual choice of $w^{(i)}(r < \sigma)$. Although not implied in the notation so far, the procedure discussed as of yet must be executed for every state point (η, T^*) of interest to obtain optimal results. This leads to an optimized potential of the form $v_{\mathrm{opt}}(r; \eta, T^*)$ with associated perturbation potential $w_{\mathrm{opt}}(r; \eta, T^*)$. In practice,

executing the optimization algorithm at certain state points and applying a fit through the thus gained optimized perturbation potentials works well to obtain a continuous optimized perturbation potential.

8.2.3. Optimizing the behavior of the bulk pressure

In the mean-field approach, for a given hard-core-plus-soft-tail interaction potential $v(r;\eta,T^*)$ (not necessarily derived via the techniques discussed in this chapter as of yet), the behavior of the associated perturbation potential inside the hard core can be utilized to optimize the behavior of the bulk pressure of the corresponding fluid. To do so, we use bulk pressure data gained by canonical MC simulations. The mean-field expression of the bulk pressure p of a fluid with a particle-particle interaction potential which is a function of the density, or the packing fraction, reads

$$\begin{aligned}\beta p = \rho\, &\frac{1+\eta+\eta^2-\eta^3}{(1-\eta)^3} \\ &+ \frac{2\pi\rho^2}{T^*}\left[I(\eta,T^*)+\eta\frac{\partial I(\eta,T^*)}{\partial\eta}\right],\end{aligned} \tag{8.10}$$

where the first term is the Carnahan-Starling expression for the hard-sphere pressure [7], and $I(\eta,T^*)$ denotes the integral

$$I(\eta,T^*) = \int_0^\infty \mathrm{d}r\, r^2 \beta w(r;\eta,T^*), \tag{8.11}$$

with the perturbation potential $w(r;\eta,T^*)$. Unlike in Eq. (6.31), the integral I now is a function of the packing fraction η, or the bulk density ρ, since the perturbation potential now is a function of the packing fraction. This has to be taken into account in the calculation of the mean-field expression of the pressure in terms

of the derivative of I with respect to η. Given the MC pressure data, Eq. (8.10) can be rewritten as a first-order linear ordinary differential equation for the expression $I(\eta, T^*)$:

$$\frac{\partial I(\eta, T^*)}{\partial \eta} = -\frac{I(\eta, T^*)}{\eta} + b(\eta, T^*). \tag{8.12}$$

Here, the expression $b(\eta, T^*)$ contains the CS pressure and the MC pressure data. Equation (8.12) can easily be solved numerically to obtain $I(\eta, T^*)$. Furthermore, we can write the integral in Eq. (8.11) as

$$\begin{aligned} I(\eta, T^*) &= \int_0^\sigma \mathrm{d}r\, r^2 \beta w(r; \eta, T^*) + \int_\sigma^\infty \mathrm{d}r\, r^2 \beta w(r; \eta, T^*) \\ &\equiv I_{\mathrm{core}}(\eta, T^*) + I_{\mathrm{ext}}(\eta, T^*). \end{aligned} \tag{8.13}$$

As we assume a given hard-core potential $v(r; \eta, T^*)$, the exterior integral I_{ext} is known, and we can solve Eq. (8.13) for I_{core}. Here, only the value of the core integral is of importance; hence, we can assume the perturbation potential $w(r; \eta, T^*)$ to be a constant $\beta c(\eta, T^*)$ inside the core, and thus write

$$\begin{aligned} I_{\mathrm{core}}(\eta, T^*) &= \beta c(\eta, T^*) \int_0^\sigma \mathrm{d}r\, r^2 \\ &\overset{\left(\text{Eq. (8.13)}\right)}{=} I(\eta, T^*) - I_{\mathrm{ext}}(\eta, T^*). \end{aligned} \tag{8.14}$$

Equation (8.14) can now easily be solved for the constant $c(\eta,T^*)$:

$$\beta c(\eta, T^*) = \frac{3}{\sigma^3}\Big[I(\eta, T^*) - I_{\mathrm{ext}}(\eta, T^*)\Big].$$

If we plug the thus gained perturbation potential (core plus exterior) back into Eq. (8.10), we recover the MC pressure.

8.3. Results and discussion

We apply the techniques discussed in Sec. 8.2.2 to study the inhomogeneous Jagla fluid. The phase behavior of the latter, and especially the appearance of a liquid-liquid critical point, we tried to investigate in Chpt. 7 by application of the perturbation DFT which ultimately failed at low temperatures and close to the binodals.

8.3.1. Test particle geometry

To obtain the optimized perturbation potential $w_{\mathrm{opt}}(r;\eta,T^*)$ for the test particle geometry, we apply the iteration in Eq. (8.9), where we choose the perturbation potential to be zero for $r < \sigma$, and, furthermore, force it to be zero for $r > a_{\max}\,\sigma$, to have a finite range; i.e., the potential in the iteration is only updated at $\sigma \leq r \leq a_{\max}\,\sigma$. Here, our choice of the parameter $a_{\max}$ depends on the state point (η, T^*) at which the optimization is carried out. Subsequently, we apply the potential $w_{\mathrm{opt}}(r;\eta,T^*)$ in a standard mean-field DFT code for the test particle geometry and find excellent agreement between DFT and (initial) MC results in a wide range of the parameters T^* and η. While a value of $a_{\max} = 20\,\sigma$ yields excellent results at high temperatures ($T^* \approx 1.0$), we have to reduce the range of $w_{\mathrm{opt}}(r)$ at lower temperatures ($a_{\max} = 5\,\sigma$ at $T^* = 0.1$) to ensure convergence of both the iteration to find the optimized potential and the actual mean-field DFT code run with the optimized potential. This in turn causes small deviations between DFT and MC results for $r > a_{\max}$. These differences, however, are smaller than the accuracy of the corresponding plots (Fig. 8.2). We note that, unless otherwise stated, all MC results presented here are computed using a standard canonical Metropolis [25] MC algorithm.

Figure 8.1 shows a comparison of the radial distribution functions, at the state point $(\eta, T^*) = (0.1, 1.0)$, calculated by means of MC simulations, the optimized DFT, and standard mean-field DFT, the latter being a mean-field DFT where the particles interact via the Jagla potential v_{J} and *not* via the optimized potential. As already mentioned, the agreement between MC and optimized DFT data is excellent, while mean-field DFT already predicts an inaccurate contact value. Figure 8.2 depicts the radial distribution functions of MC simulation and optimized DFT at $(\eta, T^*) = (0.3, 0.1)$. Even tough we have to reduce the range of $a_{\max}$ to $5\,\sigma$, to ensure convergence of the code, the thus caused deviations are still smaller than the accuracy of the plot, whereas mean-field DFT, being in its unstable region at this particular state point (see Fig. 8.10), fails to converge. For the two state points considered here, the soft tails of the optimized interaction potentials v_{opt} are shown in Fig. 8.3. We observe that at high temperatures, where mean-field DFT still predicts results in the range of the MC data, the changes in the interaction potential necessary to acquire accurate results are rather small. However, at lower temperatures and in the unstable region of mean-field theory, the interaction potential needs to be modified dramatically to compensate the shortcomings of mean-field DFT.

8.3.2. Infinite slit geometry

To study the phase behavior of the Jagla fluid under confinement, we extent the techniques described in Sec. 8.3.1 to the infinite slit geometry (see Sec. 7.2). As the iteration technique [Eq. (8.9)] to determine the optimized interaction potential is applicable only in the test particle geometry - there the external potential is equal to the particle-particle interaction potential - but not in the slit geometry, we use the freedom of choice of the pertur-

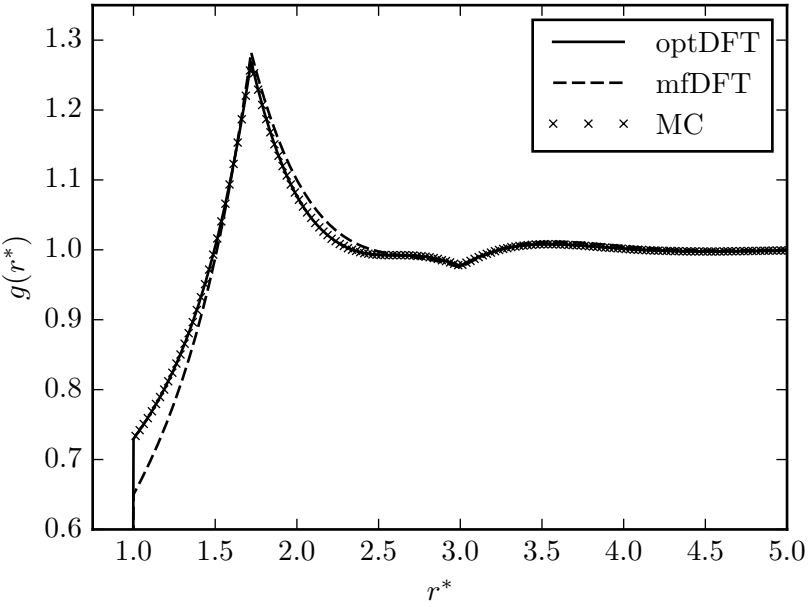

Figure 8.1.: The radial distribution function $g(r^*)$ of the Jagla fluid as a function of the reduced center-to-center particle distance $r^* = r/\sigma$ at $(\eta, T^*) = (0.1, 1.0)$ calculated by means of Monte Carlo simulations (crosses), the optimized DFT (solid line), and standard mean-field DFT (dashed line). The cutoff parameter $a_{\max}$ of the optimized potential was set to $20\,\sigma$.

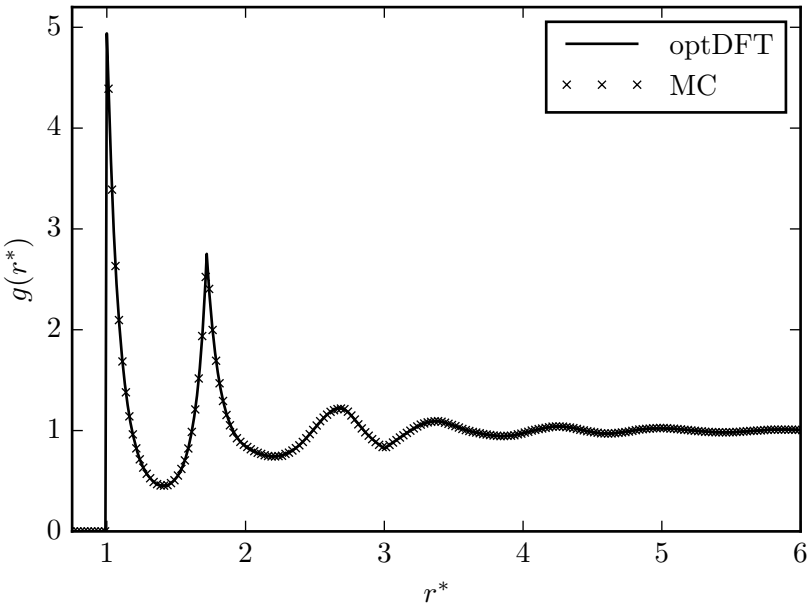

Figure 8.2.: The radial distribution function $g(r^*)$ of the Jagla fluid as a function of the reduced center-to-center particle distance $r^* = r/\sigma$ at $(\eta, T^*) = (0.3, 0.1)$ calculated by means of Monte Carlo simulations (crosses) and the optimized DFT (solid line). The cutoff parameter $a_{\max}$ of the optimized potential was set to $5\,\sigma$.

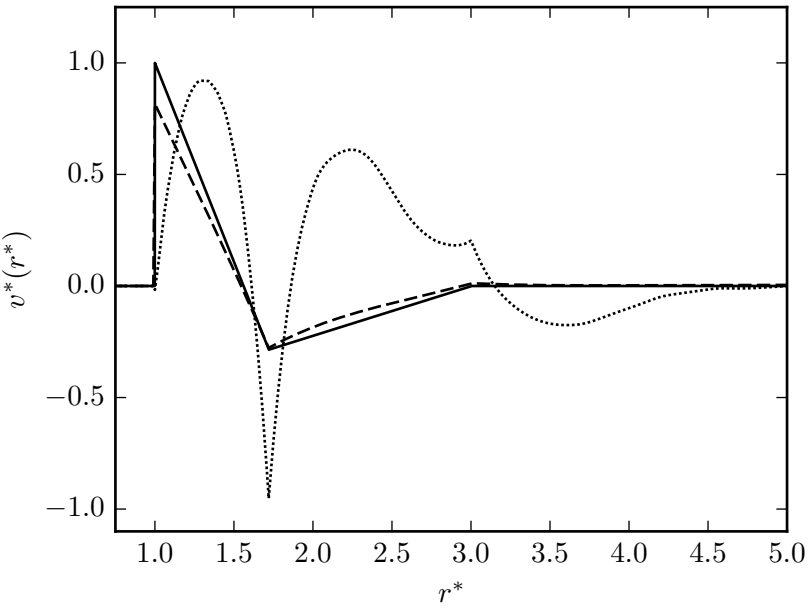

Figure 8.3.: The soft tail of the reduced Jagla potential $v_{\mathrm{J}}^* = v_{\mathrm{J}}/\epsilon$ as applied in this work (solid line), and the soft tails of the reduced optimized (for the test particle geometry) potentials $v_{\mathrm{opt}}^* = v_{\mathrm{opt}}/\epsilon$ for $(\eta, T^*) = (0.1, 1.0)$ (dashed line) and $(\eta, T^*) = (0.3, 0.1)$ (dotted line) as functions of the reduced center-to-center particle distance $r^* = r/\sigma$.

bation potential's behavior inside the hard core to adjust the optimized potential, gained in the test particle geometry, to the slit geometry. To this end, we fix the perturbation potential inside the core to a certain behavior, calculate the optimized potential behavior outside the hard core in the test particle geometry, and then apply the thus gained perturbation potential (hard core plus optimized soft tail) as interaction potential in a DFT code for the slit geometry. The latter we term optimized slit DFT. Subsequently, we compare the density profiles gained with the optimized slit DFT to those computed with a standard Metropolis [25] MC code for the slit. We studied constant, linear and quadratic functions as perturbation potential cores and found that the improvement of the linear function over the constant function was tremendous, whereas only little, if at all, accuracy was gained by shifting from linear to quadratic behavior. Hence, we calculate optimized potentials for a wide range of parameters of the linear function in the core using the just described technique, and afterwards determine for which parameter set the deviation between optimized slit DFT and MC density profiles is minimal. Since both the iteration to determine the optimized potential and the optimized slit DFT calculation are carried out quickly, thanks to fast-Fourier techniques, we refrain from applying a more elaborate minimization algorithm. As it turns out, also the choice of the parameter $a_{\max}$ (the optimized potential's range) is crucial in the minimization process and we had to reduce it to $3.08\,\sigma$ ($0.08\,\sigma$ to achieve a smooth transition of the potential to zero) in order to gain good compliance between optimized slit DFT and MC density distributions. Interestingly, $3\,\sigma$ is the range of the original Jagla potential.

In the following, we compare the optimized slit DFT density profiles to those obtained via MC simulations, perturbation DFT, and mean-field DFT in a slit with reduced length $l = 22$ at

different assorted state points (η, T^*). Here, l is chosen such that the bulk limit can be observed in the center of the slit to check for consistency.

At high temperatures and low densities, i.e. $(\eta, T^*) = (0.1, 1.0)$, we find the agreement between optimized slit DFT and MC results to be very good (see Fig. 8.4). Only at the first minimum

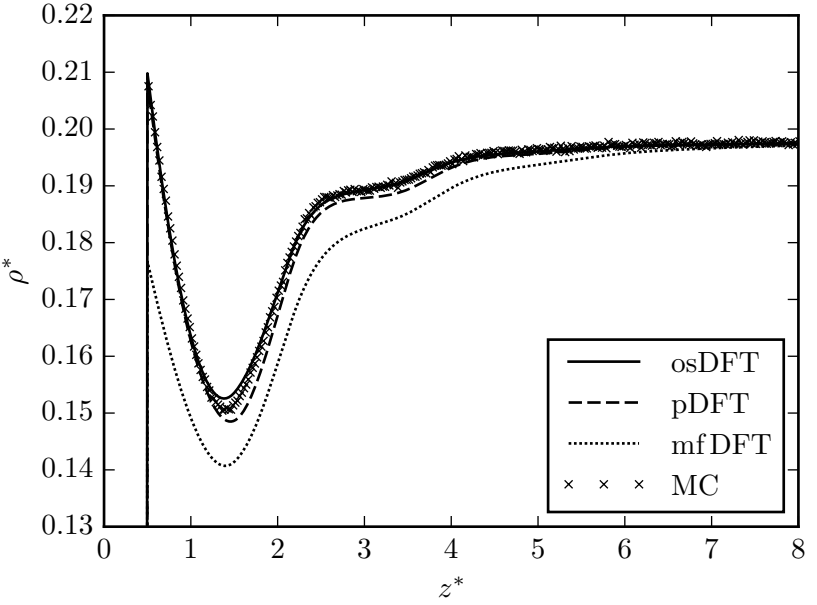

Figure 8.4.: The density distribution $\rho^* = \rho\sigma^3$ of the Jagla fluid in a slit with hard walls and reduced length $l = L/\sigma = 22$ at $(\eta, T^*) = (0.1, 1.0)$ described by means of the optimized slit DFT (solid line), perturbation DFT (dashed line), standard mean-field DFT (dotted line), and MC simulations (crosses). The abscissa provides the reduced distance $z^* = z/\sigma$ from the left wall.

away from the hard wall the optimized slit DFT profile is a

little off the MC data, but overall optimized slit DFT yields an improvement over the already good perturbation DFT result. As already discussed in Sec. 7.2, mean-field DFT fails to predict correct results in the vicinity of the hard wall.

If we move closer to the first biondal line of the Jagla fluid (see triangles in Fig. 8.10), by reducing the temperature at constant density, we find that at $(\eta, T^*) = (0.1, 0.5)$ the optimized slit DFT looses a bit of its accuracy but still produces result in good agreement with the corresponding MC data. This is depicted in Fig. 8.5. Again, the first minimum away from the hard wall is not reproduced correctly. Also, optimized slit DFT lies a little below the MC data between the first minimum and the bulk limit. However, compared to the perturbation DFT profile, which clearly lies below the MC profile, these are only minor shortcomings. Standard mean-field DFT fails and predicts a profile close to or in a gas phase. This is not surprising, since at the state point under consideration, the mean-field Jagla fluid is unstable (see solid line in Fig. 8.10).

At lower temperatures and higher densities, but not close to first or second binodal, which is the case at $(\eta, T^*) = (0.3, 0.3)$, the optimized slit DFT overall is in very good agreement with the MC results (see Fig. 8.6). This is remarkable since here perturbation DFT fails and exhibits unphysical oscillations. Mean-field DFT, being considered at a state point in its unstable region, erroneously predicts a gas phase.

By further reducing the temperature, i.e. $(\eta, T^*) = (0.3, 0.1)$, which also brings us closer to the second binodal, optimized slit DFT looses some of its accuracy and clearly shows deviations from the exact MC profile (see Fig. 8.7). However, the contact value seems still to be predicted well, and also the overall shape of the profile is in agreement with the MC results. Even though the density profile is not perfect, this is still a great improvement within

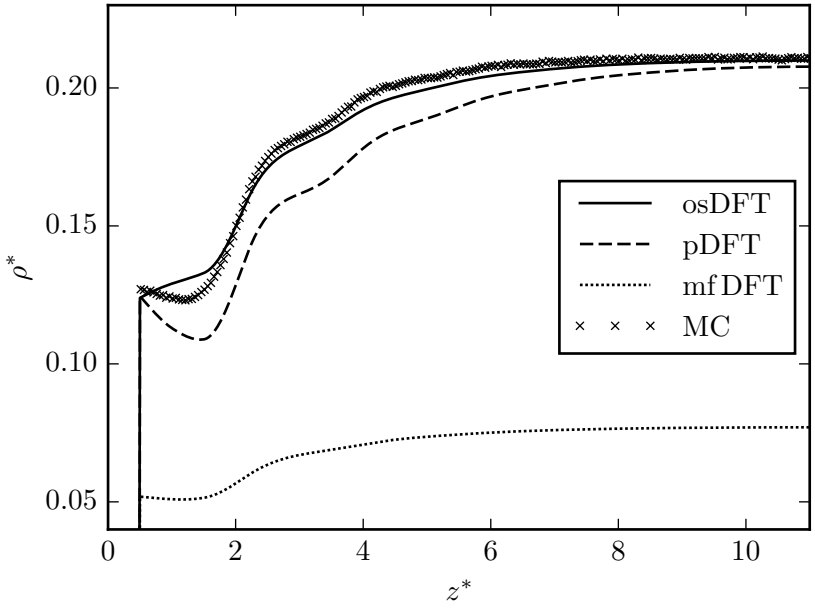

Figure 8.5.: The density distribution $\rho^* = \rho\sigma^3$ of the Jagla fluid in a slit with hard walls and reduced length $l = L/\sigma = 22$ at $(\eta, T^*) = (0.1, 0.5)$ described by means of the optimized slit DFT (solid line), perturbation DFT (dashed line), standard mean-field DFT (dotted line), and MC simulations (crosses). The abscissa provides the reduced distance $z^* = z/\sigma$ from the left wall.

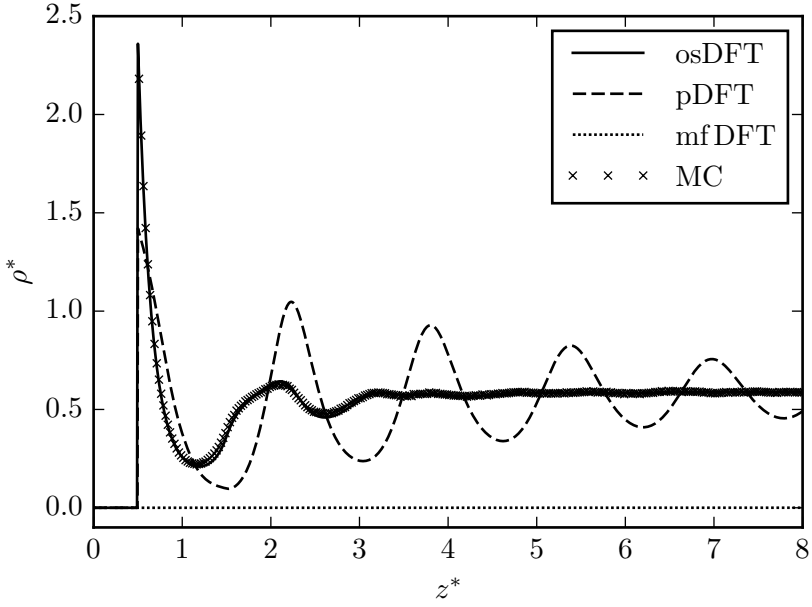

Figure 8.6.: The density distribution $\rho^* = \rho\sigma^3$ of the Jagla fluid in a slit with hard walls and reduced length $l = L/\sigma = 22$ at $(\eta, T^*) = (0.3, 0.3)$ described by means of the optimized slit DFT (solid line), perturbation DFT (dashed line), standard mean-field DFT (dotted line), and MC simulations (crosses). The abscissa provides the reduced distance $z^* = z/\sigma$ from the left wall.

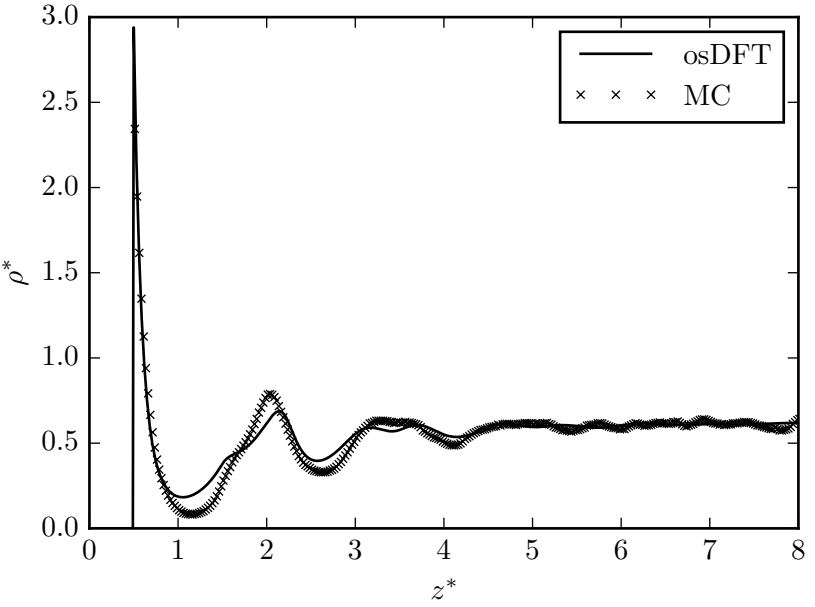

Figure 8.7.: The density distribution $\rho^* = \rho\sigma^3$ of the Jagla fluid in a slit with hard walls and reduced length $l = L/\sigma = 22$ at $(\eta, T^*) = (0.3, 0.1)$ described by means of the optimized slit DFT (solid line) and MC simulations (crosses). The abscissa provides the reduced distance $z^* = z/\sigma$ from the left wall.

DFT given that the perturbation DFT shows coarse artifacts in its density profile at higher temperature already. Perturbation DFT and mean-field DFT, being considered at a state point in the unstable regions of the corresponding bulk phase diagrams (see Fig. 8.10), fail to converge at $(\eta, T^*) = (0.3, 0.1)$.

Moving even closer to the second binodal line to the state point $(\eta, T^*) = (0.25, 0.1)$ by reducing the density increases the deviations between optimized slit DFT and MC results further. This is depicted in Fig. 8.8. Now, also the contact value is not predicted correctly anymore. Still, the optimized slit DFT results are in the range of the MC data while, at least roughly, resembling the shape of the quasi-exact density distribution. Perturbation DFT and mean-field DFT, again, fail to converge which is to expect given that the state point under consideration lies even deeper in the corresponding unstable regions (see Fig. 8.10).

As mentioned above, the MC results presented so far are calculated in a canonical simulation box in which, as the density is kept constant, no phase transition is possible. Hence, using canonical MC density profiles as input data for our optimized slit DFT at state points close to a binodal is questionable; especially since DFT is a theory formulated in the grand canonical ensemble. For this reason, we also fed the optimized slit DFT MC data we calculated by means of grand canonical MC simulations [27] for state points close to a binodal line, especially in the region $0.25 \leq \eta \leq 0.3$ at $T^* = 0.1$. However, when comparing grand canonical MC and corresponding optimized slit DFT density profiles, no improvement regarding the deviation of the latter from the former can be observed as against the canonical calculations. By this we mean that if we, for example, compare the mean square deviation between MC and optimized slit DFT profiles of a canonical calculation at $(\eta, T^*) = (0.25, 0.1)$ to the mean square deviation of a grand canonical calculation, which results in a bulk

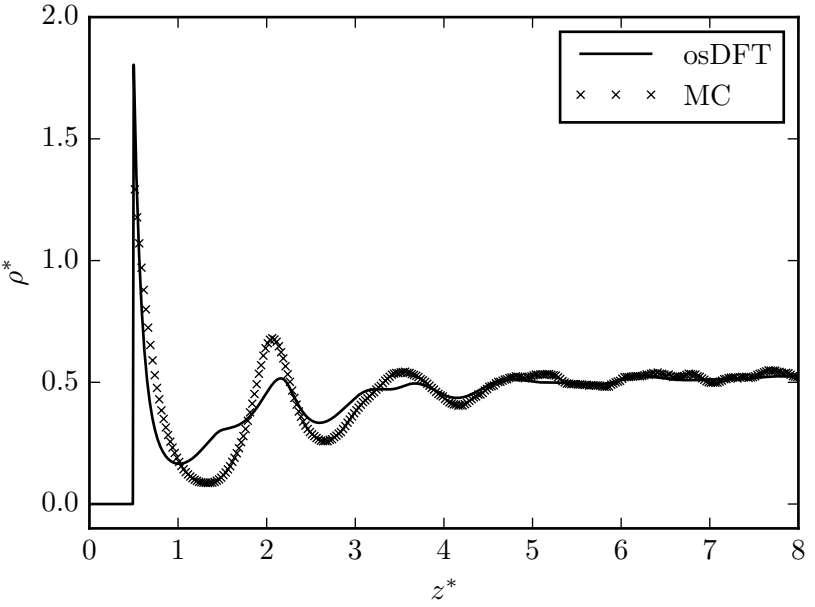

Figure 8.8.: The density distribution $\rho^* = \rho\sigma^3$ of the Jagla fluid in a slit with hard walls and reduced length $l = L/\sigma = 22$ at $(\eta, T^*) = (0.25, 0.1)$ described by means of the optimized slit DFT (solid line) and MC simulations (crosses). The abscissa provides the reduced distance $z^* = z/\sigma$ from the left wall.

density of $\eta = 0.263$ in the slit center at the same temperature, the two are of the same magnitude.

We also investigate the optimized slit DFT's performance regarding the variation of the slit length at state points where no phase transition due to a change of geometry is to expect. The calculations to calibrate the optimized slit DFT are all performed in a geometry with reduced slit length $l = 22$. If we gradually reduce the slit length down to $l = 6$, keeping the original optimized interaction potential, we find the agreement between optimized slit DFT and MC data to be only slightly poorer compared to the case with $l = 22$ for all state points checked. Figure 8.9 shows a comparison of optimized slit DFT and MC density distributions in slits with $l = 16$, $l = 11$ and $l = 6$ at $(\eta, T^*) = (0.3, 0.3)$. Note that an investigation of the optimized slit DFT's phase behavior due to a variation of the slit length follows below.

Furthermore, we note that the optimized slit DFT seems to be robust regarding small changes in the optimized perturbation potential. To acquire a continuous optimized perturbation potential $w_{\mathrm{opt}}(r; \eta, T^*)$, we perform curve fits, first in T^*-direction and subsequently in η-direction, through the optimized perturbation potentials for previously considered state points. This is done for the data gained using canonical MC. The fitted potential obviously deviates slightly from the original version; nevertheless, when plugged into the optimized slit DFT, the quality of the results remains the same. For the fit in T^*-direction we apply the function

$$w(r; T^*) = w_{\mathrm{J}}(r) + \sum_{i=0}^{5} w_i(r) \Big(T^*\Big)^{-i/8}, \tag{8.15}$$

where the functions $w_i(r)$ are the fit parameters and $w_{\mathrm{J}}(r)$ is the soft tail of the original Jagla potential. In particular, the fit in T^*-direction is done as follows. For a given packing fraction η, we have

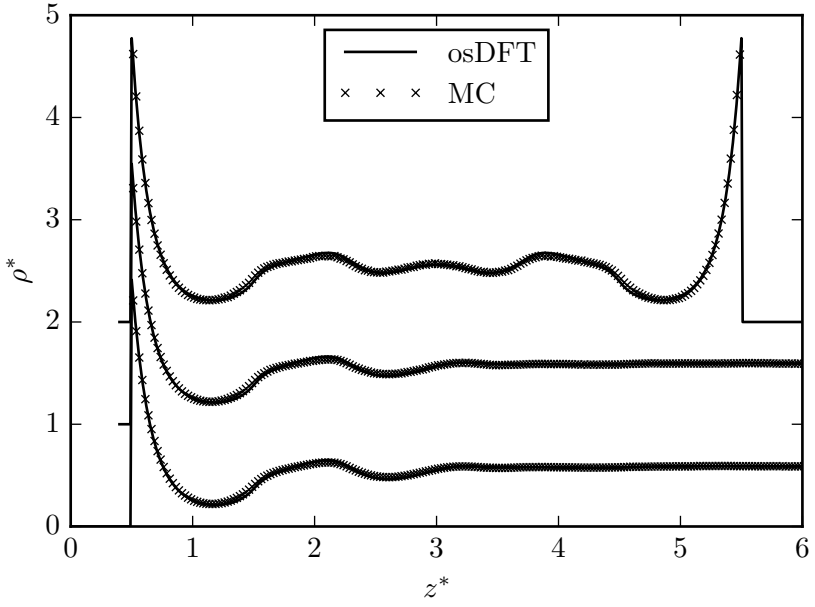

Figure 8.9.: The density distribution $\rho^* = \rho\sigma^3$ of the Jagla fluid in a slit with hard walls and reduced length $l = L/\sigma = 16$ (bottom), $l = 11$ (center), $l = 6$ (top) at $(\eta, T^*) = (0.3, 0.3)$ described by means of the optimized slit DFT (solid line) and MC simulations (crosses). For reasons of clarity, the center and the top line are shifted upwards by 1.0 and 2.0, respectively. The abscissa provides the reduced distance $z^* = z/\sigma$ from the left wall.

previously calculated optimized potential values w_{opt} available at $r = 0.00\,\sigma, 0.01\,\sigma, 0.02\,\sigma, \ldots, 3.08\,\sigma$ for various temperatures $T^* = 0.1, 0.2, \ldots, 1.0, 2.0, \ldots, 5.0$. Note, that $a_{\mathrm{max}} = 3.08\,\sigma$ is the range of the optimized potential. Now, for a fixed value of r, we fit the function in Eq. (8.15) to the values of w_{opt} at the various temperatures. This is repeated for every value of r which gives us the perturbation potential w_{opt} for every temperature in the interval $[0.1, 5.0]$ at the previously chosen packing fraction. This procedure is then repeated for the packing fractions $\eta = 0.001, 0.1, 0.15, 0.2, 0.25, 0.3$.

The subsequent fit in η-direction is done using the polynomial

$$w(r; T^*, \eta) = \sum_{i=0}^{3} u_i(r; T^*)\eta^i \tag{8.16}$$

with fit parameters $u_i(r; T^*)$. Here, for a fixed value of the tuple (r, T^*), we fit the function in Eq. (8.16) to the previously, through the fit in T^*-direction, determined values of w_{opt} at the packing fractions $\eta = 0.001, 0.1, 0.15, 0.2, 0.25, 0.3$. This is repeated for every tuple (r, T^*), where $r = 0.00\,\sigma, 0.01\,\sigma, 0.02\,\sigma, \ldots, 3.08\,\sigma$, as before, and $T^* = 0.08, 0.09, 0.1, \ldots, 5.0$. This finally yields the fitted optimized perturbation potential $w_{\mathrm{opt}}(r; \eta, T^*)$.

The obvious question now is, if the optimized slit DFT is able to describe the phase behavior of the Jagla fluid correctly. We first examine the bulk phase behavior of the canonical optimized slit DFT and for this purpose apply the fitted potential $w_{\mathrm{opt}}(r; \eta, T^*)$. We calculate the bulk binodal as described in Secs. 6.1.1 and 6.1.2, where we have to consider that the perturbation potential $w_{\mathrm{opt}}(r; \eta, T^*)$ is a function of the packing fraction η. Thus, the mean-field term of the bulk excess free energy density now reads:

$$\beta f_{\mathrm{mf}}^{\mathrm{ex}} = 2\pi\rho^2 \int_0^\infty \mathrm{d}r\, r^2 \beta w_{\mathrm{opt}}(r; \eta, T^*), \tag{8.17}$$

and the corresponding expressions for the excess chemical potential and the pressure are [c.f. Eqs. (6.26) and (6.27)]

$$\mu_{\mathrm{mf}}^{\mathrm{ex}} = 4\pi\rho I + 2\pi\rho^2 \frac{\partial I}{\partial \rho},$$

and

$$p_{\mathrm{mf}}^{\mathrm{ex}} = 2\pi\rho^2 I + 2\pi\rho^3 \frac{\partial I}{\partial \rho},$$

where the integral I now is the integral in Eq. (8.17). Note, that Eq. (8.17) is the bulk limit of the second term in Eq. (8.1) divided by the system's volume V. The resulting phase diagram of the canonical optimized slit DFT is plotted in Fig. 8.10 (plus symbols), and we find that it has little in common with the phase diagram of the Jagla fluid derived via MC simulations by Lomba and coworkers [24] (triangles). Not only does the optimized slit DFT binodal merely show one critical point instead of the expected two, also it is neither close to the first nor to the second MC binodal.

In an attempt to improve the bulk phase behavior of the optimized slit DFT, we, as described in Sec. 8.2.3, modify the potential core of the fitted perturbation potential $w_{\mathrm{opt}}(r;\eta,T^*)$ such that the canonical MC bulk pressure is recovered. The new potential, which we term $w_{\mathrm{opt}}^{\mathrm{p}}(r;\eta,T^*)$, now has the value of the well-chosen constant inside the core and is the unaltered fitted perturbation potential $w_{\mathrm{opt}}(r;\eta,T^*)$ outside the core. If we calculate the bulk phase diagram using the potential $w_{\mathrm{opt}}^{\mathrm{p}}(r;\eta,T^*)$, we find the two resulting binodals to be in good agreement with the MC binodals by Lomba and et al. (see Fig. 8.10, crosses). This implies that our method to improve the bulk pressure of the fluid also seems to improve its bulk phase behavior. However, if we plug the potential $w_{\mathrm{opt}}^{\mathrm{p}}(r;\eta,T^*)$ back into the slit DFT (this DFT we call pressure-optimized slit DFT), we can not recover the

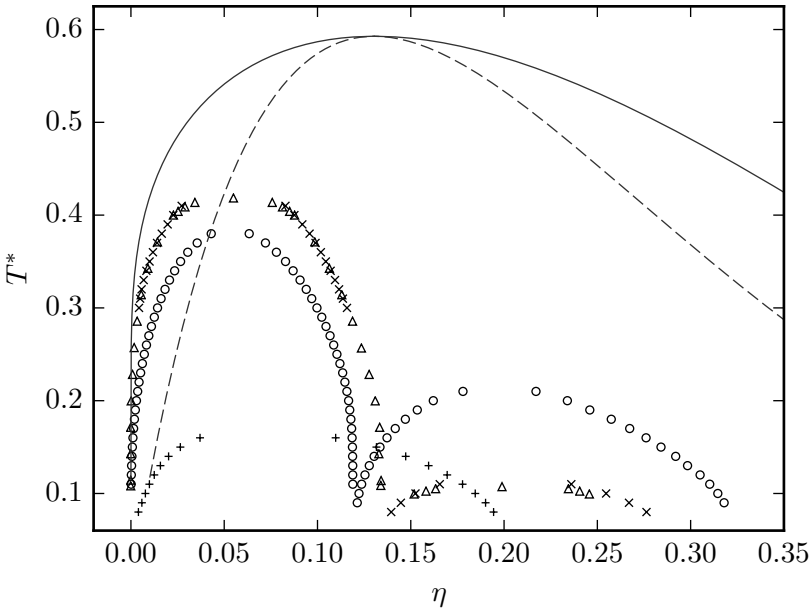

Figure 8.10.: The bulk binodal lines of the Jagla fluid in the T^*-η phase diagram obtained by means of mean-field perturbation theory with the optimized perturbation potential $w_{\mathrm{opt}}(r;\eta,T^*)$ (plus symbols), mean-field perturbation theory with the pressure-optimized perturbation potential $w^{\mathrm{p}}_{\mathrm{opt}}(r;\eta,T^*)$ (crosses), standard mean-field theory, i.e., mean-field theory with the soft tail of the Jagla potential as perturbation (solid line), first order perturbation theory of the twice split Jagla potential (circles, Sec. 6.4.2), and MC simulations [24] (triangles). The dashed line shows the standard mean-field bulk spinodal of the Jagla fluid.

density profiles of the optimized slit DFT. The density profiles of the pressure-optimized slit DFT are far off the corresponding MC density distributions and sometimes even show a gas phase at state points where the MC simulations predict a liquid.

Hence, we try to merge optimized slit DFT and pressure-optimized slit DFT results, by calculating a potential behavior inside the core which is as close as possible to the linear ramp of optimized slit DFT, under the constraint that the integral I_{core} [see Eq. (8.13)] takes the same value as in the pressure-optimized slit DFT. This is essentially a minimization under constraints in the function space on the interval $[0, \sigma]$, and we apply the method of Lagrange multipliers to solve it. If we term the new behavior of our optimized potential inside the core $w^{\mathrm{L}}_{\mathrm{opt}}(r; \eta, T^*)$, then the constraint of the minimization is given by

$$\begin{aligned}\int_0^\sigma \mathrm{d}r\, r^2 \beta w^{\mathrm{L}}_{\mathrm{opt}}(r; \eta, T^*) &\overset{\text{(Eq. (8.13))}}{=} I_{\mathrm{core}}(\eta, T^*) \\ &\overset{\text{(Eq. (8.14))}}{=} \beta c(\eta, T^*) \int_0^\sigma \mathrm{d}r\, r^2 \\ &= \frac{\sigma^3}{3} \beta c(\eta, T^*),\end{aligned}$$

whereas the expression to be minimized reads

$$\int_0^\sigma \mathrm{d}r \Big(\beta w^{\mathrm{L}}_{\mathrm{opt}}(r; \eta, T^*) - \beta w_{\mathrm{opt}}(r; \eta, T^*) \Big)^2 .$$

Thus, the corresponding Lagrangian function is the functional

$$\begin{aligned}\Lambda\Big[w^{\mathrm{L}}_{\mathrm{opt}}, \lambda\Big] = &\int_0^\sigma \mathrm{d}r \Big(\beta w^{\mathrm{L}}_{\mathrm{opt}}(r; \eta, T^*) - \beta w_{\mathrm{opt}}(r; \eta, T^*) \Big)^2 \\ &+ \lambda \left[\int_0^\sigma r^2 \beta w^{\mathrm{L}}_{\mathrm{opt}}(r; \eta, T^*)\, \mathrm{d}r - \frac{\sigma^3}{3} \beta c(\eta, T^*) \right],\end{aligned}$$

with the the Lagrange multiplier λ. We now demand

$$\frac{\delta\Lambda\Big[w_{\rm opt}^{\rm L},\lambda\Big]}{\delta w_{\rm opt}^{\rm L}} = 0, \tag{8.18}$$

and

$$\frac{\partial\Lambda\Big[w_{\rm opt}^{\rm L},\lambda\Big]}{\partial\lambda} = 0,$$

where the l.h.s. of Eq. (8.18) is a functional derivative, and obtain

$$w_{\rm opt}^{\rm L}(r;\eta,T^*) = w_{\rm opt}(r;\eta,T^*) - \frac{1}{2}\lambda\, r^2, \tag{8.19}$$

and

$$\lambda = -\frac{10}{3\,\sigma^2}c(\eta,T^*) + \frac{10}{\sigma^5}\int_0^\sigma {\rm d}r\, r^2 w_{\rm opt}(r;\eta,T^*).$$

On the interval $[0,\sigma]$, on which the minimization is carried out, the potential $w_{\rm opt}(r;\eta,T^*)$ is a linear function in r, and, hence, $w_{\rm opt}^{\rm L}(r;\eta,T^*)$ in Eq. (8.19) is quadratic in r, where $w_{\rm opt}^{\rm L}(r = 0;\eta,T^*) = w_{\rm opt}(r=0;\eta,T^*)$. This is depicted in Fig. 8.11 which shows a comparison of the perturbation potentials $w_{\rm opt}$, $w_{\rm opt}^{\rm p}$, $w_{\rm opt}^{\rm L}$, and the soft tail of the original Jagla potential $v_{\rm J}$ at the state point $(\eta,T^*) = (0.3,0.3)$. We observe that while the behavior of $w_{\rm opt}^{\rm L}$ inside the hard core is much closer to the behavior of $w_{\rm opt}$ than the behavior of $w_{\rm opt}^{\rm p}$, the deviation between $w_{\rm opt}^{\rm L}$ and $w_{\rm opt}$ inside the core is still rather large. If we calculate the bulk binodal line of the fluid with perturbation potential $w_{\rm opt}^{\rm L}$ inside the core and $w_{\rm opt}$ outside the core, we recover the binodal of the fluid with the perturbation potential $w_{\rm opt}^{\rm p}$ inside and $w_{\rm opt}$ outside the core. The density profiles in the slit calculated with the Lagrangian-optimized fluid ($w_{\rm opt}^{\rm L}$), however, show the same shortcomings as the previously determined density profiles of the

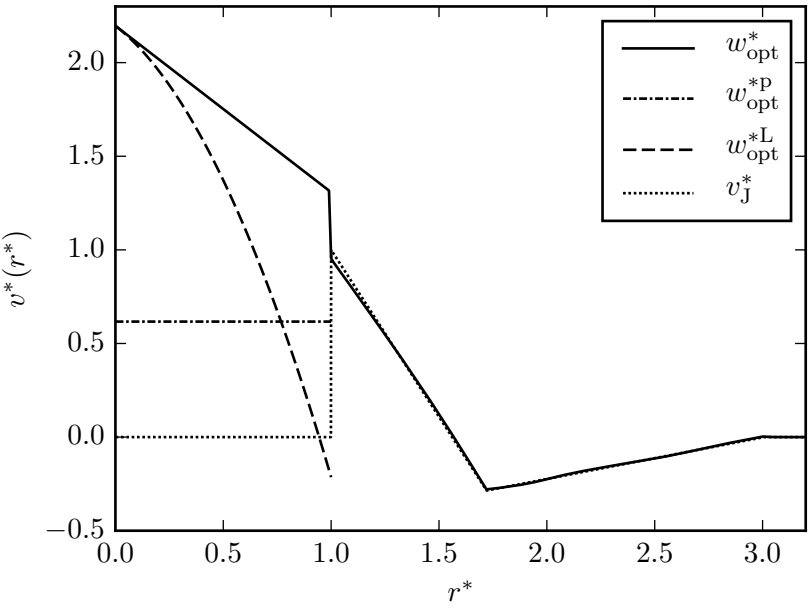

Figure 8.11.: The reduced perturbation potentials of the optimized slit DFT [$w^*_{\mathrm{opt}} = w_{\mathrm{opt}}/\epsilon$ (solid line)], the pressure-optimized slit DFT [$w^{*\mathrm{p}}_{\mathrm{opt}} = w^{\mathrm{p}}_{\mathrm{opt}}/\epsilon$ (dash-dotted line)], and the Lagrangian-optimized slit DFT [$w^{*\mathrm{L}}_{\mathrm{opt}} = w^{\mathrm{L}}_{\mathrm{opt}}/\epsilon$ (dashed line)] at $(\eta, T^*) = (0.3, 0.3)$. The dotted line shows the soft tail of the original reduced Jagla potential $v^*_{\mathrm{J}} = v_{\mathrm{J}}/\epsilon$. Since w^*_{opt}, $w^{*\mathrm{p}}_{\mathrm{opt}}$, and $w^{*\mathrm{L}}_{\mathrm{opt}}$ are equal for $r > \sigma$, only w^*_{opt} is plotted outside the hard core for reasons of clarity. The abscissa provides the reduced center-to-center particle distance $r^* = r/\sigma$.

pressure-optimized slit DFT ($w_{\mathrm{opt}}^{\mathrm{p}}$). Obviously, the deviation between the potentials $w_{\mathrm{opt}}^{\mathrm{L}}$ and w_{opt} inside the core is still too large to recover the results of the optimized slit DFT (w_{opt}) . While, as shown before, the latter seems stable to small changes in the optimized interaction potential, large changes in the behavior of $w_{\mathrm{opt}}(r;\eta,T^*)$ inside the hard core obviously destroy the resemblance of optimized slit DFT and MC density profiles.

The second investigation regarding the optimized slit DFT's phase behavior done in this work is focused on the slit geometry, and investigates if a phase transition inside the slit can be triggered by variation of the slit length. For this, we choose a state point in the stable region close to the high density liquid branch of the MC bulk liquid-liquid binodal (triangles in Fig. 8.10) and prepare a DFT slit system with corresponding reservoir. We then decrease the reduced slit length l step by step and perform two DFT calculations for each step; one with an initial density profile which has the liquid density of the state point under consideration and one with a gas initial density profile. We note that for all calculations with variable length l the optimized perturbation potential $w_{\mathrm{opt}}(r;\eta,T^*)$ calibrated for $l = 22$ is applied. In case of a phase transition due to the reduction of the slit length, the density inside the slit suddenly jumps to a lower density. Furthermore, if plotted as a function of the slit length $L = l\,\sigma$, the grand potential per area, given by $\Omega^* = -p\,L + 2\,\gamma$, where p is the pressure and γ the surface tension, exhibits a kink at the length where the two phases can coexist due to the change in pressure and surface tension. We do this investigation by deploying both canonically and grand-canonically calibrated optimized slit DFT, but cannot observe any phase transition. The density in the slit center is almost constant, also the grand potential per area shows

only one slope. Furthermore, these findings are independent of the chosen initial density.

This is in contrast to the grand canonical MC simulation results where a phase transition inside the slit can be observed in the density profiles as well as in the excess chemical potential $\mu_{\mathrm{mc}}^{\mathrm{ex}}$ due to the variation of the slit length. In Fig. 8.12, $\mu_{\mathrm{mc}}^{\mathrm{ex}}$ is plotted vs. the slit length l and we observe that the data is unsteady at $l_{\mathrm{co}} \approx 15$. This is the reduced slit length at which the two phases can coexist, and the jump in the data indicates a first-order phase transition. The MC simulations conducted to obtain the data in Fig. 8.12 all have the same initial density to achieve comparable results. In Fig. 8.13, a comparison of the corresponding grand canonical MC density profiles with grand-canonically optimized slit DFT density profiles is depicted for various slit lengths. Both figures show data at $T^* = 0.1$ and at a chemical potential μ which results in a density of $\rho^* \approx 0.493$, or $\eta \approx 0.256$, in the slit center of the slit with $l = 22$. The aim of Fig. 8.13 is to show the drop in density in the slit centers of the MC profiles, which can be observed especially in the region where $z^* > 4$. The upper family of MC profiles, oscillating roughly in the vicinity of $\rho^* = 0.45$, or $\eta \approx 0.24$, is the density distributions in the slits with length $l = 16, 18, 22$. Note that the state point at $\eta \approx 0.24$ and at $T^* = 0.1$ is in the vicinity of the high density liquid branch of the MC bulk liquid-liquid binodal (triangles [24] in Fig. 8.10). The lower family of MC profiles, oscillating roughly in the vicinity of $\rho^* = 0.35$, or $\eta \approx 0.18$, is the density distributions in the slits with length $l = 12, 14$. The state point at $\eta \approx 0.18$ and at $T^* = 0.1$ is in the vicinity of the low density liquid branch of the MC bulk liquid-liquid binodal. The discontinuity in the excess chemical potential $\mu_{\mathrm{mc}}^{\mathrm{ex}}(l)$ and the drop of density in the slit centers of the grand canonical MC simulations both occur at $l \approx 15$, indicating a first-order phase transition, which is triggered

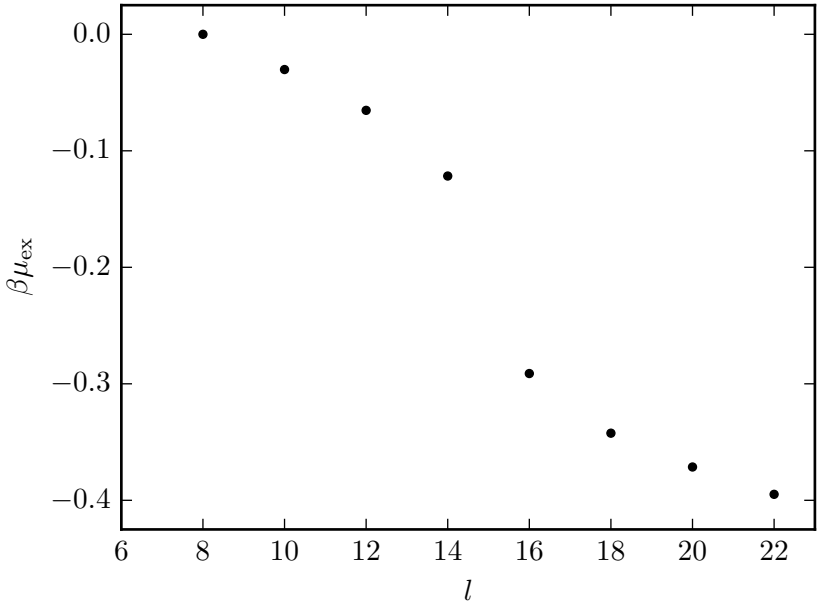

Figure 8.12.: The excess chemical potential of the grand canonical MC simulations as a function of the reduced slit length $l = L/\sigma$. The corresponding state point is at $T^* = 0.1$ and at a chemical potential μ which results in a density of $\rho^* \approx 0.493$, or $\eta \approx 0.256$, in the slit center of the slit with $l = 22$. The ordinate is scaled such that the excess chemical potential of the smallest slit length is zero.

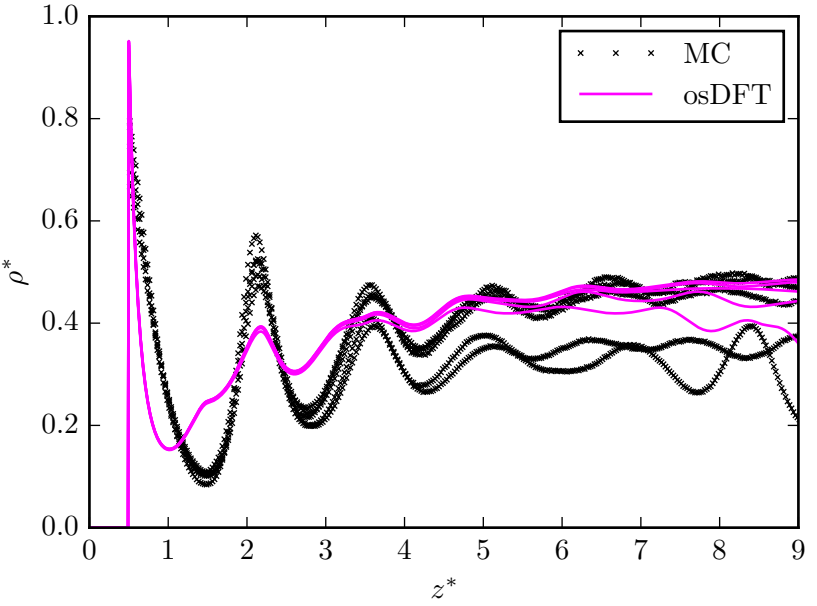

Figure 8.13.: (Color online.) The density distributions $\rho^* = \rho\sigma^3$ of the Jagla fluid in slits with hard wall and reduced length $l = L/\sigma = 12, 14, 16, 18, 22$ described by means of the optimized slit DFT, which is optimized using grand canonical MC data (solid lines) and grand canonical MC simulations (crosses). The corresponding state point is at $T^* = 0.1$ and at a chemical potential μ which results in a density of $\rho^* \approx 0.493$, or $\eta \approx 0.256$, in the slit center of the slit with $l = 22$. The abscissa provides the reduced distance $z^* = z/\sigma$ from the left wall. For reasons of clarity only the left parts of the profiles are plotted. We comment on the deviation between MC and DFT data in the text body.

due to the reduction of the slit length. The density profiles of the optimized slit DFT lack the sudden drop in density between $l = 14$ and $l = 16$; instead, the DFT density in the slit centers decreases merely slightly and continuously if the slit length is reduced. The degree of deviation between MC and optimized slit DFT density profiles for $l = 22$ is in the same range as in Fig. 8.8, which shows the canonical MC and the canonically-optimized slit DFT density profiles at $(\eta, T^*) = (0.25, 0.1)$, and is commented on in the corresponding paragraph in the text body. For completeness we note that, even though it does not produce correct density profiles, we also investigated the phase behavior of the pressure-optimized slit DFT ($w^{\mathrm{p}}_{\mathrm{opt}}$) inside the slit, and find the same negative result.

8.4. Conclusions and outlook

Obviously, the information the optimized slit DFT inherits from the MC density profiles in the calibration process discussed in Sec. 8.2.2 is enough to predict the density distribution inside the slit if no phase transition is to expect. The information about the latter, however, seems to be lost. The entire information from the MC calculations conducted to calibrate the optimized slit DFT is passed on via the optimized interaction potential w_{opt} with which the optimized weighted density $n_{\mathrm{opt}}(r) = \big(\rho * \beta w_{\mathrm{opt}}\big)(r)$ and the excess chemical potential $\beta\mu_{\mathrm{ex}}$ is determined. For a given state point (η, T^*), we determine one optimized perturbation potential for the reduced slit length $l = 22$. Hence, if we vary the slit length in the DFT calculation, the excess chemical potential is constant. This is in contrast to the grand canonical MC simulations where the excess chemical potential depends on the average particle number density inside the slit and, hence, changes if the slit length

is varied. Moreover, the excess chemical potential in the grand canonical MC simulations is an unsteady function of the reduced slit length l, if a phase transition inside the slit occurs due to the variation of l (see Fig. 8.12). Here, the jump occurs at the slit length where the two phases can coexist. Our optimized slit DFT misses this information which presumably is one reason for it does not describe the phase transition inside the confining slit. One could try to pass on the behavior of the grand canonical MC simulation excess chemical potential to the optimized slit DFT, but for this MC simulations with different reduced slit lengths l at the fixed state point of interest need to be conducted. If this is the case, it is more accurate to not only fix the behavior of DFT's chemical potential, but to do a full calibration for different slit lengths, i.e., to obtain an optimized perturbation potential $w_{\mathrm{opt}}(r;\eta,T^*,l)$ which is now additionally a function of the reduced slit length l. This has the benefit that also the optimized weighted density $n_{\mathrm{opt}}(r) = (\rho * \beta w_{\mathrm{opt}})(r)$ is adjusted to the variation of l. This, however, would make the optimized slit DFT redundant as it would not deliver information which is novel compared to the information already gained by the MC simulations conducted to calibrate it.

Part III.

Colloid-polymer mixture under confinement

9. A liquid-liquid critical point in a ternary colloid-polymer mixture

After the difficulties we encountered in Pt. II to describe the inhomogeneous Jagla fluid within the framework of DFT, we continue to use DFT to investigate the influence of the infinite slit confinement on the phase diagram, and in particular on the liquid-liquid binodal, of a simple model system for a colloid-polymer mixture. In colloid-polymer mixtures the colloidal particles are immersed in a solvent of polymer. Here, attraction between the colloids can be generated and adjusted based on the concentration, or density, of non-adsorbing polymer, and based on the size ratio R_c/R_g, where R_c is the radius of the colloidal sphere and R_g is the radius of gyration of the polymer. This attraction has its origin in the for the polymer excluded volume due to the presence of the colloidal particles. The excluded volume decreases if the colloids are packed more densely which in turn decreases the energy of the effective colloid-colloid interaction, and, thus, creates an effective attraction between the colloidal particles. This effective attraction may lead to gas-liquid separation [10], and even to liquid-liquid separation [15], of the colloidal particles. Here, by colloidal gas phase, a phase with a low colloid density is meant. Based on the findings of Ref. [15], in which the existence of a liquid-liquid critical point in a ternary mixture of monodisperse

colloidal spheres with two polydisperse or monodisperse polymer components is discussed, we set up a basic model system of a ternary colloid-polymer mixture which is comprised of monodisperse colloids and two monodisperse polymer species. We show that a bulk liquid-liquid critical point of the colloidal particles can arise in this simple system, and continue to study its behavior under the confinement of an infinitely large slit. To describe the particle interactions, we apply the Asakura-Oosawa-Vrij (AOV) model [2, 3, 39] for colloid-polymer mixtures in which the colloids are considered to be hard spheres, and in which the polymers exclusively interact with the colloid particles, but not with each other, via a hard-sphere interaction. Within the AOV model, the phase diagram of a colloid-polymer mixture of monodisperse colloids and monodisperse polymer is akin to the phase diagram of a simple fluid, where the polymer reservoir density corresponds to an inverse temperature. Furthermore, the phase behavior of the AOV model is similar to the one which follows from free volume theory, as has been shown in Ref. [36]. In free volume theory the excess free energy of the mixture is expressed as an expansion in the density of the polymer, or, more generally, in the density of the depletion agent, up to and including first order. This linearization is identical to the assumption of a vanishing interaction between the particles of the depletion agent. In the following, we deploy the framework of FMT (see Sec. 4.2) to express the free volume theory approach.

9.1. Bulk phase diagram

9.1.1. Theory

To investigate the ternary colloid-polymer mixture comprised of monodisperse colloids and two monodisperse polymer species, we

consider a system of N_c colloid particles which is coupled to two polymer particle reservoirs[1] and has the Volume V. One reservoir exclusively contains particles of polymer species No. 1 and possesses the chemical potential μ_1^r, where the superscript r stands for reservoir, and the other reservoir exclusively contains particles of polymer species No. 2 and possesses the chemical potential μ_2^r. I.e., we consider a semi-grand-canonical ensemble. Within the AOV model the particles are either considered to be hard spheres or to be ideal, and we refer to the hard-sphere radius of the colloids as R_c and to the hard-sphere radii of polymer species No. 1 and No. 2 as R_1 and R_2, respectively. The corresponding hard-sphere diameters we denote by σ with the associated index. The colloid particles interact with each other pairwise via the hard-sphere interaction potential

$$v_\mathrm{cc}(r) = \begin{cases} \infty & , r < 2\,R_\mathrm{c} \\ 0 & , \text{otherwise} \end{cases} \quad ,$$

where r denotes the center-to-center particle distance, and the pair interaction between a colloid particle and a polymer particle of species No. i ($i = 1, 2$) is described by the hard-sphere pair potential

$$v_{\mathrm{c}i}(r) = \begin{cases} \infty & , r < R_\mathrm{c} + R_i \\ 0 & , \text{otherwise} \end{cases} \quad .$$

The pair potentials of the possible polymer-polymer interactions, $v_{ii}(r)$ and $v_{12}(r) = v_{21}(r)$, all vanish which implies that the two reservoirs contain ideal particles.

[1] If the system is coupled to polymer reservoirs, the strength of the colloid-colloid interaction is solely dependent on the polymer reservoir densities and independent of the colloid density inside the system. This is crucial for interpreting the polymer reservoir density as an inverse temperature in the phase diagram.

In order to study the bulk phase behavior of the colloids immersed in the depletion agent of polymer, we continue to determine coexisting colloid phases. Two colloid phases, labeled I and II, can coexist if the chemical potentials of the colloids of both phases are equal and if the system pressures of both phases are equal [c.f. Eq. (6.21)]:

$$\begin{aligned} \mu_{\mathrm{c}}^{\mathrm{I}} &= \mu_{\mathrm{c}}^{\mathrm{II}} \\ p^{\mathrm{I}} &= p^{\mathrm{II}}. \end{aligned} \tag{9.1}$$

Thus, in the following, we determine the chemical potential μ_{c} of the colloids and the system pressure p. Our starting point is the Helmholtz free energy density $f = F/V$ of the system which for the mixture generally reads as:

$$f(\rho_{\mathrm{c}}, \rho_1, \rho_2) = f_{\mathrm{c}}^{\mathrm{id}}(\rho_{\mathrm{c}}) + f_1^{\mathrm{id}}(\rho_1) + f_2^{\mathrm{id}}(\rho_2) + f^{\mathrm{ex}}(\rho_{\mathrm{c}}, \rho_1, \rho_2). \tag{9.2}$$

Here, $f_{\mathrm{c}}^{\mathrm{id}}(\rho_{\mathrm{c}})$, $f_1^{\mathrm{id}}(\rho_1)$, and $f_2^{\mathrm{id}}(\rho_2)$ are the ideal gas contributions of the colloids, polymer species No. 1, and polymer species No. 2, respectively [see first equation in Eq. (6.25)], and $f^{\mathrm{ex}}(\rho_{\mathrm{c}}, \rho_1, \rho_2)$ is the excess part. The quantities ρ_{c}, ρ_1, and ρ_2 are the bulk number densities *inside* the system of the colloid particles, the particles of polymer species No. 1, and the particles of polymer species No. 2, respectively. Since we make use of the FMT approach to free volume theory, the excess contribution to the free energy density of the mixture is a function of the weighted densities n_α, $\beta f^{\mathrm{ex}}(\rho_{\mathrm{c}}, \rho_1, \rho_2) = \Phi(\{n_\alpha\})$ [c.f. Eq. (4.6)], where $\alpha = 0, 1, 2, 3$, as the vector weighted densities vanish in bulk (see Sec. 4.2). In the free volume theory, or AOV, ansatz $\Phi(\{n_\alpha\})$ is linearized [28] in the densities of the polymer around vanishing densities of all

polymer such that

$$\Phi^{\mathrm{AOV}}\Big(\big\{n_\alpha^{\mathrm{c}}, n_\alpha^{(1)}, n_\alpha^{(2)}\big\}\Big) = \Phi\Big(\big\{n_\alpha^{\mathrm{c}}\big\}\Big) + \sum_{\kappa=0}^{3} \frac{\partial\Phi\big(\{n_\alpha^{\mathrm{c}}\}\big)}{\partial n_\kappa^{\mathrm{c}}}\, n_\kappa^{(1)} + \sum_{\kappa=0}^{3} \frac{\partial\Phi\big(\{n_\alpha^{\mathrm{c}}\}\big)}{\partial n_\kappa^{\mathrm{c}}}\, n_\kappa^{(2)}. \tag{9.3}$$

Here, n_α^{c}, $n_\alpha^{(1)}$, and $n_\alpha^{(2)}$ are the weighted densities No. $\alpha = 0, 1, 2, 3$ of the colloids, polymer species No. 1, and No. 2, respectively [c.f. Eq. (4.7)], and $\Phi\big(\{n_\alpha^{\mathrm{c}}\}\big)$ is the hard-sphere free energy density of the pure colloid system without polymer. We now introduce the so-called free volume fraction ψ_i of polymer species No. i, the bulk FMT expression of which reads as

$$\psi_i = \exp\left(-\sum_{\kappa=0}^{3} \frac{\partial\Phi}{\partial n_\kappa^{\mathrm{c}}} \frac{n_\kappa^{(i)}}{\rho_i} \right) = \psi_i(\eta_{\mathrm{c}}), \tag{9.4}$$

and which is a function of the colloid bulk density ρ_{c}, or colloid packing fraction $\eta_{\mathrm{c}} = \pi\rho_c\sigma_c^3/6$, exclusively, due to the terms $n_\kappa^{(i)}/\rho_i$. The free volume fraction ψ_i can be interpreted as the Boltzmann factor of the reversible work required to insert a single particle of polymer species No. i into a pure bulk colloid system, i.e., [28]

$$\psi_i = \lim_{\rho_{1,2}\to 0} \exp(-\beta\mu_i^{\mathrm{ex}}). \tag{9.5}$$

For a vanishing colloid density ρ_{c}, the free volume fractions go to unity. This can easily be seen from (9.5). With the same we have

$$\lim_{\rho_{\mathrm{c}}\to 0} \psi_i = \lim_{\rho_{\mathrm{c}}\to 0} \lim_{\rho_{1,2}\to 0} \exp(-\beta\mu_i^{\mathrm{ex}}) = \exp(-\beta \lim_{\rho_{\mathrm{c}}\to 0} \lim_{\rho_{1,2}\to 0} \mu_i^{\mathrm{ex}}),$$

where the second equation holds since the exponential function is continuous, and $\lim_{\rho_c \to 0} \lim_{\rho_{1,2} \to 0} \mu_i^{\mathrm{ex}} = 0$ since the energy required to insert a particle of polymer species No. i into vacuum is zero. With this, we obtain

$$\lim_{\rho_c \to 0} \psi_i = 1.$$

By employing Eq. (9.4), we can rewrite the expression for Φ^{AOV} to be

$$\Phi^{\mathrm{AOV}}(\eta_c, \rho_1, \rho_2) = \Phi\Big(\{n_\alpha^c(\eta_c)\}\Big) - \rho_1 \ln\Big(\psi_1(\eta_c)\Big) - \rho_2 \ln\Big(\psi_2(\eta_c)\Big). \tag{9.6}$$

The expression for Φ^{AOV} in Eq. (9.6) as well as the ideal gas contributions of the polymer in Eq. (9.2) contain the system polymer densities ρ_1 and ρ_2. However, since we assume a system which is coupled to two polymer particle reservoirs, we can not control the polymer system densities ρ_i, but only the polymer reservoir densities ρ_i^r. Hence, we make use of the fact that in the AOV model the polymer-polymer interactions are neglected and express ρ_i in terms of ρ_i^r. Polymer reservoir No. i contains an ideal gas of particles of polymer species No. i and has the chemical potential $\beta\mu_i^r = \ln(\Lambda^3 \rho_i^r)$. The chemical potential μ_i of polymer species No. i inside the system is given by [see Eq. (6.19)]

$$\begin{aligned} \beta\mu_i = \frac{\partial \beta f}{\partial \rho_i} &= \ln(\Lambda^3 \rho_i) + \frac{\partial \Phi^{\mathrm{AOV}}}{\partial \rho_i} \\ &= \ln(\Lambda^3 \rho_i) - \ln\big(\psi_i(\eta_c)\big). \end{aligned} \tag{9.7}$$

Since we assume particle reservoirs and system to be in thermodynamic equilibrium, $\mu_i = \mu_i^r$ must hold from which we obtain

$$\rho_i = \psi_i \, \rho_i^r. \tag{9.8}$$

Now, we can rewrite the free energy density f of the system, as well as all functions we obtain from f, as functions of ρ_c (or η_c), ρ_1^r, and ρ_2^r, which are all variables we can control. Thus, we continue to calculate the chemical potential μ_c of the colloids inside the system and the system pressure p. The former is given by

$$\begin{aligned}\beta\mu_\mathrm{c} &= \frac{\partial\beta f(\rho_\mathrm{c},\rho_1,\rho_2)}{\partial\rho_\mathrm{c}} \\ &= \ln\left(\Lambda^3\rho_\mathrm{c}\right) + \frac{\partial\Phi^\mathrm{AOV}}{\partial\rho_\mathrm{c}} \\ &= \ln\left(\Lambda^3\rho_\mathrm{c}\right) + \frac{\partial\Phi}{\partial\rho_\mathrm{c}} - \rho_1\frac{\partial\ln\left(\psi_1(\eta_\mathrm{c})\right)}{\partial\rho_\mathrm{c}} - \rho_2\frac{\partial\ln\left(\psi_2(\eta_\mathrm{c})\right)}{\partial\rho_\mathrm{c}},\end{aligned} \tag{9.9}$$

where we have used the expression in Eq. (9.6) for Φ^AOV. The first two terms in the last equality of Eq. (9.9) we recognize to be the chemical potential $\beta\mu_\mathrm{c}^\circ$ of the pure, or unperturbed, colloid system. By using the relation between the polymer system densities ρ_i and the polymer reservoir densities ρ_i^r in Eq. (9.8), we can rewrite[2]

[2] With (9.8) and the definition of $\beta\mu_\mathrm{c}^\circ$ we rewrite the expression in the last line of Eq. (9.9) to be

$$\beta\mu_\mathrm{c} = \beta\mu_\mathrm{c}^\circ - \psi_1\rho_1^\mathrm{r}\frac{\partial\ln\left(\psi_1(\eta_\mathrm{c})\right)}{\partial\rho_\mathrm{c}} - \psi_2\rho_2^\mathrm{r}\frac{\partial\ln\left(\psi_2(\eta_\mathrm{c})\right)}{\partial\rho_\mathrm{c}}.$$

Now, we make use of the fact that $\frac{\partial\ln(\psi_i)}{\partial\rho_\mathrm{c}} = \frac{1}{\psi_i}\frac{\partial\psi_i}{\partial\rho_\mathrm{c}}$ and obtain

$$\beta\mu_\mathrm{c} = \beta\mu_\mathrm{c}^\circ - \rho_1^\mathrm{r}\frac{\partial\psi_1}{\partial\rho_\mathrm{c}} - \rho_2^\mathrm{r}\frac{\partial\psi_2}{\partial\rho_\mathrm{c}}.$$

In the last step, we substitute the partial derivatives via

$$\frac{\partial\psi_i}{\partial\rho_\mathrm{c}} = \frac{\partial\psi_i}{\partial\eta_\mathrm{c}}\frac{\partial\eta_\mathrm{c}}{\partial\rho_\mathrm{c}} = \frac{\partial\psi_i}{\partial\eta_\mathrm{c}}\frac{\pi}{6}\sigma_\mathrm{c}^3,$$

μ_c as a function of η_c, η_1^r, and η_2^r, where $\eta_i^r = \pi\rho_i^r\sigma_i^3/6$ are the polymer reservoir packing fractions:

$$\beta\mu_c = \beta\mu_c^\circ - \frac{\eta_1^r}{q_1^3}\frac{\partial\psi_1}{\partial\eta_c} - \frac{\eta_2^r}{q_2^3}\frac{\partial\psi_2}{\partial\eta_c}. \tag{9.10}$$

Here, we have introduced the diameter ratios $q_i = \sigma_i/\sigma_c$. In analogy to Eq. (6.20), the pressure of the three-component colloid-polymer system is given by

$$p = -f + \rho_c\mu_c + \rho_1\mu_1 + \rho_2\mu_2$$

which, with the expressions in Eqs. (9.2) and (9.6), becomes

$$\begin{aligned}\beta p = &-\beta(f_c^{id} + f_1^{id} + f_2^{id}) \\ &- \Phi(\{n_\alpha^c\}) + \rho_1 \ln\left(\psi_1(\eta_c)\right) + \rho_2 \ln\left(\psi_2(\eta_c)\right) \\ &+ \beta(\rho_c\mu_c + \rho_1\mu_1 + \rho_2\mu_2).\end{aligned} \tag{9.11}$$

This can be simplified, and by using Eq. (9.8) one obtains (see App. D.1)

$$\beta p = \beta p_c^\circ + \rho_1^r\left[\psi_1 - \eta_c\frac{\partial\psi_1}{\partial\eta_c}\right] + \rho_2^r\left[\psi_2 - \eta_c\frac{\partial\psi_2}{\partial\eta_c}\right], \tag{9.12}$$

where we have introduced the pressure of the unperturbed system,

$$\beta p_c^\circ = \rho_c - \Phi + \rho_c\frac{\partial\Phi}{\partial\rho_c}.$$

We now restrict ourselves to the special case in which the reservoir packing fraction of polymer species No. 1 is a multiple of the reservoir packing fraction of polymer species No. 2, i.e.,

$$\eta_1^r = a\,\eta_2^r, \tag{9.13}$$

and introduce the diameter ratio $q_i = \sigma_i/\sigma_c$ to obtain the expression in (9.10).

where $a \geq 0$. This reduces the number of independant parameters from three, namely η_c, η_1^r, and η_2^r, to two, namely η_c and η_2^r, and, thus, a state point of the system is now given by $(\eta_\mathrm{c}, \eta_2^\mathrm{r})$. With this, the system of equations one has to solve to determine coexisting colloid phases, Eq. (9.1), becomes

$$\begin{aligned} \mu_\mathrm{c}(\eta_\mathrm{c}^\mathrm{I}, \eta_2^\mathrm{r}) &= \mu_\mathrm{c}(\eta_\mathrm{c}^\mathrm{II}, \eta_2^\mathrm{r}) \\ p(\eta_\mathrm{c}^\mathrm{I}, \eta_2^\mathrm{r}) &= p(\eta_\mathrm{c}^\mathrm{II}, \eta_2^\mathrm{r}), \end{aligned}$$

for a fixed value of η_2^r. Since the attraction between the colloids is caused by the presence of the polymer and must vanish for vanishing polymer densities, phase separation is to be expected for η_2^r greater than a critical polymer reservoir density $\eta_{2,\,\mathrm{crit}}^\mathrm{r}$, and the polymer density η_2^r can be interpreted as an inverse temperature. The critical point $(\eta_{\mathrm{c},\,\mathrm{crit}}, \eta_{2,\,\mathrm{crit}}^\mathrm{r})$ can be determined by solving the system of equations

$$\frac{\partial p(\eta_\mathrm{c}, \eta_2^\mathrm{r})}{\partial \eta_\mathrm{c}} = 0, \qquad \frac{\partial^2 p(\eta_\mathrm{c}, \eta_2^\mathrm{r})}{\partial \eta_\mathrm{c}^2} = 0$$

for η_c and η_2^r [c.f. Eq. (6.23)], and by solving

$$\frac{\partial p(\eta_\mathrm{c}, \eta_2^\mathrm{r})}{\partial \eta_\mathrm{c}} = 0$$

for η_2^r, we obtain the spinodal as a function $\eta_2^\mathrm{r}(\eta_\mathrm{c})$ [c.f. Eq. (6.22)].

9.1.2. Results

To study gas-liquid and liquid-liquid phase separation of the colloid particles in the ternary colloid-polymer mixture described in Sec. 9.1.1, we adjust the remaining parameters as follows. The diameter ratios $q_i = \sigma_i/\sigma_\mathrm{c}$ we set to $q_1 = 0.25$ and $q_2 = 1.5$, and the parameter a in Eq. (9.13), which determines η_1^r depending on

the free parameter η_2^{r}, we set to $a = 0.6$. For the hard-sphere free energy density $\Phi(\{n_\alpha\})$ of the pure colloid system, we deploy the White Bear version of FMT mark II (see Sec. 4.2), since it provides highly accurate results for thermodynamic quantities and, furthermore, satisfies the SPT differential equation, $\partial\Phi^{\mathrm{WBII}}/\partial n_3 = \beta p$ in bulk, the derivational term of which appears in the free volume fractions ψ_i [Eq. (9.4)].

Figure 9.1 shows the thus obtained pressure curves as functions of the colloid packing fraction η_{c} for various values of the polymer reservoir packing fraction η_2^{r}. We observe van der Waals loops in the regions $0.02 \lesssim \eta_{\mathrm{c}} \lesssim 0.14$ and $0.25 \lesssim \eta_{\mathrm{c}} \lesssim 0.46$ which diminish and finally vanish as η_2^{r} decreases. These indicate that gas-liquid and liquid-liquid phase separation of the colloid particles can occur in the given system. The dash-dotted line shows the pressure at the liquid-liquid critical polymer packing fraction $\eta_{2,\mathrm{LL}}^{\mathrm{r}} \approx 0.5548$, and we observe a saddle point at $\eta_{\mathrm{c,LL}} \approx 0.3625$. Likewise, at the gas-liquid critical polymer packing fraction $\eta_{2,\mathrm{GL}}^{\mathrm{r}} \approx 0.5510$, the pressure curve (dash-dot-dotted line) has a saddle point at $\eta_{\mathrm{c,GL}} \approx 0.0779$. For vanishing η_{c}, the pressure does not go to zero but approaches a positive limit which is caused by the two remaining polymer species in the system. In the given configuration the reduced pressure is given by

$$\frac{\beta p \sigma_{\mathrm{c}}^3}{\eta_2^{\mathrm{r}}} = \frac{\beta p_c^\circ \sigma_{\mathrm{c}}^3}{\eta_2^{\mathrm{r}}} + \frac{6\,a}{\pi\, q_1^3}\left[\psi_1 - \eta_{\mathrm{c}}\frac{\partial\psi_1}{\partial\eta_{\mathrm{c}}}\right] + \frac{6}{\pi\, q_2^3}\left[\psi_2 - \eta_{\mathrm{c}}\frac{\partial\psi_2}{\partial\eta_{\mathrm{c}}}\right].$$

In the limit $\eta_{\mathrm{c}} \to 0$, the pure colloid pressure p_c° vanishes, as does the second term in each bracket, and the free volume fractions ψ_i go to unity. With this, we obtain

$$\lim_{\rho_{\mathrm{c}}\to 0} \frac{\beta p \sigma_{\mathrm{c}}^3}{\eta_2^{\mathrm{r}}} = \frac{6}{\pi}\left(\frac{a}{q_1^3} + \frac{1}{q_2^3}\right) \approx 73.904\,.$$

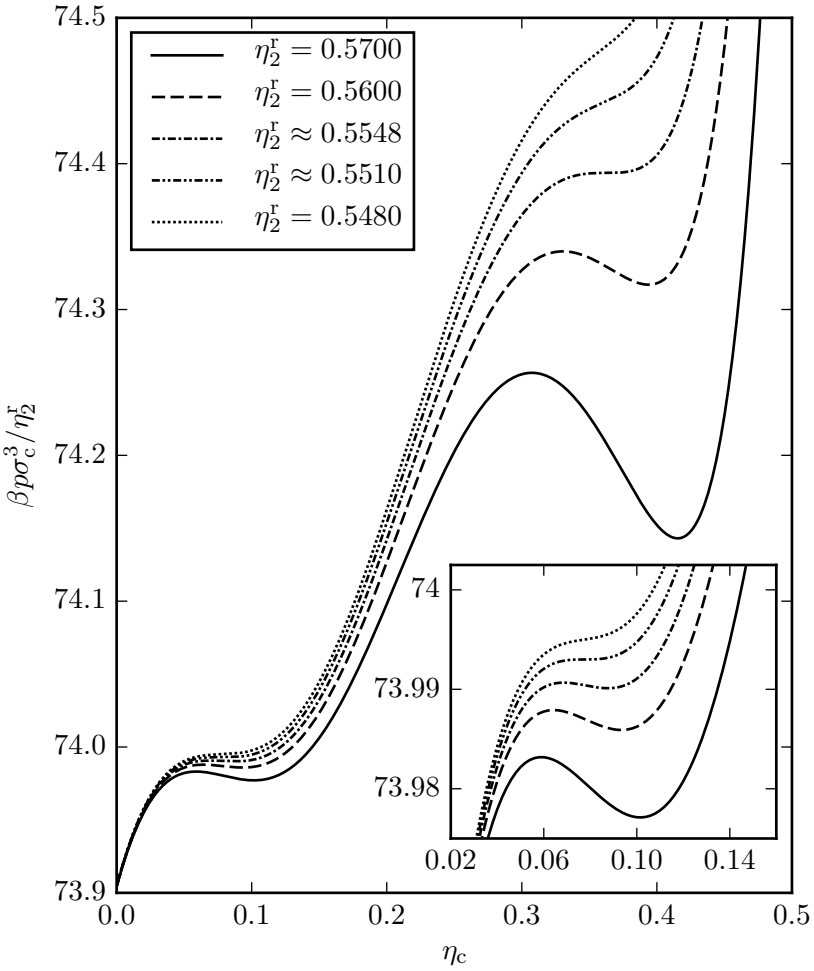

Figure 9.1.: The reduced bulk pressure $\beta p \sigma_c^3 / \eta_2^r$ of the ternary colloid-polymer mixture as a function of the colloid packing fraction η_c for various values of the polymer reservoir packing fraction η_2^r. The dash-dotted and the dash-dot-dotted lines show the pressure at the liquid-liquid critical polymer packing fraction $\eta_{2,LL}^r \approx 0.5548$ and the gas-liquid critical polymer packing fraction $\eta_{2,GL}^r \approx 0.5510$, respectively. For reasons of clarity, the inset shows the pressure for small values of η_c in greater detail.

Our pressure data, plotted in Fig. 9.2, attains the same (correct) low density limit.

We continue to calculate the corresponding phase diagram. This yields the results presented in Fig. 9.2. As is to be expected from the previously analyzed pressure curves, we find a spinodal of the colloid-colloid interaction (dashed line) which has two critical points (full dots). Furthermore, we obtain a binodal which has three different branches. One for $\eta_2^{\mathrm{r}} \gtrsim 0.6$ indicating a transition from colloid gas to high-density colloid liquid (dotted line), one which denotes a transition from colloid gas to low-density colloid liquid (dash-dotted line), and one that marks a transition from low-density colloid liquid to high-density colloid liquid (dash-dot-dotted line). The critical point of the gas-low-density-liquid coexistence is located at $(\eta_{\mathrm{c,GL}}, \eta_{2,\mathrm{GL}}^{\mathrm{r}}) \approx (0.0779, 0.5510)$, and the critical point of the liquid-liquid coexistence at $(\eta_{\mathrm{c,LL}}, \eta_{2,\mathrm{LL}}^{\mathrm{r}}) \approx (0.3625, 0.5548)$.

9.2. Phase diagram of the inhomogeneous mixture

9.2.1. Theory

The next step of our analysis is the investigation of the inhomogeneous phase diagram of the ternary colloid-polymer mixture, the bulk properties of which are discussed in Sec. 9.1. For this, we examine the colloid-polymer mixture when confined in an infinite slit with hard walls by means of classical DFT; this implies that we now consider a grand-canonical ensemble. The infinite slit geometry is introduced in Sec. 7.2. As discussed at the beginning of this chapter, the presence of the polymer generates an effective attraction between the hard-sphere colloids; likewise, an effective

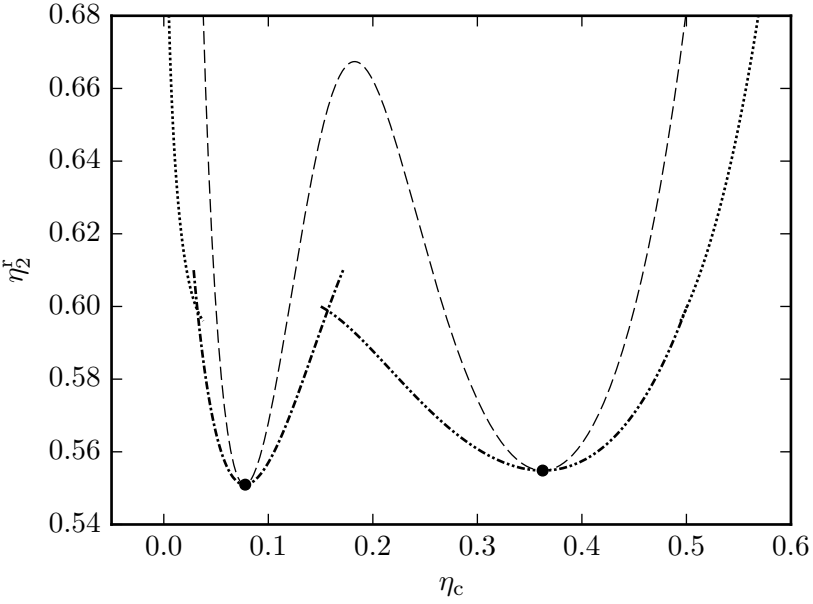

Figure 9.2.: The bulk phase diagram of the colloid-colloid interaction in the ternary colloid-polymer mixture. The ordinate provides the reservoir packing fraction η_2^r of polymer species No. 2, where the reservoir packing fraction η_1^r of colloid species No. 1 is adjusted to $\eta_1^r = 0.6\,\eta_2^r$. On the abscissa, the colloid packing fraction η_c is plotted. The dashed line depicts the spinodal of the colloid-colloid interaction, and the associated binodal exhibits three branches. These indicate possible phase transitions from gas to high-density liquid (dotted line), from gas to low-density liquid (dash-dotted line), and from low-density liquid to high-density liquid (dash-dot-dotted line). The critical points of the gas-low-density-liquid binodal and the liquid-liquid binodal are marked by the full dots.

interaction potential, which is dependent on polymer concentration and size ratios, is generated between the colloids and the hard walls of the slit, making the latter effectively attractive to the colloids. In the inhomogeneous system, the equilibrium particle densities of the colloids and the two polymer species, $\rho_c(\mathbf{r})$, $\rho_1(\mathbf{r})$, and $\rho_2(\mathbf{r})$, are functions of the position $\mathbf{r}$ inside the system, and the functional of the grand potential of the ternary colloid-polymer mixture in the AOV model reads as follows (c.f. Sec. 4.1):

$$\begin{aligned}\Omega[\rho_c(\mathbf{r}),\rho_1(\mathbf{r}),\rho_2(\mathbf{r})] = k_B T \sum_{j=c,1,2} \int \mathrm{d}\mathbf{r}\, \rho_j(\mathbf{r}) \Big[\ln\left[\Lambda_j^3 \rho_j(\mathbf{r})\right] - 1 \Big] \\ + k_B T \int \mathrm{d}\mathbf{r}\, \Phi^{\mathrm{AOV}} \Big(\{ n_\alpha^c, n_\alpha^{(1)}, n_\alpha^{(2)} \} \Big) \\ + \sum_{j=c,1,2} \int \mathrm{d}\mathbf{r}\, \rho_j(\mathbf{r}) [V_{\mathrm{ext},j}(\mathbf{r}) - \mu_j] .\end{aligned} \tag{9.14}$$

Here, the first term is the sum over the ideal gas contributions of the three particle species to the functional of the intrinsic Helmholtz free energy, and the second term is the excess contribution $\mathcal{F}^{\mathrm{ex}}$. The expression for Φ^{AOV} is the same as in Eq. (9.3), only now also the vector weighted densities $\mathbf{n}_{v1}(\mathbf{r})$ and $\mathbf{n}_{v2}(\mathbf{r})$ have to be taken into account, such that $\alpha, \kappa = 0, 1, 2, 3, v1, v2$. The external potentials of the slit geometry read as follows:

$$V_{\mathrm{ext},j}(z) = \begin{cases} 0 & , R_j \le z \le L - R_j \\ \infty & , \text{otherwise} \end{cases} ,$$

where L is the wall separation distance, and z denotes the distance form the left wall. Since the bulk system discussed in Sec. 9.1 constitutes the particle reservoir of the inhomogeneous system, the

chemical potentials μ_j are given by the expressions in Eqs. (9.10) and (9.7), respectively. The equilibrium density profiles $\rho_j(\mathbf{r})$ can be obtained by solving the minimization conditions

$$\frac{\delta\Omega}{\delta\rho_j(\mathbf{r})} = 0, \qquad j = \mathrm{c}, 1, 2, \tag{9.15}$$

through, e.g., a Piccard iteration. Insertion of the results of (9.15) into Eq. (9.14) yields the grand potential Ω of the system.

In the inhomogeneous case, a colloid phase is characterized by the tuple $(\bar{\eta_\mathrm{c}}, \eta_2^\mathrm{r})$. Here, $\bar{\eta_\mathrm{c}}$ is the mean packing fraction of the colloids inside the system, i.e.,

$$\bar{\eta_\mathrm{c}} = \frac{4\pi}{3} R_\mathrm{c}^3 \left[\frac{1}{L - 2R_\mathrm{c}} \int_{R_\mathrm{c}}^{L-R_\mathrm{c}} \mathrm{d}z\, \rho_\mathrm{c}(z) \right], \tag{9.16}$$

where the term in brackts is the mean colloid density[3] inside the system. Thus, for a given polymer reservoir density η_2^r, two colloid phases, $(\bar{\eta}_\mathrm{c}^\mathrm{I}, \eta_2^\mathrm{r})$ and $(\bar{\eta}_\mathrm{c}^\mathrm{II}, \eta_2^\mathrm{r})$, can coexist if the grand potentials and chemical potentials of both phases are equal, i.e., if

$$\begin{aligned} \mu_\mathrm{c}(\bar{\eta}_\mathrm{c}^\mathrm{I}, \eta_2^\mathrm{r}) &= \mu_\mathrm{c}(\bar{\eta}_\mathrm{c}^\mathrm{II}, \eta_2^\mathrm{r}), \\ \Omega(\bar{\eta}_\mathrm{c}^\mathrm{I}, \eta_2^\mathrm{r}) &= \Omega(\bar{\eta}_\mathrm{c}^\mathrm{II}, \eta_2^\mathrm{r}) \end{aligned} \tag{9.17}$$

holds. In bulk, $\Omega = -pV$, and thus we recover (9.1) from the bulk limit of Eq. (9.17).

9.2.2. Results and outlook

To determine colloid phases which can coexist in the infinite slit geometry, we proceed as follows. In so doing, we are guided by

[3] In the exprssion for the mean colloid density of the system, the volume of the system is defined to be the volume accessible to the hard-sphere centers of the colloid particles.

the bulk phase diagram of the ternary colloid-polymer mixture (Fig. 9.2). For a given reservoir packing fraction η_2^{r} and slit length L, we determine the grand potential Ω and the equilibrium density profiles $\rho_1(z)$, $\rho_2(z)$, and $\rho_{\mathrm{c}}(z)$ of the system for various values of the colloid reservoir packing fraction η_{c}. Here, we treat the gas-low-density-liquid and the liquid-liquid binodal separately, and orient ourselves by the width of the corresponding bulk binodal at the chosen value of η_2^{r} to find an appropriate range of the values of η_{c}. Via Eq. (9.10), we calculate the corresponding chemical potentials $\mu_{\mathrm{c}}(\eta_{\mathrm{c}})$ of the colloids and thus gain data points of the function $\Omega(\mu_{\mathrm{c}})$. This procedure is repeated twice for every value of η_{c} with different initial colloid packing fractions $\eta_{\mathrm{c}}^{\mathrm{init}}$ for the minimizing iteration; one lies notably below η_{c} and the other notably above. In case of a possible phase coexistence inside the slit, the data $\Omega(\mu_{\mathrm{c}})$ show two different intersecting branches, one corresponding to a low-density phase and one corresponding to a high-density phase. Obviously, at the intersection $(\mu_{\mathrm{c}}^{\mathrm{co}}, \Omega^{\mathrm{co}})$ the chemical potentials of the colloids of both phases and the grand potentials of both phases are equal and thus the intersection marks the phase coexistence [c.f. Eq. (9.17)]. Figure 9.3 shows a plot of the $\Omega(\mu_{\mathrm{c}})$ data corresponding to the liquid-liquid binodal at $\eta_2^{\mathrm{r}} = 0.585$ for a slit with length $L = 10.0\, R_{\mathrm{c}}$. Via the inverse of Eq. (9.10), we determine the reservoir colloid packing fraction $\eta_{\mathrm{c}}(\mu_{\mathrm{c}}^{\mathrm{co}})$ corresponding to the phase coexistence. While the value $\mu_{\mathrm{c}}^{\mathrm{co}}$ is unique, $\eta_{\mathrm{c}}(\mu_{\mathrm{c}}^{\mathrm{co}})$ is not necessarily, and there may be one, two, or three results. In the latter case, one corresponds to an unstable phase and can be discarded. The curve $\mu_{\mathrm{c}}(\eta_{\mathrm{c}})$ corresponding to the liquid-liquid binodal at $\eta_2^{\mathrm{r}} = 0.585$ is shown in Fig. 9.4. The dashed line marks $\mu_{\mathrm{c}}^{\mathrm{co}}$ and the three intersections with the curve $\mu_{\mathrm{c}}(\eta_{\mathrm{c}})$ (solid line) are the three possible values for $\eta_{\mathrm{c}}(\mu_{\mathrm{c}}^{\mathrm{co}})$. The one located at $\eta_{\mathrm{c}} \approx 0.4$ corresponds to an physically unstable phase, since here the function $\mu_{\mathrm{c}}(\eta_{\mathrm{c}})$ has a negative slope. For each

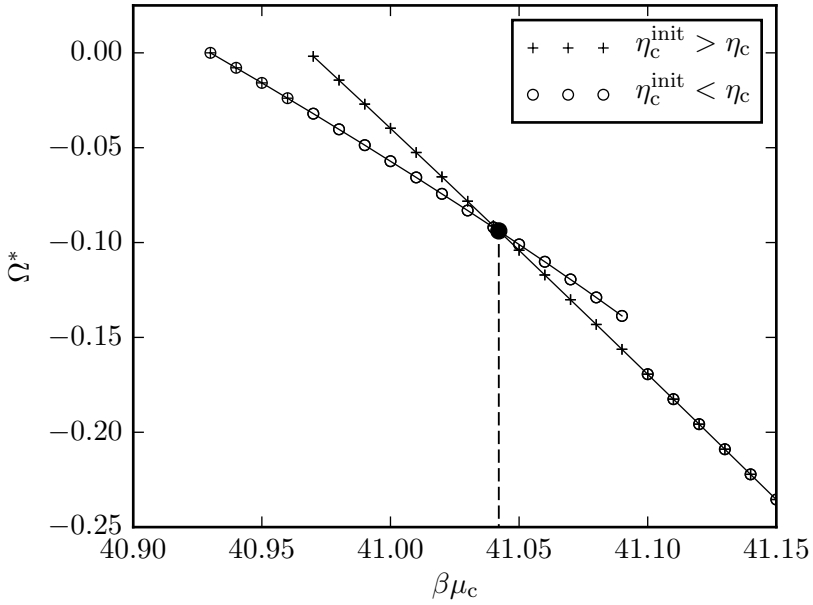

Figure 9.3.: The reduced grand potential $\Omega^* = \beta\Omega R_c^2/A$ of the ternary colloid-polymer mixture confined inside an infinite slit with length $L = 10\,R_c$ as a function of the chemical potential $\beta\mu_c$ of the colloids. Here A denotes the area of the confining walls. The polymer reservoir packing fraction η_2^r is adjusted to 0.585, and each data point (plus symbol or circle) is the result of one DFT calculation. The range of $\beta\mu_c$ on the abscissa corresponds to a range of η_c from approximately 0.13 to 0.48 (see Fig. 9.4), and the plus symbols show the results of the calculations for which the initial colloid packing fraction η_c^{init} was set to 0.55, whereas the circles show results for $\eta_c^{init} = 0.02$. We observe two different branches of solutions which are interpolated (thin solid lines) to determine the intersection (full dot). The latter marks the phase coexistence, as here the grand potentials and the chemical potentials of the two branches are equal [see Eq. (9.17)]. The vertical dashed line marks the chemical potential $\beta\mu_c^{co}$ at which the two branches intersect. From the corresponding density profiles (two of these, which represent the coexisting phases, are plotted in Fig. 9.5), we can identify the steeper branch (more negative slope) with the high-density liquid phase and the branch which is less steep (less negative slope) with the low-density liquid phase. The results have been adjusted in the direction of the ordinate such that the greatest value of the grand potential in the data is zero.

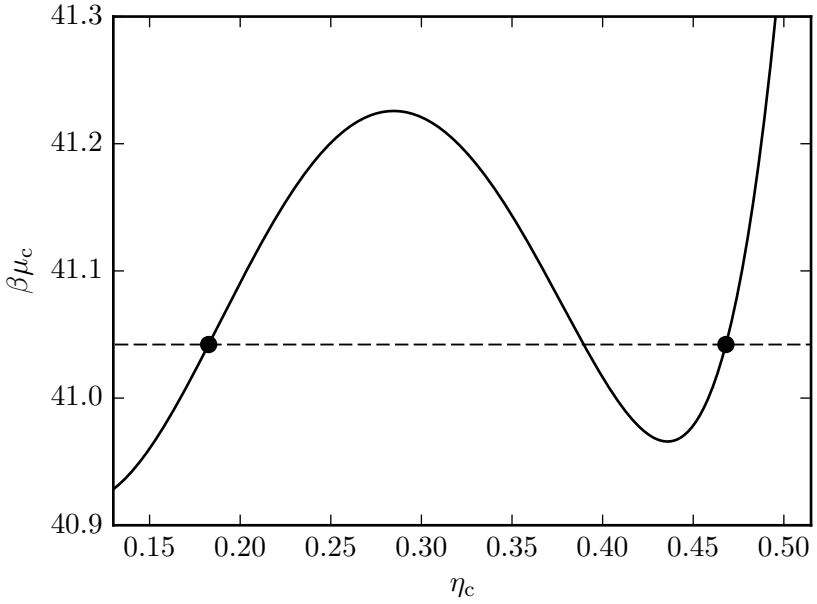

Figure 9.4.: The chemical potential $\beta\mu_c$ of the colloids as a function of the colloid reservoir packing fraction η_c (solid line) at a polymer reservoir packing fraction $\eta_2^r = 0.585$. The curve shows the van der Waals loop corresponding to the liquid-liquid binodal, and the horizontal dashed line marks the chemical potential at which the low-density liquid and the high-density liquid phase can coexist (c.f. Fig. 9.3). The full dots mark the physically meaningful colloid reservoir packing fractions $\eta_c(\mu_c^{co})$ which correspond to the phase coexistence.

of the values $\eta_c(\mu_c^{co})$ which are not associated with an unstable phase, two more DFT minimizations are carried out, one with initial colloid packing fraction $\eta_c^{init} < \eta_c(\mu_c^{co})$ and one with $\eta_c^{init} > \eta_c(\mu_c^{co})$. This yields two distinct results which we label I and II. While the grand potentials of these are, of course, equal, i.e., $\Omega^I = \Omega^{II}$, the density profiles differ. One is the colloid one-particle density $\rho_c^I(z)$ of the low-density phase and the other the colloid one-particle density $\rho_c^{II}(z)$ of the high-density phase. An example is given in Fig. 9.5, where the density profiles of the two liquid phases which can coexist at $\eta_2^r = 0.585$ in a slit with length $L = 10\,R_c$ are plotted. The two colloid mean packing fractions corresponding to the phase coexistence, $\bar{\eta}_c^I$ and $\bar{\eta}_c^{II}$, are obtained from the one-particle densities $\rho_c^I(z)$ and $\rho_c^{II}(z)$ via Eq. (9.16).

If for various values of η_2^r the colloid mean packing fractions $\bar{\eta}_c^I(\eta_2^r)$ and $\bar{\eta}_c^{II}(\eta_2^r)$ of the coexisting phases are plotted in an η_2^r-$\bar{\eta}_c$-graph, a phase diagram of the colloid-colloid interaction in the infinite slit is obtained. Figure 9.6 shows the binodals of the inhomogeneous system for various reduced slit lengths $l = L/R_c$ (symbols), where the solid lines connecting the symbols are merely intended to guide the eye and are of no physical meaning. The dashed as well as the dash-dotted and dash-dot-dotted gray lines are the bulk spinodal and binodals depicted in Fig. 9.2, respectively. In bulk, the mean colloid packing fraction $\bar{\eta}_c$ inside the system is equal to the colloid reservoir packing fraction η_c, and, hence, the bulk data is plotted on the same scale on the abscissa as the results for the inhomogeneous system. In an infinitely long slit, i.e., $l \to \infty$, the influence of the walls on the mean colloid packing fraction inside the system vanishes, and we obtain the corresponding coexisting phases via DFT calculations in a system without walls (a bulk system). The respective results are plotted as crosses in Fig. 9.6 and are in very good agreement

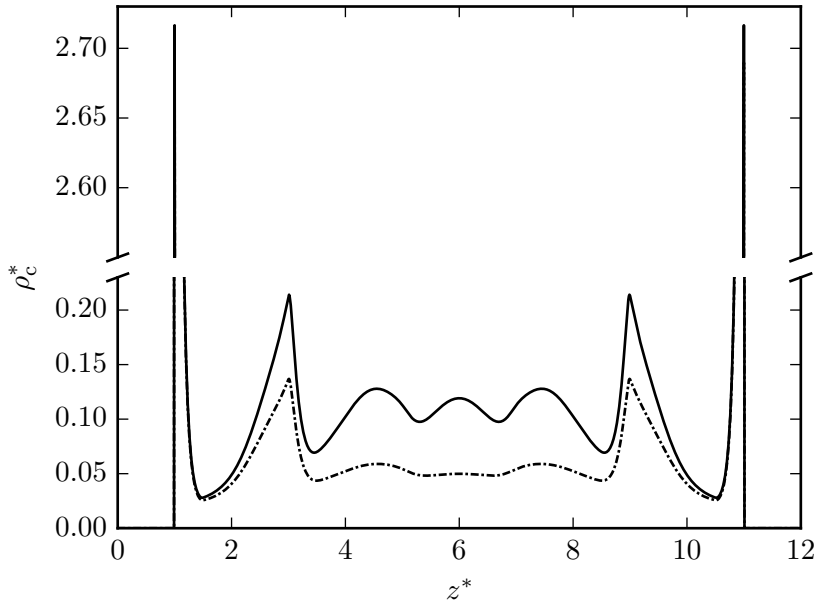

Figure 9.5.: The colloid density distributions in the slit, $\rho_c^* = \rho_c R_c^3$, of the low-density liquid phase (dash-dotted line) and the high-density liquid phase (solid line) which can coexist at a polymer reservoir packing fraction $\eta_2^r = 0.585$. The slit length L is $10\,R_c$, and the abscissa provides the reduced distance $z^* = z/R_c$ from the left wall. Since the hard walls are effectively attractive to the colloid particles, the density close to the walls is notably high.

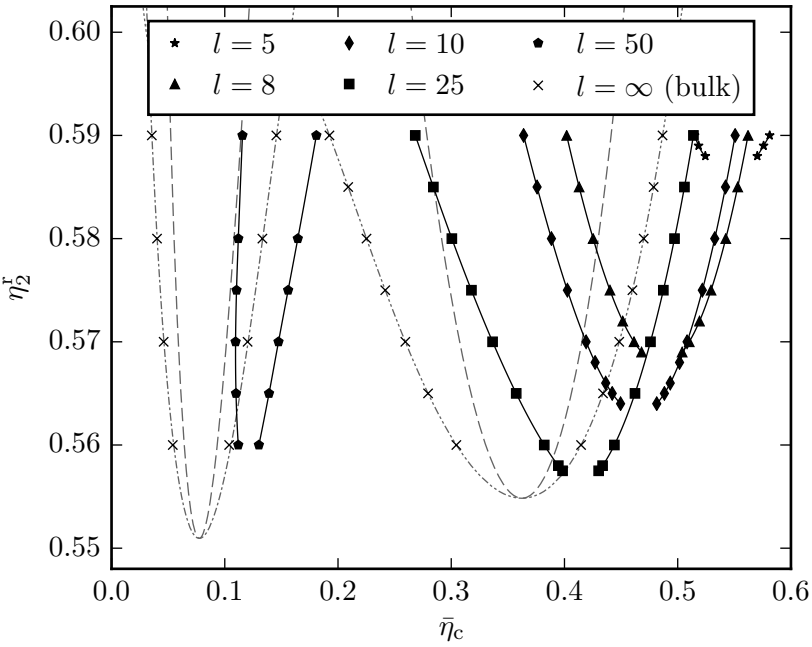

Figure 9.6.: The phase diagram of the colloid-colloid interaction in the ternary colloid-polymer mixture if confined by the infinite slit geometry for various values of the reduced slit length $l = L/R_{\mathrm{c}}$ (symbols). The black solid lines are intended to guide the eye and are of no physical meaning. The ordinate provides the reservoir packing fraction η_2^{r} of polymer species No. 2, where the reservoir packing fraction η_1^{r} of colloid species No. 1 is adjusted to $\eta_1^{\mathrm{r}} = 0.6\,\eta_2^{\mathrm{r}}$. On the abscissa, the mean colloid packing fraction inside the slit, $\bar{\eta_{\mathrm{c}}}$, is plotted. The non-solid gray lines are the bulk spinodal (dashed line) and binodals (dash-dotted and dash-dot-dotted line) discussed in Sec. 9.1.2 and depicted in Fig. 9.2. In bulk $\bar{\eta_{\mathrm{c}}} = \eta_{\mathrm{c}}$, and, hence, bulk and inhomogeneous data are plotted on the same scale on the abscissa.

with the bulk data discussed in Sec. 9.1.2 (non-solid gray lines in Fig. 9.6).

If the slit length L is reduced, the liquid-liquid binodal (depicted by the squares, diamonds, triangles, and stars in Fig. 9.6) is shifted to higher mean colloid packing fractions and becomes more narrow, i.e., the density jump of the corresponding liquid-liquid phase transition at a given value of η_2^{r} becomes smaller. Furthermore, the liquid-liquid critical point (not shown explicitly in our data, but its position can be roughly estimated) is shifted towards higher polymer reservoir packing fractions η_2^{r}. These effects become the more prominent, the smaller L becomes, and the effect on the liquid-liquid binodal by reducing l from 8 (triangles) to 5 (stars) is tremendous. We observe the same qualitative behavior of the gas-low-density-liquid binodal under confinement (pentagons), however, the effect of the confining walls seems to be stronger here, as the changes in shape and position by going from $l = \infty$ to $l = 50$ are more pronounced than the changes of the liquid-liquid binodal if l is reduced from ∞ to 25. Furthermore, we note that our data of the gas-low-density-liquid binodal for $l = 50$ (pentagons) exhibits (weak) reentrant phase behavior of the gas branch, since the data points at $\eta_2^{\mathrm{r}} = 0.575$, $\eta_2^{\mathrm{r}} = 0.57$, and $\eta_2^{\mathrm{r}} = 0.565$ lie at a lower mean colloid packing fractions $\bar{\eta}_{\mathrm{c}}$ than the points at $\eta_2^{\mathrm{r}} = 0.56$ and $\eta_2^{\mathrm{r}} = 0.58$. However, the effect is weak and only supported by three data points so that we can not rule out the possibility that we observe a numerical artifact.

The phase behavior of the colloid-polymer mixture inside the slit we observe in our results is in agreement with the findings by Evans [12] that the nature of the phase transition in a capillary is determined by the location of the capillary critical point; the location of which differs from the location of the bulk critical point, as can be observed in our results in Fig. 9.6. The smaller the wall separation distance L becomes, the more the critical

point is shifted towards higher mean colloid packing fractions $\bar{\eta_c}$ and towards higher polymer reservoir packing fractions η_2^r, making the critical point dependent on L: $(\eta_{c,\,crit}(L), \eta_{2,\,crit}^r(L))$. Reference [12] finds that the phase transition in the capillary is of first order at temperatures below the capillary critical temperature $T_{crit}(L)$ and of higher order, i.e., continuous, for temperatures above the capillary critical temperature. In the case of the colloid-polymer mixture within the AOV model, this translates to the fact that phase transitions which occur in the capillary are first-order if the polymer reservoir packing fraction η_2^r lies above the critical capillary polymer reservoir packing fraction $\eta_{2,\,crit}^r(L)$, whereas phase transitions in the capillary are continuous if $\eta_2^r < \eta_{2,\,crit}^r(L)$. This is confirmed by our results. For fixed $\eta_2^r > \eta_{2,\,crit}^r(L)$, we find the typical two branches in the data $\Omega(\mu_c)$ (see Fig. 9.3) as well as a density jump in the corresponding density profiles. This is characteristic of a first-order phase transition. For fixed $\eta_2^r < \eta_{2,\,crit}^r(L)$, only one branch in $\Omega(\mu_c)$ is observed which changes its slope continuously. The corresponding density profiles change continuously, too. This is the characteristic of a higher-order phase transition. When compared to the results by Schmidt et al. [35], who study the phase diagram of a binary colloid-polymer mixture with diameter ratio $q = \sigma_p/\sigma_c = 1$ in an infinite slit with hard walls, it appears that the two biondals of our ternary colloid-polymer mixture are more sensitive regarding the decrease of the density jump between coexisting densities at fixed η_2^r upon reduction of the slit length L.

Possible future work on the subject could be the investigation of how modification of the colloid-wall interaction alters the behavior of the gas-low-density-liquid and liquid-liquid binodal under confinement, as well as a more thorough investigation of the possible reentrant phase behavior of the gas-low-density-liquid binodal under confinement.

Part IV.

Conclusion and additional remarks

10. Conclusions and outlook

The primary aim of this dissertation was the construction of a DFT capable of describing the phase behavior and, especially, the liquid-liquid phase transition of the Jagla fluid under confinement. Here, the motivation was that a successful description of the inhomogeneous Jagla fluid might be a first small step towards the finding of an experimental setting which stabilizes the presumed liquid-liquid critical point of water.

To achieve this goal, two approaches were pursued. First, we constructed a perturbation DFT based on a first-order perturbation description of the homogeneous Jagla fluid in which the Jagla interaction potential was separated twice into reference and perturbation parts. While this perturbation DFT outperformed standard mean-field DFT and produced results in good agreement with MC data at state points not too close to the binodals, it failed at low temperatures in the vicinity of the bulk liquid-liquid critical temperature. In the second approach, we employed MC simulation data of the Jagla bulk fluid to compute an optimized interaction potential which, if applied in standard mean-field DFT, is supposed to recover the quasi-exact MC results of the inhomogeneous fluid. This optimized DFT delivered results more accurate than the results of our perturbation DFT, and at state points not too close to the binodals the agreement between optimized DFT and MC simulation density profiles was excellent. Even at temperatures in the vicinity of the bulk liquid-liquid critical temperature the density profiles of the optimized DFT

were in the same range as the MC simulation profiles. Despite these positive findings, it turned out that our optimized DFT is not capable of describing phase transitions inside the infinite slit geometry, and, hence, is not suited to compute the phase diagram or the inhomogeneous Jagla fluid.

Future approaches towards a DFT for the Jagla fluid could be the one derived by Tschopp et al. [38] who present their 'Barker-Henderson density functional' to describe classical inhomogeneous fluids; or a DFT based on the ansatz of Santos et al. [34, 19] who approximate the soft tails of hard-core interaction potentials by piecewise constant functions.

Finally, we succeeded in computing the gas-liquid and the liquid-liquid binodal of a ternary colloid-polymer mixture confined by a slit with infinitely extended hard walls using DFT. Here, the Asakura-Oosawa-Vrij model was applied in which the particle interactions are either ideal or hard-sphere-like; the effective attraction between the colloid particles required to observe phenomena like phase separation is solely caused by the presence of the polymer. Since merely hard-sphere interactions had to be treated, we could fall back on FMT which is a DFT that accurately describes hard-sphere mixtures. This spared us of treating the soft tail of an effective interaction potential in a perturbative manner. It might be interesting to extract the effective interaction potential between two colloid particles in the mixture and examine if the liquid-liquid critical point of the colloid-colloid interaction can be recovered by using perturbation theory. In so doing, the colloid-polymer mixture would be treated as a simple one-component fluid in which the (colloid) particles solely interact via the effective interaction potential.

A. Remarks on Chapter 3

A.1. Integration of the n-particle density

With Eq. (3.5) we have

$$\int \rho^{(n)}(\mathbf{r}^n)\mathrm{d}\mathbf{r}^n = \frac{1}{\Xi}\sum_{N=n}^{\infty}\frac{z^N}{(N-n)!}\int \exp(-\beta V_N)\mathrm{d}\mathbf{r}^N$$
$$\overset{(2.6)}{=} \frac{1}{\Xi}\sum_{N=n}^{\infty}\frac{z^N}{(N-n)!}\,Z_N.$$

Now, we plug in a factor of one of the form $N!/N!$, and find

$$\int \rho^{(n)}(\mathbf{r}^n)\mathrm{d}\mathbf{r}^n \overset{(3.3)}{=} \sum_{N=n}^{\infty}\frac{N!}{(N-n)!}\,p(N)$$
$$\overset{(3.2)}{=} \left\langle \frac{N!}{(N-n)!} \right\rangle.$$

Note that the sum in the first equality starts from $N = n$, and not from $N = 0$ as in Eq. (3.2), which is due to the fact that here an ensemble of systems with $N \geq n$ is considered, since the quantity $(N-n)!$ is only well defined in a system where a subset of n out of N particles can be chosen.

A.2. The n-particle density of the ideal fluid

The chemical potential of the ideal fluid is $\mu^{\mathrm{id}} = k_{\mathrm{B}}T\ln\Lambda^3\rho$. With this, the activity of the ideal fluid becomes

$$z^{\mathrm{id}} = \exp(\beta\mu^{\mathrm{id}})/\Lambda^3 = \exp(\ln\Lambda^3\rho)/\Lambda^3 = \rho.$$

Furthermore, the interatomic potential energy V_N of the ideal gas is zero, from which follows that the partition function Ξ^{id} of the ideal fluid is

$$\Xi^{\mathrm{id}} \overset{(3.1)}{=} \sum_{N=0}^{\infty} \frac{\rho^N}{N!} V^N,$$

and the n-particle density of the ideal gas is

$$\rho^{(n)} = \frac{1}{\Xi^{\mathrm{id}}} \sum_{N=n}^{\infty} \frac{\rho^N}{(N-n)!} V^{(N-n)}.$$

Now, we substitute $(N-n) \to k$, i.e. $N = k+n$, and obtain

$$\rho^{(n)} = \frac{1}{\Xi^{\mathrm{id}}} \sum_{k=0}^{\infty} \frac{\rho^n \rho^k}{k!} V^k = \frac{1}{\Xi^{\mathrm{id}}} \rho^n \Xi^{\mathrm{id}} = \rho^n.$$

B. Remarks on Chapter 6

B.1. The derivative of $\left\langle V_N'(\lambda)\right\rangle_\lambda$

$$
\begin{aligned}
\frac{\partial\left\langle V_N'(\lambda)\right\rangle_\lambda}{\partial\lambda} &\overset{(6.3)}{=} \frac{\partial}{\partial\lambda}\frac{1}{Z_N(\lambda)}\int \exp\big[-\beta V_N(\lambda)\big]V_N'(\lambda)\mathrm{d}\mathbf{r}^N \\
&= \left(\frac{\partial}{\partial\lambda}\frac{1}{Z_N(\lambda)}\right)\int \exp\big[-\beta V_N(\lambda)\big]V_N'(\lambda)\mathrm{d}\mathbf{r}^N \\
&\quad + \frac{1}{Z_N(\lambda)}\int\Big[V_N'(\lambda)\frac{\partial}{\partial\lambda}\exp\big[-\beta V_N(\lambda)\big] \\
&\qquad\qquad + \exp\big[-\beta V_N(\lambda)\big]\frac{\partial}{\partial\lambda}V_N'(\lambda)\Big]\mathrm{d}\mathbf{r}^N \\
&\overset{(2.6)}{=} -\frac{1}{Z_N(\lambda)^2}\frac{\partial}{\partial\lambda}\left(\int \exp\big[-\beta V_N(\lambda)\big]\mathrm{d}\mathbf{r}'^N\right) \\
&\quad \times \int \exp\big[-\beta V_N(\lambda)\big]V_N'(\lambda)\mathrm{d}\mathbf{r}^N \\
&\quad + \frac{1}{Z_N(\lambda)}\int\Big[-V_N'(\lambda)\exp\big[-\beta V_N(\lambda)\big]\beta V_N'(\lambda) \\
&\qquad\qquad + \exp\big[-\beta V_N(\lambda)\big]V_N''(\lambda)\Big]\mathrm{d}\mathbf{r}^N \\
&= \frac{1}{Z_N(\lambda)^2}\int \exp\big[-\beta V_N(\mathbf{r}'^N;\lambda)\big]\beta V_N'(\mathbf{r}'^N;\lambda)\mathrm{d}\mathbf{r}'^N \\
&\quad \times \int \exp\big[-\beta V_N(\lambda)\big]V_N'(\lambda)\mathrm{d}\mathbf{r}^N \\
&\quad + \frac{1}{Z_N(\lambda)}\int\Big[-\beta V_N'^2(\lambda)\exp\big[-\beta V_N(\lambda)\big] \\
&\qquad\qquad + \exp\big[-\beta V_N(\lambda)\big]V_N''(\lambda)\Big]\mathrm{d}\mathbf{r}^N \\
&= \left\langle V_N''(\lambda)\right\rangle_\lambda - \beta\Big(\left\langle [V_N'(\lambda)]^2\right\rangle_\lambda - \left\langle V_N'(\lambda)\right\rangle_\lambda^2\Big)
\end{aligned}
$$

B.2. Rewriting the expression $\langle W_N \rangle_\lambda$

First, we have

$$\begin{aligned}\langle W_N \rangle_\lambda &\overset{(2.7)}{=} \frac{1}{Z_N(\lambda)} \int W_N \exp(-\beta V_N(\lambda)) \mathrm{d}\mathbf{r}^N \\ &\overset{(6.8)}{=} \sum_{i=1}^{N} \sum_{j>i}^{N} \frac{1}{Z_N(\lambda)} \int w(r_{ij}) \exp(-\beta V_N(\lambda)) \mathrm{d}\mathbf{r}^N.\end{aligned}$$

Now, we rewrite the integral to be

$$\begin{aligned}&\int \cdots \int w(r_{ij}) \exp\big(-\beta V_N(\mathbf{r}_1, \ldots, \mathbf{r}_N; \lambda)\big) \mathrm{d}\mathbf{r}_1 \ldots \mathrm{d}\mathbf{r}_N \\ &= \int \cdots \int w(|\mathbf{d} - \mathbf{c}|) \exp\big(-\beta V_N(\mathbf{a}, \mathbf{b}, \mathbf{r}_3, \ldots, \underbrace{\mathbf{c}}_{\text{i-th}}, \ldots, \underbrace{\mathbf{d}}_{\text{j-th}}, \ldots, \mathbf{r}_N; \lambda)\big) \\ &\qquad \mathrm{d}\mathbf{a}\, \mathrm{d}\mathbf{b} \ldots \underbrace{\mathrm{d}\mathbf{c}}_{\text{i-th}} \ldots \underbrace{\mathrm{d}\mathbf{d}}_{\text{j-th}} \ldots \mathrm{d}\mathbf{r}_N \\ &= \int \cdots \int w(|\mathbf{r}_2 - \mathbf{r_1}|) \exp\big(-\beta V_N(\mathbf{r}_i, \mathbf{r}_j, \ldots, \underbrace{\mathbf{r}_1}_{\text{i-th}}, \ldots, \underbrace{\mathbf{r}_2}_{\text{j-th}}, \ldots, \mathbf{r}_N; \lambda)\big) \\ &\qquad \mathrm{d}\mathbf{r}_i\, \mathrm{d}\mathbf{r}_j \ldots \underbrace{\mathrm{d}\mathbf{r}_1}_{\text{i-th}} \ldots \underbrace{\mathrm{d}\mathbf{r}_2}_{\text{j-th}} \ldots \mathrm{d}\mathbf{r}_N \\ &= \int \cdots \int w(r_{12}) \exp\big(-\beta V_N(\mathbf{r}_1, \mathbf{r}_2, \ldots, \underbrace{\mathbf{r}_i}_{\text{i-th}}, \ldots, \underbrace{\mathbf{r}_j}_{\text{j-th}}, \ldots, \mathbf{r}_N; \lambda)\big) \\ &\qquad \mathrm{d}\mathbf{r}_1\, \mathrm{d}\mathbf{r}_2 \ldots \underbrace{\mathrm{d}\mathbf{r}_i}_{\text{i-th}} \ldots \underbrace{\mathrm{d}\mathbf{r}_j}_{\text{j-th}} \ldots \mathrm{d}\mathbf{r}_N \\ &= \int \cdots \int w(r_{12}) \exp\big(-\beta V_N(\mathbf{r}_1, \ldots, \mathbf{r}_N; \lambda)\big) \mathrm{d}\mathbf{r}_1 \ldots \mathrm{d}\mathbf{r}_N \\ &= \int w(r_{12}) \exp(-\beta V_N(\lambda)) \mathrm{d}\mathbf{r}^N\end{aligned}$$

In the first equality we rename the integration variables $\mathbf{r}_1 \to \mathbf{a}$, $\mathbf{r}_2 \to \mathbf{b}$, $\mathbf{r}_i \to \mathbf{c}$, $\mathbf{r}_j \to \mathbf{d}$, in the second equality we rename $\mathbf{c} \to \mathbf{r}_1$, $\mathbf{d} \to \mathbf{r}_2$, $\mathbf{a} \to \mathbf{r}_i$, $\mathbf{b} \to \mathbf{r}_j$, and in the third equality we exploit the fact that we assume identical particles and, hence, $V_N(\mathbf{r}_1, \ldots, \mathbf{r}_i, \ldots, \mathbf{r}_j, \ldots, \mathbf{r}_N; \lambda) =$

$V_N(\mathbf{r}_1, \ldots, \mathbf{r}_j, \ldots, \mathbf{r}_i, \ldots, \mathbf{r}_N; \lambda)$ for any i, j, i.e. $V_N(\mathbf{r}_1, \ldots, \mathbf{r}_N; \lambda)$ is invariant under the exchange of particles. Now we plug the integral back in the expression for $\langle W_N \rangle_\lambda$ and obtain

$$\langle W_N \rangle_\lambda = \sum_{i=1}^{N} \sum_{j>i}^{N} \frac{1}{Z_N(\lambda)} \int w(r_{12}) \exp(-\beta V_N(\lambda)) \mathrm{d}\mathbf{r}^N.$$

Since the integral and $Z_N(\lambda)$ are independent of i and j, we gain a factor of $N(N-1)/2$ and write

$$\begin{aligned}
\langle W_N \rangle_\lambda &= \frac{N(N-1)}{2} \frac{1}{Z_N(\lambda)} \int w(r_{12}) \exp(-\beta V_N(\lambda)) \mathrm{d}\mathbf{r}^N \\
&= \frac{1}{2} \iint \mathrm{d}\mathbf{r}_1 \mathrm{d}\mathbf{r}_2 w(r_{12}) \\
&\quad \times \underbrace{\frac{N(N-1)}{Z_N(\lambda)} \int \cdots \int \mathrm{d}\mathbf{r}_3 \ldots \mathrm{d}\mathbf{r}_N \exp(-\beta V_N(\mathbf{r}_1, \ldots, \mathbf{r}_N; \lambda))}_{\rho^{(2)}_{N;\lambda}(\mathbf{r}_1, \mathbf{r}_2)} \\
&= \frac{1}{2} \iint \rho^{(2)}_{N;\lambda}(\mathbf{r}_1, \mathbf{r}_2) w(r_{12}) \mathrm{d}\mathbf{r}_1 \mathrm{d}\mathbf{r}_2.
\end{aligned}$$

C. Remarks on Chapter 7

C.1. Functional derivative of Ω with respect to the interaction potential

We simplify the notation such that $v(\mathbf{r}_1, \mathbf{r}_2) \equiv v(1,2)$ and $\exp[-\beta v(\mathbf{r}_1, \mathbf{r}_2)] \equiv \mathrm{e}(1,2)$. Now, we rewrite the functional derivative of Ω with respect $v(1,2)$ to be a functional derivative of the partition function Ξ with respect to $\mathrm{e}(1,2)$:

$$\begin{aligned}
\frac{\delta\Omega}{\delta v(1,2)} &\overset{(3.4)}{=} \frac{\delta(-k_B T \ln \Xi)}{-k_B T(-\beta)\delta v(1,2)} \\
&= \frac{\delta \ln \Xi}{\delta \ln \mathrm{e}(1,2)} \\
&= \frac{\delta \ln \Xi}{\delta \mathrm{e}(1,2)} \frac{\partial \mathrm{e}(1,2)}{\partial \ln \mathrm{e}(1,2)} \\
&= \frac{1}{\Xi} \frac{\delta \Xi}{\delta \mathrm{e}(1,2)} \frac{\partial \exp[-\beta v(1,2)]}{-\beta \partial v(1,2)} \\
&= \frac{1}{\Xi} \frac{\delta \Xi}{\delta \mathrm{e}(1,2)} \exp[-\beta v(1,2)] \\
&= \frac{\mathrm{e}(1,2)}{\Xi} \frac{\delta \Xi}{\delta \mathrm{e}(1,2)}. \qquad \text{(C.1)}
\end{aligned}$$

Finally, the functional derivative $\delta\Xi/\delta\mathrm{e}(1,2)$ must be evaluated. For this, we consider the change in Ξ due to a variation of $e(i,j)$:

$$\delta\Xi \overset{(7.1)}{=} \sum_{N=0}^{\infty} \frac{1}{N!} \int \cdots \int \delta \left(\prod_{i,j>i}^{N} e(i,j) \right) \prod_{k=1}^{N} z^*(\mathbf{r}_k) \mathrm{d}\mathbf{r}_1 \ldots \mathrm{d}\mathbf{r}_N \qquad \text{(C.2)}$$

To evaluate the expression in parenthesis, we apply the product rule and find

$$\delta\left(\prod_{i,j>i}^{N} e(i,j)\right) = \sum_{k=1}^{N}\sum_{l>k}^{N} \delta e(k,l) \prod_{\substack{i,j>i \\ (i,j)\neq(k,l)}}^{N} e(i,j),$$

which we plug in (C.2) to obtain

$$\delta\Xi = \sum_{N=0}^{\infty} \frac{1}{N!} \sum_{k=1}^{N}\sum_{l>k}^{N} \int\cdots\int \left(\delta e(k,l) \prod_{\substack{i,j>i \\ (i,j)\neq(k,l)}}^{N} e(i,j)\right) \prod_{m=1}^{N} z^*(\mathbf{r}_m) \mathrm{d}\mathbf{r}_1 \ldots \mathrm{d}\mathbf{r}_N.$$

Now, in every summand of the double sum over k and l, we rename the integration variables such that the function $\delta e(\cdot,\cdot)$ has the variables "1" and "2" as arguments. Furthermore, we use the fact that the products and integrals are commutative which lets us write the variation of Ξ as

$$\delta\Xi = \sum_{N=0}^{\infty} \frac{1}{N!} \sum_{k=1}^{N}\sum_{l>k}^{N} \int\cdots\int \left(\delta e(1,2) \prod_{\substack{i,j>i \\ (i,j)\neq(1,2)}}^{N} e(i,j)\right) \prod_{m=1}^{N} z^*(\mathbf{r}_m) \mathrm{d}\mathbf{r}_1 \ldots \mathrm{d}\mathbf{r}_N.$$

Obviously, the summands of the double sum over k and l are now all equal which gives a factor of $N(N-1)/2$ (the number of all pairs of particles). With this we obtain

$$\delta\Xi = \sum_{N=0}^{\infty} \frac{1}{N!} \frac{N(N-1)}{2} \int\ldots\int \left(\delta e(1,2) \prod_{\substack{i,j>i \\ (i,j)\neq(1,2)}}^{N} e(i,j)\right) \prod_{m=1}^{N} z^*(\mathbf{r}_m) \mathrm{d}\mathbf{r}_1 \ldots \mathrm{d}\mathbf{r}_N.$$

Finally, we rearrange the integrals and make use of the fact that the first two terms of the sum over N vanish due to the factor $N(N-1)$ to have

$$\begin{aligned}\delta\Xi = &\iint \mathrm{d}\mathbf{r}_1 \mathrm{d}\mathbf{r}_2 \delta e(1,2) \\ &\times \left[\sum_{N=2}^{\infty} \frac{N(N-1)}{2N!} \int\cdots\int \prod_{\substack{i,j>i \\ (i,j)\neq(1,2)}}^{N} e(i,j) \prod_{m=1}^{N} z^*(\mathbf{r}_m) \mathrm{d}\mathbf{r}_3 \ldots \mathrm{d}\mathbf{r}_N\right]. \quad \text{(C.3)}\end{aligned}$$

Since per definition of the functional derivative also

$$\delta\Xi = \iint \mathrm{d}\mathbf{r}_1 \mathrm{d}\mathbf{r}_2 \delta e(1,2) \frac{\delta\Xi}{\delta \mathrm{e}(1,2)}$$

holds, we can identify the term in brackets in Eq. (C.3) as the functional derivative $\delta\Xi/\delta e(1,2)$. With this result, we now go back to Eq. (C.1) and obtain

$$\frac{\delta\Omega}{\delta v(1,2)} = \frac{1}{\Xi}\sum_{N=2}^{\infty}\frac{N(N-1)}{2N!}\int\cdots\int\prod_{i,j>i}^{N} e(i,j)\prod_{m=1}^{N} z^*(\mathbf{r}_m)\mathrm{d}\mathbf{r}_3\ldots\mathrm{d}\mathbf{r}_N.$$

This is exactly the result in Eq. (7.2).

C.2. Integration of Equation (7.3)

With the interaction potential $v_\lambda(\mathbf{r_1},\mathbf{r_2})$ [Eq. (7.4)] applied, Eq. (7.3) reads as follows:

$$\frac{\delta\mathcal{F}^{\mathrm{ex}}[\rho(\mathbf{r})]}{\delta v_\lambda(\mathbf{r}_1,\mathbf{r}_2)} = \frac{1}{2}\rho^{(2)}(\mathbf{r}_1,\mathbf{r}_2;\lambda). \tag{C.4}$$

The left-hand side of the equation, obviously, is the functional derivative of $\mathcal{F}^{\mathrm{ex}}[\rho(\mathbf{r})]$ with respect to $v_\lambda(\mathbf{r}_1,\mathbf{r}_2)$. Hence, the change $\delta\mathcal{F}^{\mathrm{ex}}$ in $\mathcal{F}^{\mathrm{ex}}[\rho(\mathbf{r})]$ due to the variation of v_λ is

$$\delta_\lambda\mathcal{F}^{\mathrm{ex}}[\rho(\mathbf{r})] = \iint\frac{\delta\mathcal{F}^{\mathrm{ex}}[\rho(\mathbf{r})]}{\delta v_\lambda(\mathbf{r}_1,\mathbf{r}_2)}\delta v_\lambda(\mathbf{r}_1,\mathbf{r}_2)\mathrm{d}\mathbf{r}_1\mathrm{d}\mathbf{r}_2, \tag{C.5}$$

which essentially is a multiplication of the left hand side of Eq. (C.4) with the variation $\delta v_\lambda(\mathbf{r}_1,\mathbf{r}_2)$ followed by an integration. Note that $v_\lambda(\mathbf{r}_1,\mathbf{r}_2)$ varies since λ varies, indicated by the subscript λ in δ_λ. If we apply this operation on either side of (C.4), we obtain

$$\iint\frac{\delta\mathcal{F}^{\mathrm{ex}}[\rho(\mathbf{r})]}{\delta v_\lambda(\mathbf{r}_1,\mathbf{r}_2)}\delta v_\lambda(\mathbf{r}_1,\mathbf{r}_2)\mathrm{d}\mathbf{r}_1\mathrm{d}\mathbf{r}_2 = \frac{1}{2}\iint\rho^{(2)}(\mathbf{r}_1,\mathbf{r}_2;\lambda)\delta v_\lambda(\mathbf{r}_1,\mathbf{r}_2)\mathrm{d}\mathbf{r}_1\mathrm{d}\mathbf{r}_2. \tag{C.6}$$

Since $v_\lambda(\mathbf{r}_1,\mathbf{r}_2)$ is not a functional but a function, it holds that

$$\delta v_\lambda(\mathbf{r}_1,\mathbf{r}_2) = \mathrm{d}v_\lambda(\mathbf{r}_1,\mathbf{r}_2) = \frac{\partial v_\lambda(\mathbf{r}_1,\mathbf{r}_2)}{\partial\lambda}\mathrm{d}\lambda = w(\mathbf{r}_1,\mathbf{r}_2)\mathrm{d}\lambda. \tag{C.7}$$

Now, we plug in Eq. (C.7) on the right-hand side and Eq. (C.5) on the left-hand side of (C.6) which yields

$$\delta_\lambda\mathcal{F}^{\mathrm{ex}}[\rho(\mathbf{r})] = \frac{1}{2}\iint\rho^{(2)}(\mathbf{r}_1,\mathbf{r}_2;\lambda)w(\mathbf{r}_1,\mathbf{r}_2)\mathrm{d}\mathbf{r}_1\mathrm{d}\mathbf{r}_2\,\mathrm{d}\lambda. \tag{C.8}$$

Since λ is a scalar, we integrate on either side of the Eq. (C.8) to get

$$\int_{\mathcal{F}^{\mathrm{ex}}_{(\lambda=0)}}^{\mathcal{F}^{\mathrm{ex}}_{(\lambda=1)}} \delta_\lambda \mathcal{F}^{\mathrm{ex}} = \frac{1}{2}\int_0^1 \mathrm{d}\lambda \iint \rho^{(2)}(\mathbf{r}_1,\mathbf{r}_2;\lambda) w(\mathbf{r}_1,\mathbf{r}_2)\mathrm{d}\mathbf{r}_1\mathrm{d}\mathbf{r}_2.$$

With $\delta_\lambda \mathcal{F}^{\mathrm{ex}} = \mathcal{F}^{\mathrm{ex}}|_{v_\lambda+\delta_\lambda} - \mathcal{F}^{\mathrm{ex}}|_{v_\lambda}$, we can evaluate the left-hand side and find

$$\mathcal{F}^{\mathrm{ex}}_{(\lambda=1)}[\rho(\mathbf{r})] - \mathcal{F}^{\mathrm{ex}}_{(\lambda=0)}[\rho(\mathbf{r})] = \frac{1}{2}\int_0^1 \mathrm{d}\lambda \iint \rho^{(2)}(\mathbf{r}_1,\mathbf{r}_2;\lambda) w(\mathbf{r}_1,\mathbf{r}_2)\mathrm{d}\mathbf{r}_1\mathrm{d}\mathbf{r}_2.$$

Now, we rename $\mathcal{F}^{\mathrm{ex}}_{(\lambda=1)}[\rho(\mathbf{r})]$ to be $\mathcal{F}^{\mathrm{ex}}[\rho(\mathbf{r})]$ and $\mathcal{F}^{\mathrm{ex}}_{(\lambda=0)}[\rho(\mathbf{r})]$ to be $\mathcal{F}^{\mathrm{ex}}_0[\rho(\mathbf{r})]$, the latter being the intrinsic free energy functional of the reference system, and use that $\rho^{(2)}(\mathbf{r}_1,\mathbf{r}_2;\lambda) \overset{(3.7)}{=} \rho(\mathbf{r}_1)\rho(\mathbf{r}_2)g^{(2)}(\mathbf{r}_1,\mathbf{r}_2;\lambda)$, to obtain

$$\begin{aligned}\mathcal{F}^{\mathrm{ex}}[\rho(\mathbf{r})] &= \mathcal{F}^{\mathrm{ex}}_0[\rho(\mathbf{r})] + \frac{1}{2}\int_0^1 \mathrm{d}\lambda \iint \rho(\mathbf{r}_1)\rho(\mathbf{r}_2) g^{(2)}(\mathbf{r}_1,\mathbf{r}_2;\lambda) w(\mathbf{r}_1,\mathbf{r}_2)\mathrm{d}\mathbf{r}_1\mathrm{d}\mathbf{r}_2 \\ &\equiv \mathcal{F}^{\mathrm{ex}}_0[\rho(\mathbf{r})] + \mathcal{F}^{\mathrm{ex}}_w[\rho(\mathbf{r})].\end{aligned}$$

Note that Eq. (3.7) also holds in the inhomogeneous case, and, hence, since $\rho^{(2)}(\mathbf{r}_1,\mathbf{r}_2;\lambda)$ is the 2-particle density of the inhomogeneous system (see Fn. 3 in Sec. 7.1.1), $g^{(2)}(\mathbf{r}_1,\mathbf{r}_2;\lambda)$ is the 2-particle distribution function of the inhomogeneous system.

D. Remarks on Chapter 9

D.1. Rewriting the system pressure

We start by plugging into Eq. (9.11) the expressions for the ideal gas contributions to the free energy density [see first line of Eq. (6.25)] and the expressions for the chemical potentials in Eqs. (9.7) and (9.9):

$$\begin{aligned}\beta p = &-\rho_\mathrm{c}\big[\ln(\Lambda^3\rho_\mathrm{c})-1\big]-\rho_1\big[\ln(\Lambda^3\rho_1)-1\big]-\rho_2\big[\ln(\Lambda^3\rho_2)-1\big]\\ &-\Phi+\rho_1\ln\big(\psi_1(\eta_\mathrm{c})\big)+\rho_2\ln\big(\psi_2(\eta_\mathrm{c})\big)\\ &+\rho_\mathrm{c}\ln\big(\Lambda^3\rho_\mathrm{c}\big)+\rho_\mathrm{c}\frac{\partial\Phi}{\partial\rho_\mathrm{c}}-\rho_\mathrm{c}\rho_1\frac{\partial\ln\big(\psi_1(\eta_\mathrm{c})\big)}{\partial\rho_\mathrm{c}}-\rho_\mathrm{c}\rho_2\frac{\partial\ln\big(\psi_2(\eta_\mathrm{c})\big)}{\partial\rho_\mathrm{c}}\\ &+\rho_1\ln(\Lambda^3\rho_1)-\rho_1\ln\big(\psi_1(\eta_\mathrm{c})\big)+\rho_2\ln(\Lambda^3\rho_2)-\rho_2\ln\big(\psi_2(\eta_\mathrm{c})\big).\end{aligned}$$

This rather lengthy expression can be simplified to be

$$\beta p=\rho_\mathrm{c}-\Phi+\rho_\mathrm{c}\frac{\partial\Phi}{\partial\rho_\mathrm{c}}+\rho_1+\rho_2-\rho_\mathrm{c}\rho_1\frac{\partial\ln\big(\psi_1(\eta_\mathrm{c})\big)}{\partial\rho_\mathrm{c}}-\rho_\mathrm{c}\rho_2\frac{\partial\ln\big(\psi_2(\eta_\mathrm{c})\big)}{\partial\rho_\mathrm{c}},$$

where we identify the first three terms as the pressure of the unperturbed colloid system, $\beta p_\mathrm{c}^\circ=\rho_\mathrm{c}-\Phi+\rho_\mathrm{c}{}^{\partial\Phi}/_{\partial\rho_\mathrm{c}}$. Now, we replace the polymer system densities ρ_i by the polymer reservoir densities ρ_i^r via Eq. (9.8), and subsequently use that ${}^{\partial\ln(\psi_i)}/_{\partial\rho_\mathrm{c}}={}^{1}/_{\psi_i}\,{}^{\partial\psi_i}/_{\partial\rho_\mathrm{c}}$ to obtain

$$\beta p=\beta p_\mathrm{c}^\circ+\rho_1^\mathrm{r}\left[\psi_1-\rho_\mathrm{c}\frac{\partial\psi_1}{\partial\rho_\mathrm{c}}\right]+\rho_1^\mathrm{r}\left[\psi_1-\rho_\mathrm{c}\frac{\partial\psi_1}{\partial\rho_\mathrm{c}}\right].$$

Finally, we rewrite the derivatives with respect to ρ_c as derivatives with respect to η_c, ${}^{\partial\psi_i}/_{\partial\rho_\mathrm{c}}={}^{\partial\psi_i}/_{\partial\eta_\mathrm{c}}\,{}^{\partial\eta_\mathrm{c}}/_{\partial\rho_\mathrm{c}}={}^{\partial\psi_i}/_{\partial\eta_\mathrm{c}}\,{}^{\pi}/_{6}\,\sigma_\mathrm{c}^3$, and replace ρ_c via $\eta_\mathrm{c}={}^{\pi}/_{6}\,\rho_\mathrm{c}\sigma_\mathrm{c}^3$. With this, we find the result in Eq. (9.12):

$$\beta p=\beta p_\mathrm{c}^\circ+\rho_1^\mathrm{r}\left[\psi_1-\eta_\mathrm{c}\frac{\partial\psi_1}{\partial\eta_\mathrm{c}}\right]+\rho_2^\mathrm{r}\left[\psi_2-\eta_\mathrm{c}\frac{\partial\psi_2}{\partial\eta_\mathrm{c}}\right].$$

Bibliography

[1] Archer, Andrew J. ; Chacko, Blesson ; Evans, Robert: The standard mean-field treatment of inter-particle attraction in classical DFT is better than one might expect. In: *The Journal of Chemical Physics* 147 (2017), jul, Nr. 3, S. 034501. http://dx.doi.org/10.1063/1.4993175. – DOI 10.1063/1.4993175

[2] Asakura, Sho ; Oosawa, Fumio: On Interaction between Two Bodies Immersed in a Solution of Macromolecules. In: *The Journal of Chemical Physics* 22 (1954), jul, Nr. 7, S. 1255–1256. http://dx.doi.org/10.1063/1.1740347. – DOI 10.1063/1.1740347

[3] Asakura, Sho ; Oosawa, Fumio: Interaction between particles suspended in solutions of macromolecules. In: *Journal of Polymer Science* 33 (1958), dec, Nr. 126, S. 183–192. http://dx.doi.org/10.1002/pol.1958.1203312618. – DOI 10.1002/pol.1958.1203312618

[4] Barker, J. A. ; Henderson, D.: Perturbation Theory and Equation of State for Fluids. II. A Successful Theory of Liquids. In: *The Journal of Chemical Physics* 47 (1967), dec, Nr. 11, S. 4714–4721. http://dx.doi.org/10.1063/1.1701689. – DOI 10.1063/1.1701689

[5] Barker, J. A. ; Henderson, D.: Perturbation Theory and Equation of State for Fluids: The Square-Well Potential. In: *The Journal of Chemical Physics* 47 (1967), oct, Nr. 8, S. 2856–2861. http://dx.doi.org/10.1063/1.1712308. – DOI 10.1063/1.1712308

[6] Bellissent-Funel, M.-C: Is there a liquid-liquid phase transition in supercooled water? In: *Europhysics Letters (EPL)* 42 (1998), apr, Nr. 2, S. 161–166. http://dx.doi.org/10.1209/epl/i1998-00223-5. – DOI 10.1209/epl/i1998–00223–5

[7] Carnahan, Norman F. ; Starling, Kenneth E.: Equation of State for Nonattracting Rigid Spheres. In: *The Journal of Chemical Physics* 51 (1969), jul, Nr. 2, S. 635–636. http://dx.doi.org/10.1063/1.1672048. – DOI 10.1063/1.1672048

[8] Daan Frenkel, Berend S.: *Understanding Molecular Simulation*. Elsevier LTD, Oxford, 2001 https://www.ebook.de/de/product/4256976/daan_frenkel_berend_smit_understanding_molecular_simulation.html. – ISBN 0122673514

[9] Debenedetti, Pablo G.: Supercooled and glassy water. In: *Journal of Physics: Condensed Matter* 15 (2003), oct, Nr. 45, S. R1669–R1726. http://dx.doi.org/10.1088/0953-8984/15/45/r01. – DOI 10.1088/0953–8984/15/45/r01

[10] Dijkstra, Marjolein ; Brader, Joseph M. ; Evans, Robert: Phase behaviour and structure of model colloid-polymer mixtures. In: *Journal of Physics: Condensed Matter* 11 (1999), dec, Nr. 50, S. 10079–10106. http://dx.doi.org/10.1088/0953-8984/11/50/304. – DOI 10.1088/0953–8984/11/50/304

[11] Evans, R.: The nature of the liquid-vapour interface and other topics in the statistical mechanics of non-uniform, classical fluids. In: *Advances in Physics* 28 (1979), apr, Nr. 2, S. 143–200. http://dx.doi.org/10.1080/00018737900101365. – DOI 10.1080/00018737900101365

[12] Evans, R: Fluids adsorbed in narrow pores: phase equilibria and structure. In: *Journal of Physics: Condensed Matter* 2 (1990), nov, Nr. 46, S. 8989–9007. http://dx.doi.org/10.1088/0953-8984/2/46/001. – DOI 10.1088/0953–8984/2/46/001

[13] Franzese, G. ; Malescio, G. ; Skibinsky, A. ; Buldyrev, S. V. ; Stanley, H. E.: Metastable liquid-liquid phase transition in a single-component system with only one crystal phase and no density anomaly. In: *Physical Review E* 66 (2002), nov, Nr. 5. http://dx.doi.org/10.1103/physreve.66.051206. – DOI 10.1103/physreve.66.051206

[14] Franzese, Giancarlo ; Malescio, Gianpietro ; Skibinsky, Anna ; Buldyrev, Sergey V. ; Stanley, H. E.: Generic mechanism for generating a liquid–liquid phase transition. In: *Nature* 409 (2001), feb, Nr. 6821, S. 692–695. http://dx.doi.org/10.1038/35055514. – DOI 10.1038/35055514

[15] Grodon, C. ; Roth, R.: Multiphase coexistence in polydisperse colloidal mixtures. In: *The Journal of Chemical Physics* 126 (2007), feb, Nr. 5, S. 054901. http://dx.doi.org/10.1063/1.2430524. – DOI 10.1063/1.2430524

[16] Gussmann, Florian B.: *Statistical physics of ion channels*, Universität Tübingen, Diploma thesis, 2014

[17] Hansen, Jean-Pierre ; McDonald, Ian R.: *Theory of Simple Liquids; with Applications to Soft Matter*. Elsevier LTD, Oxford, 2013 https://www.ebook.de/de/product/20578656/jean_pierre_hansen_ian_r_mcdonald_theory_of_simple_liquids_with_applications_to_soft_matter.html. – ISBN 0123870321

[18] Hansen-Goos, Hendrik ; Roth, Roland: Density functional theory for hard-sphere mixtures: the White Bear version mark II. In: *Journal of Physics: Condensed Matter* 18 (2006), aug, Nr. 37, S. 8413–8425. http://dx.doi.org/10.1088/0953-8984/18/37/002. – DOI 10.1088/0953–8984/18/37/002

[19] Haro, Mariano L. ; Rodríguez-Rivas, Álvaro ; Yuste, Santos B. ; Santos, Andrés: Structural properties of the Jagla fluid. In: *Physical Review E* 98 (2018), jul, Nr. 1. http://dx.doi.org/10.1103/physreve.98.012138. – DOI 10.1103/physreve.98.012138

[20] Henderson, Douglas (Hrsg.): *Fundamentals of Inhomogeneous Fluids*. Taylor & Francis Inc, 1992 https://www.ebook.de/de/product/4332749/fundamentals_of_inhomogeneous_fluids.html. – ISBN 0824787110

[21] Henderson, R.L.: A uniqueness theorem for fluid pair correlation functions. In: *Physics Letters A* 49 (1974), sep, Nr. 3, S. 197–198. http://dx.doi.org/10.1016/0375-9601(74)90847-0. – DOI 10.1016/0375–9601(74)90847–0

[22] Jagla, E. A.: Liquid-liquid equilibrium for monodisperse spherical particles. In: *Physical Review E* 63 (2001), may, Nr. 6. http://dx.doi.org/10.1103/physreve.63.061501. – DOI 10.1103/physreve.63.061501

[23] Llano-Restrepo, Mario ; Chapman, Walter G.: Bridge function and cavity correlation function for the Lennard-Jones fluid from simulation. In: *The Journal of Chemical Physics* 97 (1992), aug, Nr. 3, S. 2046–2054. http://dx.doi.org/10.1063/1.463142. – DOI 10.1063/1.463142

[24] Lomba, E. ; Almarza, N. G. ; Martín, C. ; McBride, C.: Phase behavior of attractive and repulsive ramp fluids: Integral equation and computer simulation studies. In: *The Journal of Chemical Physics* 126 (2007), jun, Nr. 24, S. 244510. http://dx.doi.org/10.1063/1.2748043. – DOI 10.1063/1.2748043

[25] Metropolis, Nicholas ; Rosenbluth, Arianna W. ; Rosenbluth, Marshall N. ; Teller, Augusta H. ; Teller, Edward: Equation of

State Calculations by Fast Computing Machines. In: *The Journal of Chemical Physics* 21 (1953), jun, Nr. 6, S. 1087–1092. http://dx.doi.org/10.1063/1.1699114. – DOI 10.1063/1.1699114

[26] Nolting, Wolfgang: *Grundkurs Theoretische Physik 6*. Springer-Verlag GmbH, 2013 https://www.ebook.de/de/product/18307225/wolfgang_nolting_grundkurs_theoretische_physik_6.html. – ISBN 364225392X

[27] Norman, G. E. ; Filinov, V. S.: Investigation of phase transitions by a Monte Carlo method. In: *High Temp. (USSR)* 7 (1969), S. 216–222

[28] Oversteegen, S. M. ; Roth, R.: General methods for free-volume theory. In: *The Journal of Chemical Physics* 122 (2005), jun, Nr. 21, S. 214502. http://dx.doi.org/10.1063/1.1908765. – DOI 10.1063/1.1908765

[29] Poole, Peter H. ; Sciortino, Francesco ; Essmann, Ulrich ; Stanley, H. E.: Phase behaviour of metastable water. In: *Nature* 360 (1992), nov, Nr. 6402, S. 324–328. http://dx.doi.org/10.1038/360324a0. – DOI 10.1038/360324a0

[30] Rosenfeld, Yaakov: Free-energy model for the inhomogeneous hard-sphere fluid mixture and density-functional theory of freezing. In: *Physical Review Letters* 63 (1989), aug, Nr. 9, S. 980–983. http://dx.doi.org/10.1103/physrevlett.63.980. – DOI 10.1103/physrevlett.63.980

[31] Roth, R ; Evans, R ; Lang, A ; Kahl, G: Fundamental measure theory for hard-sphere mixtures revisited: the White Bear version. In: *Journal of Physics: Condensed Matter* 14 (2002), nov, Nr. 46, S. 12063–12078. http://dx.doi.org/10.1088/0953-8984/14/46/313. – DOI 10.1088/0953–8984/14/46/313

[32] Roth, Roland: Fundamental measure theory for hard-sphere mixtures: a review. In: *Journal of Physics: Condensed Matter* 22 (2010), jan, Nr. 6, S. 063102. http://dx.doi.org/10.1088/0953-8984/22/6/063102. – DOI 10.1088/0953–8984/22/6/063102

[33] Roth, Roland ; Hansen-Goos, Hendrik: Classical density functional theory meets Monte-Carlo simulations. In: *Molecular Physics* (2018), apr, S. 1–8. http://dx.doi.org/10.1080/00268976.2018.1456686. – DOI 10.1080/00268976.2018.1456686

[34] Santos, Andrés ; Yuste, Santos B. ; Haro, Mariano L. ; Bárcenas, Mariana ; Orea, Pedro: Structural properties of fluids interacting via

piece-wise constant potentials with a hard core. In: *The Journal of Chemical Physics* 139 (2013), aug, Nr. 7, S. 074505. http://dx.doi.org/10.1063/1.4818601. – DOI 10.1063/1.4818601

[35] Schmidt, Matthias ; Fortini, Andrea ; Dijkstra, Marjolein: Capillary condensation of colloid–polymer mixtures confined between parallel plates. In: *Journal of Physics: Condensed Matter* 15 (2003), nov, Nr. 48, S. S3411–S3420. http://dx.doi.org/10.1088/0953-8984/15/48/002. – DOI 10.1088/0953–8984/15/48/002

[36] Schmidt, Matthias ; Löwen, Hartmut ; Brader, Joseph M. ; Evans, Robert: Density Functional for a Model Colloid-Polymer Mixture. In: *Physical Review Letters* 85 (2000), aug, Nr. 9, S. 1934–1937. http://dx.doi.org/10.1103/physrevlett.85.1934. – DOI 10.1103/physrevlett.85.1934

[37] Sokolowski, S. ; Fischer, J.: The role of attractive intermolecular forces in the density functional theory of inhomogeneous fluids. In: *The Journal of Chemical Physics* 96 (1992), apr, Nr. 7, S. 5441–5447. http://dx.doi.org/10.1063/1.462727. – DOI 10.1063/1.462727

[38] Tschopp, S. M. ; Vuijk, H. D. ; Sharma, A. ; Brader, J. M.: Mean-field theory of inhomogeneous fluids. In: *Physical Review E* 102 (2020), oct, Nr. 4. http://dx.doi.org/10.1103/physreve.102.042140. – DOI 10.1103/physreve.102.042140

[39] Vrij, A.: Polymers at Interfaces and the Interactions in Colloidal Dispersions. In: *Pure and Applied Chemistry* 48 (1976), jan, Nr. 4, S. 471–483. http://dx.doi.org/10.1351/pac197648040471. – DOI 10.1351/pac197648040471

[40] Wadewitz, T. ; Winkelmann, J.: Application of density functional perturbation theory to pure fluid liquid–vapor interfaces. In: *The Journal of Chemical Physics* 113 (2000), aug, Nr. 6, S. 2447–2455. http://dx.doi.org/10.1063/1.482062. – DOI 10.1063/1.482062

[41] Weeks, John D. ; Chandler, David ; Andersen, Hans C.: Role of Repulsive Forces in Determining the Equilibrium Structure of Simple Liquids. In: *The Journal of Chemical Physics* 54 (1971), jun, Nr. 12, S. 5237–5247. http://dx.doi.org/10.1063/1.1674820. – DOI 10.1063/1.1674820

[42] Xu, L. ; Kumar, P. ; Buldyrev, S. V. ; Chen, S.-H. ; Poole, P. H. ; Sciortino, F. ; Stanley, H. E.: Relation between the Widom line and

the dynamic crossover in systems with a liquid-liquid phase transition. In: *Proceedings of the National Academy of Sciences* 102 (2005), nov, Nr. 46, S. 16558–16562. http://dx.doi.org/10.1073/pnas.0507870102. – DOI 10.1073/pnas.0507870102